

# Mission Performance Assessment of a Box-Wing Aircraft

A Multiphase Optimal Control Approach Including  
Exploration of Unconventional Control

S.P. de Wringer

Technische Universiteit Delft





# Mission Performance Assessment of a Box-Wing Aircraft

**A Multiphase Optimal Control Approach  
Including Exploration of Unconventional  
Control**

by

S.P. de Wringer

to obtain the degree of Master of Science  
at the Delft University of Technology,  
to be defended publicly on Wednesday, June 12, 2020 at 13:30.

Student number: 4351568  
Project duration: September 26, 2019 – June 12, 2020  
Thesis committee: Prof. dr. ir. L.L.M. Veldhuis, TU Delft, committee chair  
Dr. F. Oliviero, TU Delft, supervisor  
C. Varriale MSc, TU Delft, supervisor  
Ir. P.C. Roling, TU Delft

An electronic version of this thesis is available at <http://repository.tudelft.nl/>.



# Preface

This report about the mission profile optimisation and corresponding mission performance assessment of a box-wing aircraft has been written in partial fulfilment and as the conclusion of the MSc curriculum in Aerospace Engineering at the Delft University of Technology (TUD). Even though the emphasis of this report is put on the box-wing aircraft's commercial mission performance, the tool that has been developed can be put to use in a larger context. I therefore hope that my work will prove useful for future research at the Aerospace Engineering faculty, whether it be about commercial aircraft mission analysis or some other problem requiring trajectory optimisation to gain insights.

I would like to thank Carmine Varriale and Fabrizio Oliviero for supervising me in this thesis project. I appreciate that you have always shown a relaxed and open-minded attitude towards suggestions from my side and that you have explicitly expressed your confidence in my bringing this research to a higher level. Carmine, as my former neighbour and daily supervisor, I want to thank you especially for taking such a door-is-always-open, approachable stance.

Moreover, I would like to thank my family. Thanks, mam and pap, not only for giving me the opportunity to study, but especially for expressing your confidence in my abilities, being supportive, and lending a sympathetic ear, always. Thanks, zusters, for our being so close and being there for one another, through thin and thick.

Finally, I would like to express my gratitude towards Simon Tandje, without whom I would have never got to know de Heren van Stand I am now very happy to call my life-long mates.

*S.P. de Wringer  
Delft, June 2020*



# Executive Summary

It is the aim of this research to assess the mission performance of a box-wing aircraft by developing a configuration-agnostic, multi-fidelity optimal control toolbox for performance and mission analysis. The box-wing aircraft, sometimes named a PrandtlPlane (PrP), is an unconventional aircraft. An instance with redundant controls is designed within the PARSIFAL project. This specific aircraft is designed for commercial transport in the short-range segment (a 4000 km design range) and for a high passenger capacity (up to 308 passengers). Because of the beneficial induced drag characteristics inherent to the box-wing configuration, the PrP represents a possible solution towards the sustainable future of aviation.

To investigate the potential of the PrP as an alternative to conventional commercial aircraft, the mission performance assessment of the aircraft has been split into two components. The first part of the assessment covers the comparison between the performance of the PARSIFAL-designed PrP and that of a competitor aircraft with a similar design range, the A320, while allowing only non-redundant controls. The second part of the assessment involves the quantification of the PrP's performance when allowing redundant controls in the form of Direct Lift Control (DLC), enabling the aircraft to increase its net lift without a change in pitching moment.

Analyses of the PrP and its competitor aircraft for various ranges have shown that the PrP outperforms its competitor in terms of relative fuel consumption. When flying its minimum-fuel mission, the PrP's competitor consumes less fuel in absolute terms. Nonetheless, because the PrP carries more than twice as many passengers, it consumes up to 14.5 % less fuel per passenger per kilometre.

In other respects the PrP's performance is inferior to that of its competitor. The 5400 km maximum range of the PrP is considerably lower than its competitor's maximum range of 6200 km. Moreover, at a fuel-optimal Mach number of approximately 0.7 the PrP cruises appreciably slower than the cruise Mach number for which it was designed, unlike its competitor. In general, the PrP flies its trajectories much slower than its competitor at an approximately 10 % lower average velocity in the minimum-fuel missions.

If both time and fuel are considered equally in the cruise altitude optimisation, the design altitude of 11 km is deemed appropriate. If only fuel consumption is considered, the PrP would benefit in fuel economy from lowering the initial cruise altitude at the cost of increased mission time. At an optimal altitude of 9.3 km, the PrP would consume 2.2 % less fuel than at its design altitude of 11 km at the cost of even slower flight.

The sensitivities of the PrP's mission time and fuel performance to changes in its design Zero-fuel Mass (ZFM) have been investigated. Keeping the Maximum Takeoff Mass (MTOM) constant while varying the ZFM, design mission simulations were run for the PrP for several objective functions. It was found that when flying for minimum fuel, a 1 % increase in ZFM incurs a fuel consumption penalty of over 1 % through a near-linear, direct proportionality. Likewise, the mission time varies nearly linearly with the ZFM; a 1 % increase results in an approximate mission time increase of nearly 0.5 %.

The incremental aerodynamic lift and drag due to control surface deflections for DLC were modelled using a flat-plate approximation. With this approach, the projected mission-level benefits of using DLC are marginal. On the design mission, the results indicate an increase in fuel economy of 0.6 % on the minimum-fuel mission and negligible temporal gains on the minimum-time mission. It is however emphasised that numerical uncertainties due to the discretisation of the problem pollute all obtained solutions to some degree, such that appropriate caution should be exercised when interpreting these results in an absolute sense.

In future research, a grid refinement study would be a valuable addition to quantify and bound these uncertainties. It is deemed equally important to look into a more sophisticated way to model the control surface aerodynamics necessary for assessing the benefits of DLC.

A broader recommendation pertains to future research on box-wing aircraft aerodynamic design. The current research has indicated that the optimal trajectories for the PrP result in very distinct flight profiles when optimising for different objectives. Therefore, it would be interesting to see how the aerodynamic design could evolve, such that flying for fuel economy wouldn't require such a compromise in temporal performance and vice versa.



# Contents

<b>Preface</b>	<b>iii</b>
<b>Executive Summary</b>	<b>v</b>
<b>List of Figures</b>	<b>ix</b>
<b>List of Tables</b>	<b>xi</b>
<b>List of Acronyms</b>	<b>xiii</b>
<b>List of Symbols</b>	<b>xv</b>
<b>1 Introduction</b>	<b>1</b>
<b>2 PARSIFAL Project</b>	<b>5</b>
2.1 Prandtl's Best Wing System . . . . .	5
2.2 Design Drivers and Requirements . . . . .	6
2.3 Aircraft Component Sizing and Performance Analyses. . . . .	8
2.3.1 Control Surface Sizing and Applications . . . . .	8
2.3.2 Mission Performance Analysis . . . . .	10
2.4 Place of the Thesis within PARSIFAL . . . . .	11
<b>3 Flight Mechanics Model</b>	<b>13</b>
3.1 Equations of Motion . . . . .	13
3.1.1 Simplifying Assumptions . . . . .	13
3.1.2 Equations of Motion Formulation and Computational Complexity . . . . .	14
3.2 Aerodynamic Model . . . . .	15
3.2.1 Force Decomposition. . . . .	15
3.2.2 High-Lift Devices Aerodynamic Modelling. . . . .	16
3.2.3 Control Surface Aerodynamic Modelling . . . . .	17
3.3 Propulsive Model . . . . .	18
<b>4 Optimal Control Theory</b>	<b>21</b>
4.1 Fundamentals of Optimal Control . . . . .	21
4.1.1 Multiphase Problem Formulation . . . . .	21
4.1.2 State and Control Vector Definitions. . . . .	22
4.1.3 Excessive Control Penalisation . . . . .	23
4.2 Transcription Methods . . . . .	23
4.2.1 Indirect and Direct Solution Approaches . . . . .	23
4.2.2 Shooting and Collocation Methods . . . . .	24
4.3 Choice of Software . . . . .	25
<b>5 Mission Model and Program Architecture</b>	<b>27</b>
5.1 Aircraft Mission Modelling . . . . .	27
5.1.1 Aircraft Missions, Constraints, and Capture Conditions . . . . .	27
5.1.2 Mission Class System . . . . .	28
5.1.3 Flight Phase Stereotypes . . . . .	29
5.1.4 PrandtlPlane Design Mission . . . . .	32
5.2 Program Flow. . . . .	33
<b>6 Verification and Validation</b>	<b>35</b>
6.1 Problem Setup . . . . .	35
6.1.1 Reference Study Setup . . . . .	35
6.1.2 Current Study Setup . . . . .	36

---

6.2	Comparison of Trajectories . . . . .	37
<b>7</b>	<b>Mission Performance</b>	<b>41</b>
7.1	Design Mission Performance . . . . .	41
7.1.1	Design Mission Trajectory Comparison . . . . .	41
7.1.2	Top-Level Design Requirement Sensitivity . . . . .	44
7.2	Harmonic Mission Performance . . . . .	46
7.3	Top-level Mission Performance for Various Ranges . . . . .	46
<b>8</b>	<b>Unconventional Control Benefits</b>	<b>49</b>
<b>9</b>	<b>Conclusions and Recommendations</b>	<b>53</b>
	<b>Bibliography</b>	<b>57</b>

# List of Figures

1.1	The historical development of the PRE. Image taken from Ref. [11]. . . . .	2
2.1	The BWS as drawn out by Prandtl. Image taken from Ref. [20]. . . . .	6
2.2	The wing loading optimality condition for minimum induced drag on a symmetric biplane. Image taken from Ref. [23]. . . . .	6
2.3	The forecast air passenger demand up to the year 2032. Image taken from Ref. [25] . . . . .	7
2.4	Passenger-range diagram showing the position of the PrP with respect to other aircraft. Image taken from Ref. [28]. . . . .	7
2.5	Aviation mega-cities' airport congestion. Image adapted from Airbus. . . . .	8
2.6	The baseline configuration of the PrP. Image taken from Ref. [31]. . . . .	9
2.7	The RP plotted as a function of TAS, altitude, and aircraft mass. Image taken from Ref. [35]. . .	10
2.8	A non-diverted simulated mission profile for a range of 4,000 km. Image taken from Ref. [35]. .	11
2.9	Fuel burn per passenger and mission duration for several ranges. Image adapted from Ref. [35].	11
3.1	The topocentric ( $Exyh$ ) and Earth-centred ( $OXYZ$ ) reference frames, adapted from Ref. [40]. .	14
3.2	The body ( $X_bY_bZ_b$ ) and (partial) airpath ( $X_a \parallel V$ ) reference frames, adapted from Ref. [42]. . .	14
3.3	The lift-drag polar of the PrP as a function of Mach number for coordinated flight. . . . .	16
3.4	The lift-drag polar of the CSR-01 as a function of Mach number for coordinated flight. . . . .	16
3.5	The incremental lift and drag as a function of $M\delta$ , with $\delta$ in degrees. Image adapted from Ref. [49].	17
3.6	The span efficiencies of several unconventional aircraft configurations. Image adapted from Ref. [50]. . . . .	18
3.7	The maximum available thrust of the PrP as a function of altitude and Mach number. . . . .	19
3.8	The maximum available thrust of the CSR-01 as a function of altitude and Mach number. . . . .	19
3.9	The TSFC of the PrP as a function of altitude and Mach number at maximum thrust. . . . .	19
3.10	The TSFC of the CSR-01 as a function of altitude and Mach number at maximum thrust. . . . .	19
4.1	An impression of phase linkage. Image taken from Ref. [55]. . . . .	22
4.2	The taxonomy of optimal control transcription methods, indicating drawbacks and benefits of each. Image taken from Ref. [57]. . . . .	25
5.1	A typical commercial aircraft mission profile including hold, without diversion. Image taken from Ref. [63]. . . . .	28
5.2	A UML class diagram of the mission and flightPhase objects. . . . .	29
5.3	Descriptive terms of the holding pattern. Image taken from AIP ENR 1.5. . . . .	31
5.4	A UML activity diagram of the trajectory optimisation program. . . . .	33
6.1	The Madrid-Barajas airport SID PINAR1U. Map generated with the Spanish ENAIRE AIP tool.	36
6.2	The reference, replicate, and adapted trajectories' ground tracks, mapped using a Mercator projection. . . . .	37
6.3	The phase switching or end times for each of the mission setups. . . . .	37
6.4	The reference, replicate, and adapted trajectories' heading angle time histories. . . . .	37
6.5	The reference, replicate, and adapted trajectories' aircraft mass time histories. . . . .	38
6.6	The reference, replicate, and adapted trajectories' fuel consumption time histories. . . . .	38
6.7	The reference, replicate, and adapted trajectories' altitude time histories. . . . .	38
6.8	The reference, replicate, and adapted trajectories' lift coefficient time histories. . . . .	38
6.9	The reference, replicate, and adapted trajectories' velocity time histories. . . . .	39
6.10	The reference, replicate, and adapted trajectories' thrust time histories. . . . .	39
6.11	The reference, replicate, and adapted trajectories' flight path angle time histories. . . . .	39
6.12	The reference, replicate, and adapted trajectories' aerodynamic roll angle time histories. . . . .	39

7.1	The PrP's design mission 2D trajectory for several CIs. . . . .	41
7.2	The CSR-01's design mission 2D trajectory for several CIs. . . . .	41
7.3	The PrP's design mission fuel consumption for several CIs. . . . .	42
7.4	The CSR-01's design mission fuel consumption for several CIs. . . . .	42
7.5	The PrP's design mission mass for several CIs. . . . .	42
7.6	The CSR-01's design mission mass for several CIs. . . . .	42
7.7	The PrP's design mission Mach number for several CIs. . . . .	43
7.8	The CSR-01's design mission Mach number for several CIs. . . . .	43
7.9	The SAR of the PrP as a function of Mach number and altitude for $\tau = 84\%$ and $m = 106$ t. . . .	43
7.10	The PrP's design mission thrust for several CIs. . . . .	44
7.11	The CSR-01's design mission thrust for several CIs. . . . .	44
7.12	The PrP's altitude profile when leaving the initial cruise altitude freely optimisable for several CIs.	44
7.13	The PrP's Mach profile when leaving the initial cruise altitude freely optimisable for several CIs.	44
7.14	The PrP's mass when leaving the initial cruise altitude freely optimisable for several CIs. . . . .	45
7.15	The PrP's fuel consumption when leaving the initial cruise altitude freely optimisable for several CIs. . . . .	45
7.16	The PrP's absolute fuel consumption as a function of ZFM for several CIs. . . . .	45
7.17	The PrP's relative fuel consumption as a function of changes in ZFM for several CIs. . . . .	45
7.18	The PrP's absolute mission time as a function of ZFM for several CIs. . . . .	46
7.19	The PrP's relative mission time as a function of changes in ZFM for several CIs. . . . .	46
7.20	The PrP and CSR-01's harmonic mission 2D trajectories. . . . .	46
7.21	The PrP and CSR-01's harmonic mission Mach number. . . . .	46
7.22	The PrP and CSR-01's harmonic mission mass. . . . .	47
7.23	The PrP and CSR-01's harmonic mission fuel consumption. . . . .	47
7.24	The PrP and CSR-01 mission time as a function of CI and range. . . . .	47
7.25	The PrP and CSR-01 fuel consumption as a function of CI and range. . . . .	47
7.26	The PrP and CSR-01 fuel consumption per seat as a function of CI and range. . . . .	47
7.27	The PrP and CSR-01 fuel consumption per seat-kilometre as a function of CI and range. . . . .	47
8.1	The PrP's moveable deflections for several CIs. . . . .	49
8.2	The PrP's moveable deflections for several CIs in cruise. . . . .	49
8.3	The PrP's total lift increment due to DLC. . . . .	50
8.4	The PrP's total drag increment due to DLC. . . . .	50
8.5	The PrP's 2D trajectory, while enabling DLC. . . . .	50
8.6	The PrP's Mach profile, while enabling DLC. . . . .	50
8.7	The PrP's mass, while enabling DLC. . . . .	50
8.8	The PrP's fuel consumption, while enabling DLC. . . . .	50
9.1	The PrP and CSR-01 fuel consumption per seat-kilometre as a function of CI and range. . . . .	53
9.2	The PrP and CSR-01 mission time as a function of CI and range. . . . .	53

# List of Tables

2.1	The Top-level Design Requirement of the PrandtlPlane and CSR-01 aircraft. . . . .	8
2.2	The control surface specification of the PrandtlPlane semi-wing. . . . .	9
4.1	The grouping of variables into states and controls. . . . .	22
5.1	The PrandtlPlane’s design mission, with the active flight objectives, capture conditions, and path constraints per phase. . . . .	32
5.2	The boundaries imposed on the state and control variables in the design mission. . . . .	32
6.1	Comparison of optimal top-level performance metrics of the validation mission setups. . . . .	39



# List of Acronyms

---

<b>Notation</b>	<b>Description</b>
3DPM	3D Panel Method
AIM	Aeronautical Information Manual
AMC	Acceptable Means of Compliance
ASK	Available Seat Kilometre
ATC	Air Traffic Control
ATM	Air Traffic Management
BADA	Base of Aircraft Data
BWS	Best Wing System
CAS	Calibrated Airspeed
CDA	Continuous Descent Approach
CeRAS	Central Reference Aircraft data System
CFD	Computational Fluid Dynamics
CI	Cost Index
CPACS	Common Parametric Aircraft Configuration Schema
CS	Certification Specifications
CSR-01	CeRAS Short Range - Version 01
DLC	Direct Lift Control
DLR	Deutsches Zentrum fuer Luft- Und Raumfahrt
DOC	Direct Operating Costs
DoF	Degree of Freedom
EASA	European Aviation Safety Agency
EC	European Commission
EoM	Equation of Motion
ETOPS	Extended-range, Twin-engine Operational Performance Standards
EU	European Union
FAA	Federal Aviation Administration
FAP	Final Approach Point
FAR	Federal Aviation Regulations
FL	Flight Level
FPP	Flight Performance and Propulsion
GPOPS-II	General Purpose Optimal Control Software II
GSP	Gast turbine Simulation Program
IAS	Indicated Airspeed
ICAO	International Civil Aviation Organization
ICLOCS	Imperial College London Optimal Control Software
IHLG	Industry High Level Group
IPOPT	Interior Point Optimizer
ISA	International Standard Atmosphere

---

---

<b>Notation</b>	<b>Description</b>
KBE	Knowledge Based Engineering
LG	Legendre-Gauss
LGL	Legendre-Gauss-Lobatto
LGR	Legendre-Gauss-Radau
MDO	Multi-disciplinary Design and Optimisation
MINLP	Mixed-integer Nonlinear Programming
MMG	Multi-model Generator
MO	Maximum Operative
MTOM	Maximum Takeoff Mass
NLP	Nonlinear Programming
NM	Nautical Miles
OEM	Operational Empty Mass
ONERA	Office National d'Études et de Recherches Aéropatiales
OOP	Object-oriented Programming
PARSIFAL	Prandtlplane Architecture for the Sustainable Improvement of Future Airplanes
PHALANX	Performance, Handling Qualities and Loads Analysis Toolbox
PPC	Pure Pitch Control
PRE	Payload Range Efficiency
PrP	PrandtlPlane
RHS	Right-hand Side
RoC	Rate of Climb
RP	Range Parameter
SAR	Specific Air Range
SID	Standard Instrument Departure
TAS	True Airspeed
TLDR	Top-level Design Requirement
TSFC	Thrust-specific Fuel Consumption
TUD	Delft University of Technology
UML	Unified Modelling Language
VSAERO	Vortex Separation Aerodynamics
ZFM	Zero-fuel Mass

---

# List of Symbols

Symbol	Description	Units
<b>Roman letters</b>		
$A$	aspect ratio	[-]
$b$	wing span	m
$\mathcal{C}$	constraint function	
$C$	generic constant	
$C_D$	drag coefficient	[-]
$C_{D_0}$	zero-lift drag coefficient	[-]
$C_{D_2}$	lift-induced pressure drag coefficient factor	[-]
$C_L$	lift coefficient	[-]
$D$	drag	N
$e$	span efficiency factor	[-]
$\ell$	state dynamic equations	
$F$	force	N
$g$	(sea-level) gravitational acceleration	$\text{m s}^{-2}$
$h$	altitude	m
$\mathcal{J}$	cost functional	
$k$	lift-induced drag coefficient factor	[-]
$\mathcal{L}$	Lagrange (running) cost term	
$L$	lift	N
$m$	mass	kg
$M$	Mach number	[-]
$N$	reaction normal force	N
$n$	number	[-]
$P$	power	W
$p$	roll rate	$\text{rad s}^{-1}$
$q$	pitch rate	$\text{rad s}^{-1}$
$R$	radius	m
$r$	yaw rate	$\text{rad s}^{-1}$
$S$	wing area	$\text{m}^2$
$\mathbb{T}$	transformation matrix	
$T$	thrust	N
$t$	time	s
$u$	control variable vector	
$V$	velocity	$\text{m s}^{-1}$
$x$	state variable vector	
$X$	X axis	
$x$	eastward distance with respect to a reference point on the surface of the Earth	m
$Y$	Y axis	
$y$	northward distance with respect to a reference point on the surface of the Earth	m
$Z$	Z axis	
<b>Greek letters</b>		
$\alpha$	angle of attack	rad
$\beta$	angle of sideslip	rad
$\gamma$	flightpath angle	rad
$\Delta$	in- or decrement in ...	
$\delta$	deflection angle	rad

Symbol	Description	Units
$\Theta$	latitude	rad
$\theta$	pitch angle	rad
$\Lambda$	longitude	rad
$\mu$	aerodynamic angle of roll	rad
$\tau$	throttle setting	[-]
$\Phi$	Mayer (endpoint) cost term	
$\phi$	roll angle	rad
$\chi$	heading angle	rad
$\psi$	yaw angle	rad
$\omega$	angular velocity	rad s <sup>-1</sup>
<b>Subscripts</b>		
a	airpath	
ae	aerodynamic	
av	available	
b	body	
c	...at a collocation point	
cr	cruise	
cs	control surface	
E	Earth	
f	final	
gd	ground	
i	initial	
j	generic index	
$\ell$	lower	
p	...of (all) flight phases	
req	required	
rot	rotation	
sl	sea-level	
u	upper	
y	...in the y-direction	
<b>Superscripts</b>		
*	optimal solution of ...	
1	...in the 1 <sup>st</sup> phase	
f	...in the final phase	
p	...in the p <sup>th</sup> phase	

# Introduction

## Research context

Historically, the determination of aircraft trajectories and quantification of related performance metrics have always been of great interest to airlines for the obvious reasons of maximising aircraft performance and increasing profits. This ongoing interest has also served as a natural stimulant for the development of the field of aircraft trajectory optimisation. For instance, much research into optimal control has been funded by Boeing, such as Ref. [1].

Originating from the calculus of variations, optimal control theory has become the cornerstone of modern aircraft trajectory optimisation. Numerical approaches to optimisation problems, necessary for nearly all practical applications of optimal control, have branched into several specialised numerical resolution techniques, amongst which Nonlinear Programming (NLP). The applicability of these numerical techniques is intrinsically bound to the development of digital computers. Namely, whereas in the early 1960s problems with tens of decision variables and constraints were solved, present-day computers are able to solve problems with hundreds of thousands of constraints and decision variables [2].

Not only do airlines put this well-developed theory to good use, commercially, but trajectory optimisation is also indispensable in increasing aircraft operational efficiency to meet future sustainability goals. Ambitious goals are set for next-generation aircraft in road maps for the sustainable future of aviation, such as the European Commission (EC) Flightpath 2050 [3] and the Industry High Level Group (IHLG) Aviation Benefits [4] road maps. Both mention, amongst others, environmental impact minimisation and enhanced infrastructure robustness for future air passenger demand as important goals. More specifically, the Flightpath 2050 road map sets a 75 % cut in CO<sub>2</sub> emissions and a 90% NO<sub>x</sub> reduction per passenger kilometre as a goal for 2050 aircraft with respect to typical 2000s aircraft. Airbus mentions improved operations, potentially reducing CO<sub>2</sub> emissions by 10%, as one of four key pillars to meet sustainability goals [5].

Investigations into such operational improvements come in all shapes and sizes, a large part of which require trajectory analysis or optimisation to quantify the impact of a suggested improvement. For instance, Ref. [6] researches the potential benefits of allowing Continuous Descent Approaches (CDAs), an unconventional Air Traffic Management (ATM) procedure [7]. Moreover, the potential benefits of unconventional aircraft can be explored by assessing their mission performance using purely physics-based trajectory optimisation, as opposed to models that use empirically obtained coefficients, such as Base of Aircraft Data (BADA) [8].

In view of the demanding requirements imposed on next-generation aircraft, unconventional aircraft have received renewed attention lately as a possible solution towards a sustainable future for aviation [9]. Commercial aircraft have been designed according to the same tube-and-wing principle since World War II with drastically improved performance measures as a consequence: a doubling of the Payload Range Efficiency (PRE) and Range Parameter (RP), a 30% increase in transonic efficiency  $M(L/D)$ , and an 80% decrease in costs per ton-mile [10–12]. Unsurprisingly, the drastically improved, well-refined conventional aircraft design seems to have reached its maximum potential and its efficiency seems stagnant, as shown in Figure 1.1 [9, 11, 13, 14].

Contrarily, the PrandtlPlane (PrP) is an unconventional aircraft that might bridge the gap between the current aircraft design and the challenging future efficiency requirements. As discussed in Chapter 2, the PrandtlPlane Architecture for the Sustainable Improvement of Future Airplanes (PARSIFAL) project aims at designing such

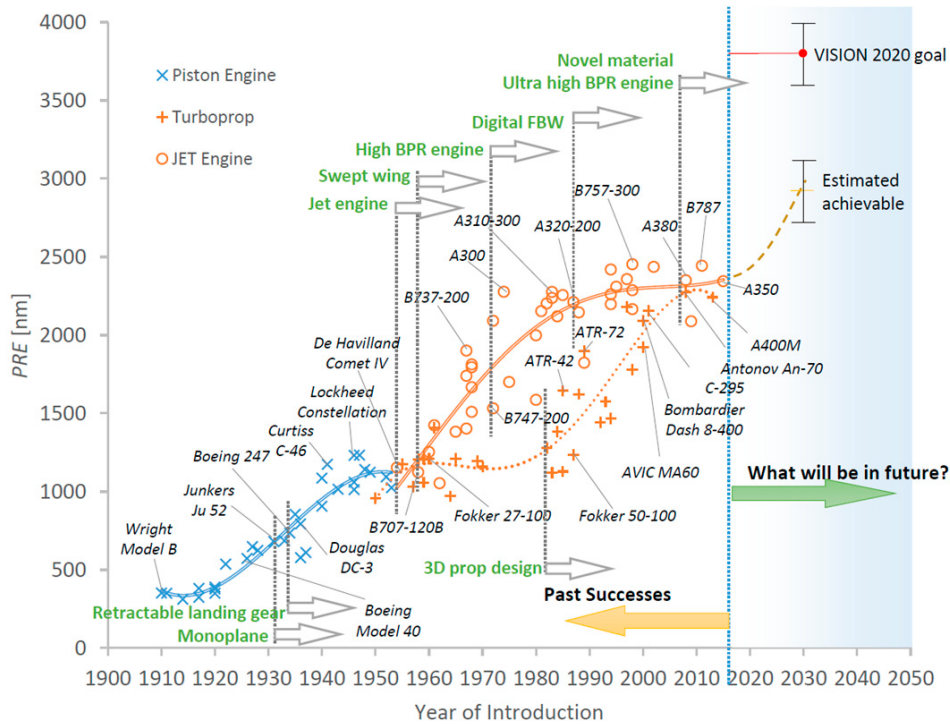


Figure 1.1: The historical development of the PRE. Image taken from Ref. [11].

a box-wing aircraft, funded by the European Union (EU) within the Horizon 2020 research- and innovation-boosting program.

The configuration is designed with redundant control surfaces and thus offers possibilities for unconventional flight control. Specifically, Pure Pitch Control (PPC) is possible without compromising the total lift by deflecting the front and rear control surfaces in phase opposition with the correct gearing. Contrarily, Direct Lift Control (DLC) without a change in pitching moment can be achieved by simultaneous downward deflection of the front and rear control surfaces [15, 16].

The PrP, its mission performance, and the potential mission-level benefits of unconventional flight control concepts are the subject of investigation of this thesis. Anticipating the specification of the research objectives and questions in the next section, the novelty of this research lies primarily in the mission performance evaluation of a box-wing aircraft in such a developed design stage. Moreover, the potential mission-level benefits of applying DLC have never been assessed, to the best of the author's knowledge.

## Research objectives and questions

Within the Flight Performance and Propulsion (FPP) department of Delft University of Technology (TUD), several tools intended for aircraft design and performance analysis are under continuous development. One of these tools is the Multi-model Generator (MMG), a Knowledge Based Engineering (KBE) application capable of generating a diverse range of aircraft configurations compliant with implemented engineering rules [17]. Coupling the MMG to analysis tools through discipline-specific report files allows evaluation of the current geometry and subsequent (automated) design improvements, essentially providing all necessary infrastructure for Multi-disciplinary Design and Optimisation (MDO). The relevance of this tool and its place in this work will be further elaborated upon in Chapter 3.

Another piece of software under development within the FPP department is the Performance, Handling Qualities and Loads Analysis Toolbox (PHALANX) [18, 19]. It is a multi-body flight dynamics simulation tool, especially apt for piloting simulation and aircraft dynamic response analysis.

The aim of this thesis is to *assess the globally optimal performance of a PrP, by developing a configuration-agnostic, multi-fidelity optimal control toolbox for performance and mission analysis*. The optimal control toolbox is developed as a branch within PHALANX, because the integral-mission performance analysis complements the quick-response performance assessment capability of PHALANX.

The main research objective is further broken down into secondary and tertiary research objectives as follows.

- (1) Develop a configuration-agnostic, multi-fidelity optimal control toolbox in MATLAB®.
  - (1.1) Develop a global aircraft trajectory optimisation toolbox within PHALANX.
  - (1.2) Verify and validate the models employed within the toolbox.
- (2) Assess the performance of the PrP with respect to its competitor aircraft.
  - (2.1) Assess the regular mission performance of the PrP with respect to its competitor aircraft.
  - (2.2) Assess the PrP's performance when enabling direct lift control.
- (3) Assess which of a selection of top-level design parameters has most influence on the aircraft's performance.

The main research question posed in this work is: *how does the PrP perform when flying its optimal mission, for a given range?* As anticipated at the end of the previous section, this performance analysis also comprises the trajectory analysis while enabling unconventional flight control, as indicated by the secondary Question (2).

- (1) How does PrP's optimal trajectory compare to competitor aircraft?
  - (1.1) How does the PrP's optimal state and control trajectory look?
  - (1.2) How does the PrP's performance compare to that of its competitor aircraft?
- (2) Does the enablement of direct lift control give the PrP a performance benefit over its competitor aircraft's performance?

## Thesis structure

This thesis is structured as follows. First, the origin of the box-wing aircraft concept, which serves as a foundation to the PARSIFAL project, is discussed in Chapter 2. In the same chapter, more information on the PARSIFAL project is given and the PrP performance knowledge gap that exists within the PARSIFAL project is discussed. Some of the research performed within this project, deemed relevant for the current work is highlighted here, too.

Subsequently, Chapter 3 presents the flight mechanics model that has been implemented within the trajectory optimisation program. Afterwards, some fundamental concepts in optimal control theory, the optimal control problem setup, and a justification for the chosen optimal control resolution approach is given in Chapter 4. Next, the implementation of the program into MATLAB® and the Object-oriented Programming (OOP) approach to modelling the mission and its flight phases are discussed in Chapter 5. The efforts made to validate the workings of this program are presented in Chapter 6.

The optimised mission profiles of the PrP are presented in the next two chapters. First, the results of several optimised aircraft missions of the PrP and its competitor aircraft are presented in Chapter 7. This encompasses several aircraft missions at various ranges, as well as a small study into the sensitivity of the PrP's top-level performance metrics to changes in its Zero-fuel Mass (ZFM) and initial cruise altitude. Subsequently, Chapter 8 addresses the impact of allowing DLC as a redundant means of controlling the PrP. Finally, the report is concluded in Chapter 9 with a summary of the most important findings and recommendations for future work.



# 2

## PARSIFAL Project

The aim of this chapter is to place the current work within the context of the PARSIFAL project. First, the historical background of the PrP and its basic principles are discussed in Section 2.1. Then, the requirements definition of the PrP as set up by the PARSIFAL team and the drivers behind those requirements are discussed in Section 2.2. Section 2.3 gives an overview of the studies performed within the PARSIFAL project relevant for this work. Finally, Section 2.4 aims at emphasising the relevance of the current work's research objectives within the PARSIFAL project.

### 2.1. Prandtl's Best Wing System

The aim of the PARSIFAL project is to design a commercial PrP. The PrP concept is based on a classic paper by Ludwig Prandtl, *Induced drag of multiplanes* [20]. As the title states, Prandtl investigated the lift-induced drag properties of wing systems with more than one wing, such as bi- and triplanes. Lift-induced drag is caused by vortex formation due to pressure gradients inevitably present on finite lifting bodies and is often, together with the pressure drag [21], modelled with the second term on the Right-hand Side (RHS) in Equation (2.1).

$$C_D = C_{D_0} + kC_L^2 \quad (2.1)$$

In his paper, Prandtl described his findings, which may be summarised in the following two points. First of all, the biplane arrangement with minimum induced drag is that arrangement with an elliptical lift distribution and equal lift on both wings. Moreover, the induced drag of this wing arrangement is lower than the induced drag of a monoplane with the same span and total lift.

Secondly, there exist optimum triplanes, which in turn have lower induced drag than a biplane with the same span and total lift. In the same way, multiplanes exist, with  $n$  up to  $\infty$  wings in theory, which have lower induced drag than a multiplane with one less wing. In any case, the total lift of each of the individual wings should be maximum at the outermost (top and bottom) wings and decrease to zero towards the symmetry plane (middle wing) to obtain minimum induced drag. This implies that the limiting case of the multiplane with infinite wings,  $n = \infty$ , has the lowest induced drag of all possible multiplanes, assuming the aforementioned loading of the individual wings.

Luckily, a more practical alternative to the practically impossible infinite-wing multiplane exists, with only two horizontal wings connected by vertical wings at the wing tips. This wing system is equivalent to the infinite wing system. Namely, for any large number of wings,  $n$ , in a wing system, each individual wing can be modelled by a simple horseshoe tip vortex. The role of this tip vortex, in turn, can be taken up by two vertical wings having a butterfly-shaped wing loading, connecting the two horizontal wings [22]. This results in a box-wing configuration, as shown in Figure 2.1, which Prandtl called the Best Wing System (BWS).

Although Prandtl used approximate methods to solve the problem of determining the configuration leading to minimum induced drag, his findings have later been confirmed. An exact solution to the minimum induced drag problem posed by Prandtl is presented in Ref. [22]. In this research, it was found that for practical applications of a box-wing system, where the box height over box width is approximately 0.1 – 0.2, Prandtl's solution is appropriate. Outside this range, however, Prandtl's approximation is too optimistic. This is confirmed by the contemporary investigation into induced drag of, amongst others, biplanes, too [23].

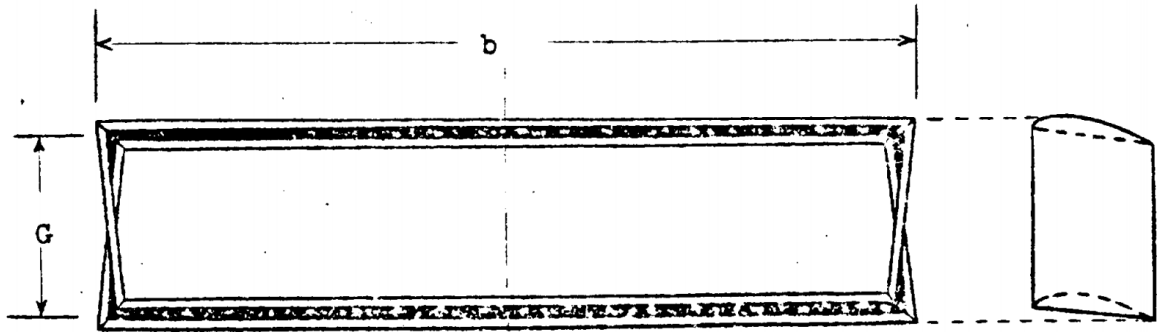


Figure 2.1: The BWS as drawn out by Prandtl. Image taken from Ref. [20].

Moreover, the induced drag of the wing system is independent of the streamwise separation of the individual lifting elements by Munk's stagger theorem [24]. This implies that the BWS indicated in Figure 2.1 has the same induced drag as an arrangement in which the bottom wing is located much more upstream than the upper wing, as will be seen in Section 2.3 is the case for the PARSIFAL aircraft configuration. In the same way, introduction of sweep and the resulting streamwise separation of lifting elements do not affect the wing's induced drag.

Yet another recent study has shown that the optimality condition for minimum induced drag is more relaxed than Prandtl's research initially indicated. Taking a coordinate system that runs along the closed wing system, starting at point A as shown in Figure 2.2, taking positive lift as pointing outwards, adding an arbitrary constant circulation to an initially optimal loading does not change the system's optimality. Namely, adding a constant value to the circulation does not affect the induced drag, because induced drag depends on *gradients* in pressure distribution and, hence, the circulation. As a result, the loading attributed to each of the wings can be modified according to design considerations other than induced drag, without compromising the induced drag performance.

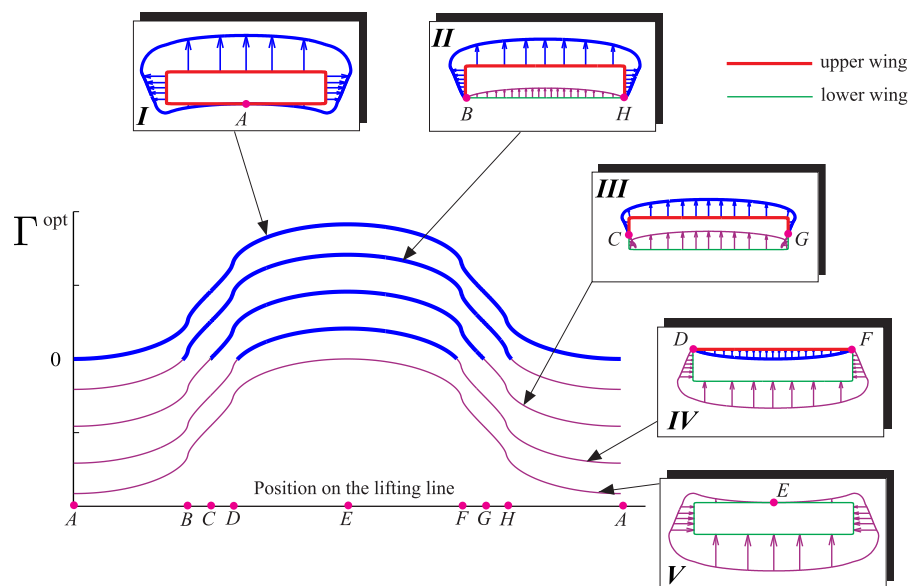


Figure 2.2: The wing loading optimality condition for minimum induced drag on a symmetric biplane. Image taken from Ref. [23].

## 2.2. Design Drivers and Requirements

As mentioned in Chapter 1, the PARSIFAL project fits well within a general trend of renewed interest in unconventional aircraft as a solution to increased sustainability in aviation. However, sustainability is only one of aviation's challenges for the near future.

A study performed by PARSIFAL partner Deutsches Zentrum Fuer Luft- Und Raumfahrt (DLR) as a foundation of the initial requirements analysis showed that a shift towards short-haul aircraft with more seats is expected [25, 26]. Specifically, flights with a range smaller than 4000 km are expected to generate most Available Seat

Kilometres (ASKs) [27], as shown graphically in Figure 2.3. This scenario agrees well with Airbus’s Global Market Forecast, which predicts the short-haul (up to 3000 Nautical Miles (NM)) segment to make up for 76% of all new aircraft deliveries in the next 20 years [5].

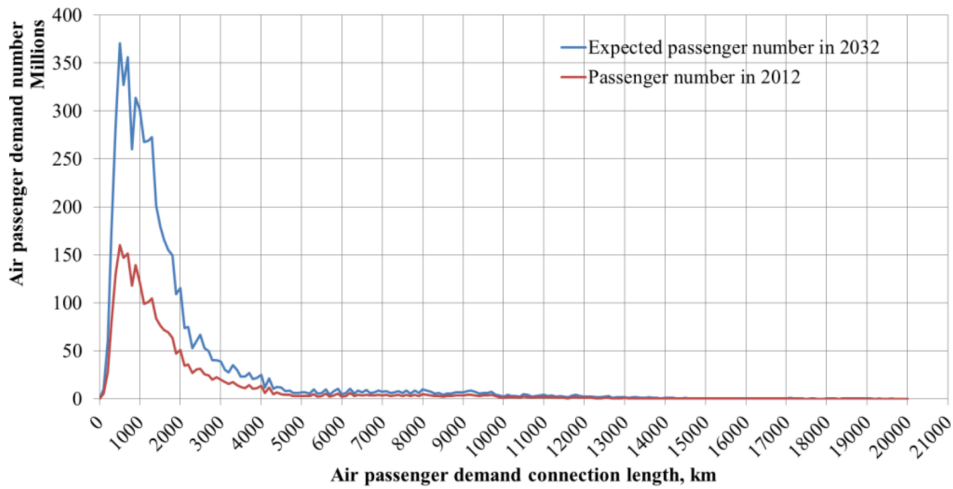


Figure 2.3: The forecast air passenger demand up to the year 2032. Image taken from Ref. [25]

The PARSIFAL project addresses the predicted rise in this range segment, by designing for a short-range, high passenger capacity aircraft. Specifically, the aircraft has a design mission range of 4000 km with a passenger capacity of 308 pax. This combination gives the aircraft a unique position in the market, as shown in Figure 2.4. With a passenger capacity comparable to an A330-300 and the range specification comparable to an A320-200, these aircraft are typically taken as reference aircraft within PARSIFAL researches.

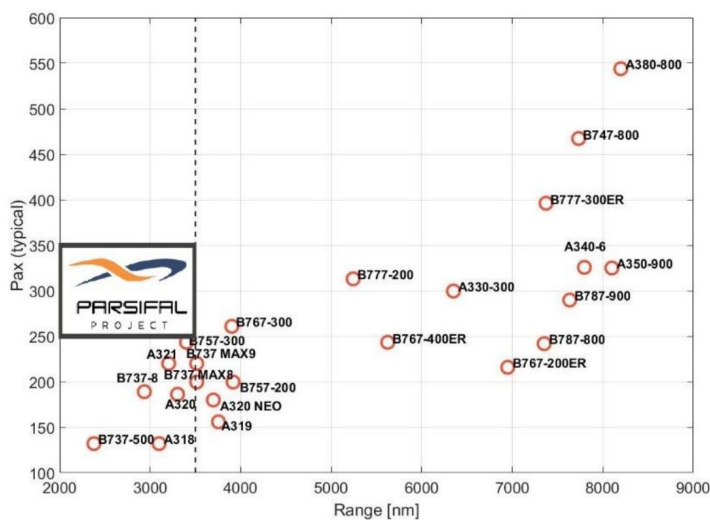


Figure 2.4: Passenger-range diagram showing the position of the PrP with respect to other aircraft. Image taken from Ref. [28].

With air traffic forecast to double in the coming 15 years, existing infrastructure will be pushed to its boundaries, as illustrated by Figure 2.5. Airports will meet their capacity limits and airport congestion is and will remain an ongoing challenge. With the forecast increase in ASKs, improvements in infrastructure alone are unlikely to resolve capacity issues. Moreover, the actual realisation of infrastructural improvements are of slow pace in many parts of the world due to, for example, political and environmental reasons [5].

To address this specific problem, the PrP has been designed for compatibility with existing infrastructure. Constrained to the 36 m wing span of an A320, the aircraft is compatible with many airports due to its International Civil Aviation Organization (ICAO) 4C aerodrome specification [29]. Other Top-level Design Requirements (TLDRs), amongst which the Maximum Takeoff Mass (MTOM), are given in Table 2.1.

## 2013 Aviation Mega-Cities\*



Source: IATA WSG database, Airbus GMF

Figure 2.5: Aviation mega-cities' airport congestion. Image adapted from Airbus.<sup>1</sup>

Reflecting on the research objectives discussed in the previous chapter and specifically Objective (2), it is noted that, in this work, an A320-like aircraft will be taken as a reference aircraft. Because of the typical data unavailability of aircraft aerodynamic and engine propulsive specifications, one nearly always needs to resort to alternative ways of modelling them. Developed as part of the Central Reference Aircraft data System (CeRAS), the CeRAS Short Range - Version 01 (CSR-01) will be used as competitor aircraft model [30] in this work, while the A330 is left out of the analysis for lack of an available alternative. Some TLDRs of this aircraft are also indicated in Table 2.1.

Table 2.1: The Top-level Design Requirement of the PrandtlPlane and CSR-01 aircraft.

Design variable	PrandtlPlane	CSR-01
MTOM	125 453 kg	79 000 kg
ZFM	98 453 kg	62 500 kg
OEM	69 193 kg	42 200 kg
$S$	266.7 m <sup>2</sup>	122.4 m <sup>2</sup>
$b$	36 m	34.1 m
$M_{cr}$	0.79	0.79
$h_{cr}$	11 km	11 km
passengers	308 pax	150 pax

## 2.3. Aircraft Component Sizing and Performance Analyses

The aim of this section is to present some of the work performed within the PARSIFAL project that is deemed relevant for this thesis. Specifically, the sizing of the control surfaces will be highlighted in Section 2.3.1, where their potential application to unconventional flight control concepts will be stressed. Afterwards, the initial aircraft performance analyses performed within the project are discussed.

### 2.3.1. Control Surface Sizing and Applications

In sizing the aircraft's control surfaces, use has been made of an iterative optimization scheme that tries to find the arrangement that minimises the total control surface span while satisfying certain handling qualities criteria

<sup>1</sup>URL <https://www.airbus.com/content/dam/corporate-topics/financial-and-company-information/Global-Market-Forecast-presentation-Andrew-Gordon-Redburn.pdf> [Accessed on 3 May, 2020]

[31]. This approach to control surface sizing, the outcomes of which are shown in Figure 2.6 for the PrP, is semi-empirical in nature and is computationally inexpensive. With instantaneous results at the cost of 35% error relative to the outcome of a high-fidelity approach, the method is especially applicable to the early design stages, where the aircraft design changes often and relatively much.

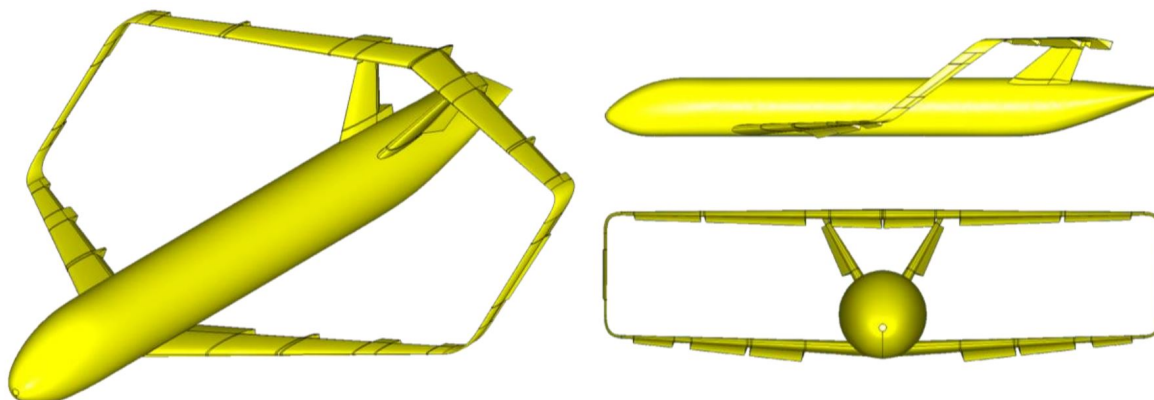


Figure 2.6: The baseline configuration of the PrP. Image taken from Ref. [31].

Contrary to the illustrative control surface layout depicted in Figure 2.6, the control surface specification as shown in Table 2.2 will be used in subsequent work in this thesis. The subscripts “in” and “out” denote the inboard and outboard locations of the respective control surface.

Table 2.2: The control surface specification of the PrandtlPlane semi-wing.

Wing	Moveable type	$\left(\frac{\eta}{b/2}\right)_{\text{in}}$	$\left(\frac{\eta}{b/2}\right)_{\text{out}}$	$c_{\text{in}}$	$c_{\text{out}}$
Front wing	Elevator	0.18	0.25	6.60 m	5.59 m
	Flap	0.30	0.75	5.19 m	3.11 m
	Aileron	0.80	0.95	2.88 m	2.18 m
Rear wing	Elevator	0.10	0.15	4.96 m	4.80 m
	Flap	0.24	0.75	4.50 m	2.82 m
	Aileron	0.80	0.95	2.65 m	2.16 m

Due to the control surface redundancy and configuration of the PrP, deflecting the control surfaces on both forward and rear wings to increase lift results in a zero net change in pitch couple, when the control surfaces are geared correctly [15, 16]. Contrarily, the pitch control of the PrP can be designed in such a way, that a pure couple, or PPC, is achieved without compromising the total lift, if the control surfaces are in phase opposition [10, 26].

The pure couple has as a main advantage that the manoeuvring precision can be increased and the safety is increased, especially in near-ground operations [10]. Because the total lift of the aircraft is not compromised, the aircraft can increase its pitch attitude without lowering the total lift and consequently its vertical position first. Contrarily, conventional aircraft are incapable of PPC; to change their pitch, they deflect the elevator upwards in order to increase the angle of attack, thereby first lowering total lift, after which the attitude is changed only sluggishly, especially for heavy aircraft.

With regard to DLC, three main advantages are identified [16]. First of all, it leads to improved flight path control precision during approach and landing. Secondly, using DLC for gust load alleviation the aircraft’s response to, for instance, atmospheric turbulence is improved. Thirdly, precision flight path control may be put to use for aerial refuelling. Moreover, DLC is especially favourable for aircraft with sluggish pitch control, because it is a means of controlling the Rate of Climb (RoC) that is, unlike controlling the RoC through aircraft pitch attitude, not slowed by the rotational inertia of the aircraft, only by its mass inertia [32, 33]. The PrP inherently has sluggish pitch control, because of the high pitch damping due to the box-wing’s staggered forward and rear wings [10, 15].

Some research has been conducted into the advantages of DLC for the PrP, as in Ref. [34]. However, the primary focus of this work has been on short-time manoeuvres, landing performance, and gust load alleviation. Moreover, the work has been written mainly from the perspective of control allocation and handling qualities, rather than mission optimisation.

### 2.3.2. Mission Performance Analysis

Within the PARSIFAL project, an initial assessment of the integral mission performance of the PrP has been performed [35]. The aircraft performance model used in this research, like any powered aircraft performance model, knows three necessary component.

The first component of the flight mechanics model is the physics, enforced through the Equations of Motion (EoMs). The research assumes a reduced point variable-mass model for an aircraft moving in the vertical plane only, while maintaining coordinated flight. For details, the reader is referred to Ref. [35].

Aerodynamically, the study takes the  $C_L$ ,  $C_D$  polars provided by Office National d'Études et de Recherches Aéronautiques (ONERA) as an input [36]. Because of their absence in the geometry at the time of the ONERA study, the drag contributions of the vertical tails and engines were accounted for by adding  $\Delta C_{D_0}$  components for each of the missing geometries to the aircraft drag.

As final component of the flight mechanics model, the propulsive model has been taken from generic models available in open literature, because no engine sizing had been performed for the PrP at that time. To model the thrust of the aircraft, the study employs slightly adapted versions of the widely used engine models proposed by Bartel and Young in Ref. [37]. The adaptations to this model were made in the model of the maximum available climb thrust and the cruise Thrust-specific Fuel Consumption (TSFC). Moreover, cruise thrust altitude lapse is modelled in correspondence with the models proposed by Raymer in [38].

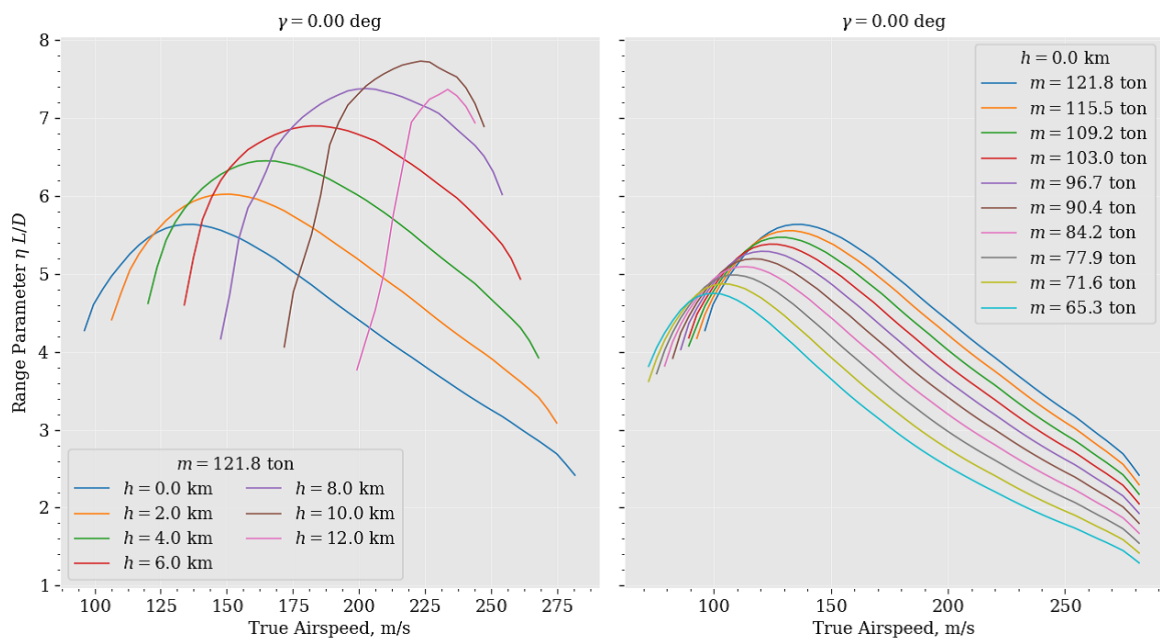


Figure 2.7: The RP plotted as a function of TAS, altitude, and aircraft mass. Image taken from Ref. [35].

With these three components, steady performance charts are derived that serve as a basis for the subsequent mission optimisation. An example of such a chart is given in Figure 2.7, where the product of the power plant and aerodynamic efficiencies, known as the RP, is shown as a function of True Airspeed (TAS), aircraft mass, and altitude. This chart shows what altitude and airspeed to fly at to maximise the RP and thereby the mission range for a given aircraft mass. In the same way, charts displaying  $P_{av}$  and  $P_{req}$  versus TAS and charts showing or  $T_{av}$  and  $T_{req}$  versus TAS for several  $h$  and  $m$  tell the combinations of altitude and velocity that optimise other mission performance metrics, at least in a point performance sense.

A time-stepping simulation is run by pre-defining the mission profile as a known sequence of flight phases, with the flight phase switches modelled as termination or capture conditions [39]. During mission definition, the user selects a flight strategy for each flight phase, such that a corresponding desired  $h$  and  $V$  to match that flight

strategy can be distilled from the performance charts. Augmenting the EoMs with a proportional controller, the aircraft is then steered towards the desired altitude and TAS. This yields a locally optimised aircraft trajectory, of which an example is shown in Figure 2.8.

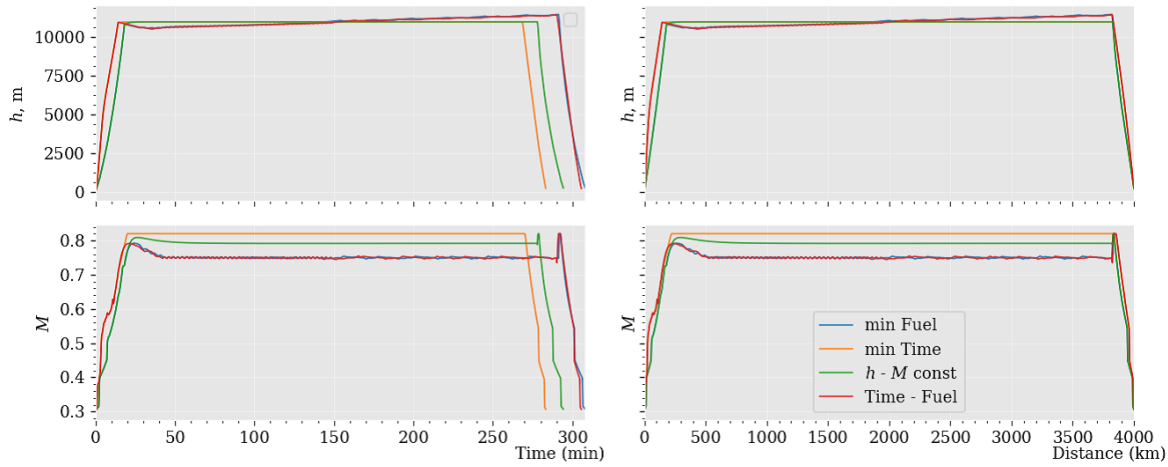


Figure 2.8: A non-diverted simulated mission profile for a range of 4,000 km. Image taken from Ref. [35].

Emphasising that the outcomes should not be taken as absolute values, because of the semi-empirical nature of the aircraft A320 and A330 models used, the local optimisation routine shows promising performance of the PrP in terms of fuel used per passenger for a given range. Though slightly slower, the PrP outperforms its competitor aircraft in terms of fuel burn per passenger-kilometre as seen in Figure 2.9. These promising results warrant the further investigation of the PrP’s performance in a global optimisation framework.

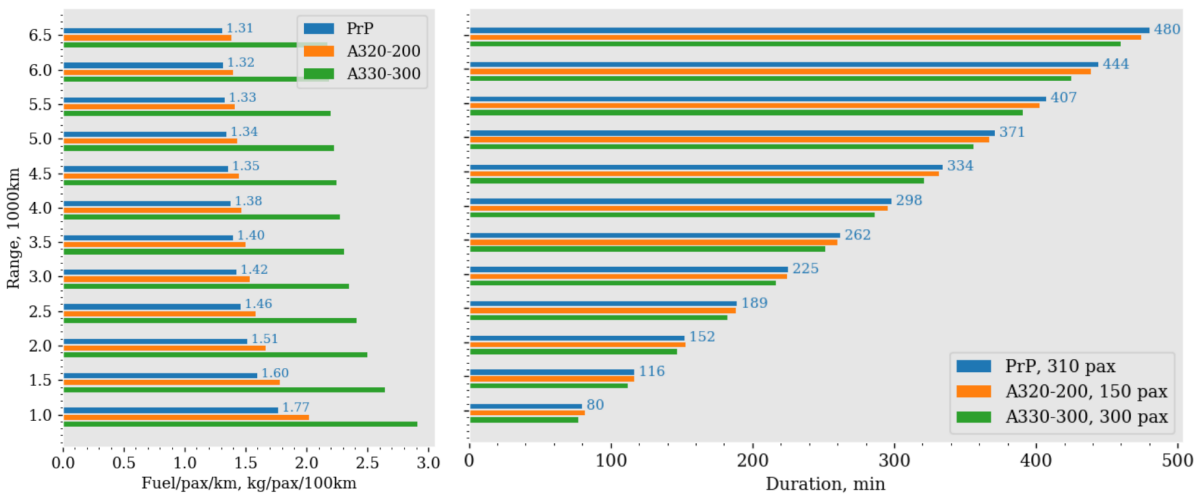


Figure 2.9: Fuel burn per passenger and mission duration for several ranges. Image adapted from Ref. [35].

## 2.4. Place of the Thesis within PARSIFAL

Having summarised the work performed to date within the PARSIFAL project, this subsection aims at reviewing the goals of the PARSIFAL project and viewing the research objectives mentioned in Chapter 1 in light of those goals. Specifically, the work package goals pertaining to aircraft mission and performance analysis as stated on the PARSIFAL project website are formulated as follows.<sup>2</sup>

- “Performance analysis (range, endurance, mission fuel, flight envelope limits, climb rate, turn rate, etc.) and mission profile optimization to gain most advantage of the best wing system”

<sup>2</sup>URL <http://parsifalproject.eu/project/> [Accessed on 1 September, 2019]

- “Exploration of advanced flight control concepts offered by the new control configuration (precision flight path control, maneuver/gust load alleviation)”

The first bullet point clarifies that *most advantage* should be gained by optimising the mission profile. This is an explicit call for global mission optimisation, as opposed to the local optimisation routine used up until this point, discussed in Section 2.3.2. This justifies the inclusion of Objective (2.1).

The second bullet point clarifies that the mission optimisation routine should be able to analyse unconventional flight control concepts enabled by the technological advances of the PrP. Combining this objective with the first bullet point, one may want to analyse unconventional trajectories enabled by the technological advantages of the PrP. For this reason, Objective (2.2) has been included in the research objectives.

# 3

## Flight Mechanics Model

The aim of this chapter is to give a description of the flight mechanics model at the core of the trajectory optimisation program. Any powered aircraft performance model needs three ingredients. Firstly, Section 3.1 deals with the EoMs, derived from first principles, that constitute the physics of the flight mechanics model. Secondly, the aerodynamic model and corresponding data acquisition method are discussed in Section 3.2. Thirdly and finally, the underlying propulsive model is the subject of Section 3.3.

### 3.1. Equations of Motion

In aircraft trajectory optimisation, several simplifying assumptions are customarily made in the derivation of the EoMs to reduce the computational complexity of the simulation. The full derivation of these EoMs will not be stated here, but the interested reader is referred to standard textbooks, such as Ref. [40]. The underlying assumptions, however, will be stated in Section 3.1.1. Some considerations in choosing the formulation of these EoMs in view of computational complexity are highlighted in Section 3.1.2.

#### 3.1.1. Simplifying Assumptions

The first simplifying assumption is that the aircraft is regarded as a point mass. This implies that rotational dynamics, such as trim equilibrium, cannot be modelled because of the zero moment arm length for a point mass. The main motivation for disregarding the rigid-body dimensions and, consequently, aircraft rotational dynamics is the consequent relief in computational complexity of the program. Confirmation of this approach is found in scientific literature; only single-maneuvre trajectories over a short time interval are typically optimised using computationally expensive, full-blown six-Degree of Freedom (DoF) EoMs that account for rotational accelerations and detailed attitude dynamics [41].

The second assumption is that the Earth is non-rotating, which yields tremendous simplifications to the full Newtonian equations in a non-inertial reference frame. Whereas generally, fictitious accelerations arise for mechanics in a non-inertial reference frame, these fictitious accelerations are neglected upon the assumption of a non-rotating Earth. Only minor errors (in the order of a tenth of a percent) arise when neglecting them. It should, however, be noted that disregarding the Coriolis acceleration over very large time intervals may result in a large cumulative error.

Thirdly, it is assumed that the aircraft is moving over a flat Earth, which has two major implications. First of all, it means that the centrifugal force coming from the - in reality - curvilinear motion of the aircraft is neglected. This is justifiable, because the centrifugal acceleration is much smaller than gravitational acceleration. The second implication is that the kinematic coordinates are not influenced by the (ellipsoidal) curvature of the Earth. The main reason for this simplification lies in that the purpose of this investigation is not to investigate realistic city-to-city trajectories, but to compare the performances of distinct aircraft on a generic mission.

Finally, it is assumed that the gravitational acceleration is constant, i.e.  $g = g_{sl}$ , and it is assumed that the thrust vector is perfectly aligned with the aircraft body axis, i.e.  $\alpha_T = 0$ .

Consequent to the flat, non-rotating Earth assumptions, the inertial reference frame that is used is the topocentric reference frame depicted in Figure 3.1. For illustrative purposes, the Earth-centred reference frame is displayed, too. Note how the topocentric coordinate system, with its origin at point E has a curved ordinate and

abscissa, following the surface of the Earth. Due to the flat Earth assumption, however,  $R_E \rightarrow \infty$  and the axes become cartesian.

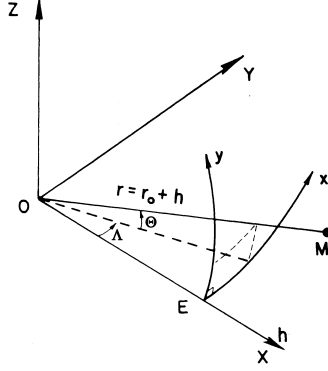


Figure 3.1: The topocentric ( $Exyh$ ) and Earth-centred ( $OXYZ$ ) reference frames, adapted from Ref. [40].

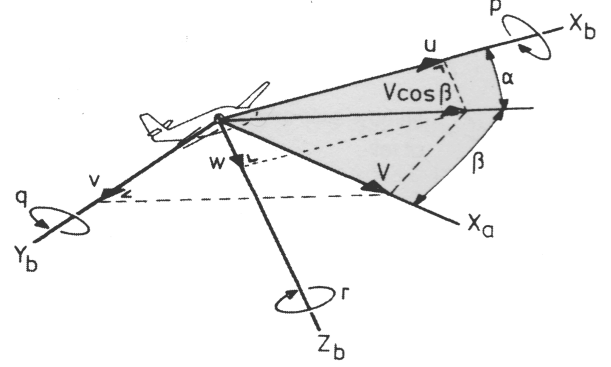


Figure 3.2: The body ( $X_b, Y_b, Z_b$ ) and (partial) airpath ( $X_a \parallel V$ ) reference frames, adapted from Ref. [42].

Generally, not all variables are expressed within the same reference frame. For example, aircraft aerodynamic data may be expressed in body frame coefficients, whereas the lift and drag are, per definition, defined in the airpath reference frame. Therefore, these quantities must be transformed from one coordinate frame to another using transformation matrices, where, for example,  $\mathbb{T}_X(\mu)$  indicates a rotation about the  $X$  axis by an angle  $\mu$  and  $\mathbb{T}_{ab}$  is shorthand notation for the transformation matrix from the body to aircraft coordinate frame. The derivation of these matrices will not be repeated here, but can be found in standard textbooks, such as Ref. [40].

### 3.1.2. Equations of Motion Formulation and Computational Complexity

The computer accuracy and speed demands involved with calculating the attitude angles are least when using an airpath formulation [43]. Nonetheless, the presence of the control variables (see Chapter 4)  $p$ ,  $q$ ,  $r$  might tempt one to express the aircraft attitude using a body formulation (the classic roll, pitch, and yaw angles), because of the well-known expression for the Euler angular rates as a function of the Euler angles and body angular rates [42], Equations (3.1). However, as will be illustrated next, this would be a computationally inefficient choice.

$$\begin{bmatrix} \dot{\phi} \\ \dot{\theta} \\ \dot{\psi} \end{bmatrix} = \begin{bmatrix} p + (q \sin \phi + r \cos \phi) \tan \theta \\ q \cos \phi - r \sin \phi \\ \frac{1}{\cos \theta} (q \sin \phi + r \cos \phi) \end{bmatrix} \quad (3.1)$$

Five angles out of  $\alpha$ ,  $\beta$ ,  $\gamma$ ,  $\mu$ ,  $\chi$ ,  $\phi$ ,  $\theta$ , and  $\psi$  are required to describe the attitudes of the body, airpath, and the inertial reference frames with respect to one another. Supposing  $\gamma$ ,  $\mu$ ,  $\phi$ ,  $\theta$ , and  $\psi$  are included in the state equations, one would need expensive matrix inversions to derive  $\alpha$  and  $\beta$  for calculating aerodynamic forces and  $\mu$  for determining the lift vector rotation. By coordinate transformation matrix manipulation, one can express these angles as in Equations (3.2), where the indices in the parentheses indicate the matrix element. Obviously, performing these operations upon each evaluation of the EoMs requires a lot of computational effort, illustrating why choosing the roll, pitch, and yaw angles as part of the states is undesirable.

$$\begin{aligned} \mathbb{T}_{Xb} &= \mathbb{T}_X(\mu) \mathbb{T}_{ab} = \mathbb{T}_Y(\gamma) \mathbb{T}_Z(\chi) \mathbb{T}_{Eb} \\ \alpha &= \arctan \frac{\mathbb{T}_{Xb}(1,3)}{\mathbb{T}_{Xb}(1,1)} \\ \beta &= \arcsin \mathbb{T}_{Xb}(1,2) \\ \mu &= -\arctan \frac{\mathbb{T}_{Xb}(3,2)}{\mathbb{T}_{Xb}(2,2)} \end{aligned} \quad (3.2)$$

Synthesising the above considerations, the EoMs are summarised in vector format as in Equations (3.3). The engine thrust and TSFC are functions of the altitude, Mach number, and throttle setting. The aerodynamics, meaning the lift and drag, and the reaction forces depend on the angle of attack, angle of sideslip, the Mach

number, and the angular rates. The derivations of the uncommon expressions for  $\dot{\alpha}$  and  $\dot{\beta}$  in Equations (3.3) are based on Ref. [43].

$$\dot{x} = \begin{bmatrix} \dot{h} \\ \dot{m} \\ \dot{V} \\ \dot{x} \\ \dot{y} \\ \dot{\mu} \\ \dot{\gamma} \\ \dot{\chi} \\ \dot{\alpha} \\ \dot{\beta} \end{bmatrix} = \begin{bmatrix} V \sin \gamma \\ -T \cdot \text{TSFC} \\ \frac{1}{m} \{ T \cos \alpha \cos \beta - (D_{ac} + D_{gd}) \} - g \sin \gamma \\ V \cos \gamma \sin \chi \\ V \cos \gamma \cos \chi \\ q \sin \beta + p \cos \alpha \cos \beta + r \sin \alpha \cos \beta \\ \frac{1}{mV} \left\{ T \sin \alpha + (N + L) \cos \mu - (F_{y_{ac}} + F_{y_{gd}}) \sin \mu - mg \cos \gamma \right\} \\ \frac{1}{mV \cos \gamma} \left\{ T \cos \alpha \sin \beta + (N + L) \sin \mu + (F_{y_{ac}} + F_{y_{gd}}) \cos \mu \right\} \\ \frac{1}{\cos \beta} \{ q \cos \alpha - p \sin \beta - \dot{\gamma} \} \\ \dot{\chi} + p \sin \alpha - r \cos \alpha \end{bmatrix} \quad (3.3)$$

These EoMs can easily be further simplified to accommodate trajectory analyses in which special types of flights are considered. For example, coordinated flight is obtained by setting  $\beta = 0$ , level flight is enforced by setting  $\gamma = 0$ , and 2D flight can be obtained by constraining  $\dot{\chi} = 0$  and  $\beta = 0$ . In a mission in which 3D flight should not be ruled out entirely, but only one or several flight phases should behave according to one of these special types of flight, one can impose these constraints on the full set of EoM, thereby giving some redundant equations. Alternatively, if the entire mission is 2D for example, the redundant equations can be removed entirely, leaving fewer DoF and thus a computationally lighter problem.

In the same way, the ground reaction forces are automatically set to zero in phases in which the aircraft is in flight. Contrarily, the ground reaction forces are calculated for the on-ground phases by solving for vertical and transverse equilibrium,  $\dot{\gamma} = \dot{X} = 0$ , thereby also giving some redundant equations.

## 3.2. Aerodynamic Model

This section aims at describing the model for the aerodynamic forces that appear in the EoMs described in the previous section. To this end, Section 3.2.1 dives into the assumed aerodynamic force decomposition and the method of aerodynamic data acquisition. Because of the unrealistic results obtained for the moveables' aerodynamics using this approach, a separate treatment of the high-lift and the control surface aerodynamics is discussed in Sections 3.2.2 and 3.2.3, respectively.

### 3.2.1. Force Decomposition

Following the approach in Ref. [31], the aerodynamic forces in Equations (3.3) are assumed to consist of three superimposed components. The first term in Equation (3.4) represents the aerodynamic force acting on a non-rotating body with control surfaces flush with the wing. The second term accounts for the contributions of control surface deflections, where, by superimposing all control surface forces, it is implicitly assumed that no control surface aerodynamic interdependence is present. The third and final aerodynamic component accounts for the aerodynamic forces that are a result of the aircraft rotational velocities.

$$F(\alpha, \beta, M, p, q, r, \delta_j) = F(\alpha, \beta, M, p = 0, q = 0, r = 0, \delta_j = 0) + \Delta F(\alpha, \beta, M, p = 0, q = 0, r = 0, \delta_j) + \sum_{\omega=p,q,r} \frac{\partial F}{\partial \omega}(\alpha, \beta, M, \delta_j = 0) \omega \quad (3.4)$$

It should be noted at this point that not all three aerodynamic force contributions are necessarily taken into account during the trajectory optimisation. Specifically, computational speed considerations may lead to disregarding the relatively short-duration component representing the aerodynamic force due to the aircraft's rotational velocity components. After all, the largest portion of the aircraft trajectory involves (near-)steady flight phases, such as cruise. Moreover, including each of the wing moveables' deflections as control variables may not always be desirable due to those same computational speed requirements. As will later be seen, however, some of the control surface deflections are put in the control vector for analysing the benefits of DLC in a brute-force mission optimisation approach.

The aerodynamic data are obtained by coupling several tools. First, an in-house MMG creates the aircraft geometry, based on an input Common Parametric Aircraft Configuration Schema (CPACS) file. The MMG, using KBE software, then automatically meshes the aircraft geometry and its wake to generate input files for Computational Fluid Dynamics (CFD) analyses [44]. Subsequently, these files are then passed to an inviscid, potential-flow 3D Panel Method (3DPM), called Vortex Separation Aerodynamics (VSAERO), which corrects for boundary layer effects.

The outcome of these analyses are tabular data for the aircraft's aerodynamic force and moment coefficients in the aircraft body reference frame. These tabular data have subsequently been corrected to remove outliers and to better match the  $C_{D_0}$  known from the CFD analyses by ONERA [36]. The respective clean lift and drag polars of the PrP and CSR-01 corresponding to the first term in Equation (3.4) are shown in Figures 3.3 and 3.4. Anticipating the requirements for the solver of the optimal control problem discussed in Chapter 4, the tabular data subsequently need to be interpolated in such a way, that they are twice continuously differentiable.

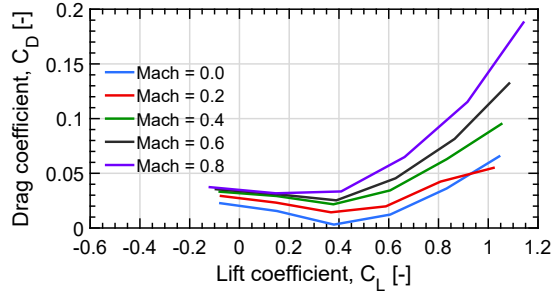


Figure 3.3: The lift-drag polar of the PrP as a function of Mach number for coordinated flight.

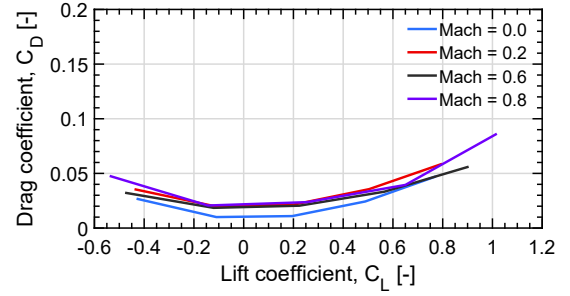


Figure 3.4: The lift-drag polar of the CSR-01 as a function of Mach number for coordinated flight.

Unfortunately, the aerodynamics due to control surface deflections, represented by the second term in Equation (3.4), aren't captured well by VSAERO in the case of the PrP. Possibly due to the box-wing's complex wing wake interactions, the drag especially seems to be underpredicted. In fact, upward deflection of the control surfaces results in a drag coefficient decrease, i.e. a net thrust increase, of approximately 40 counts for each front wing control surface and near 50 counts for each rear wing control surface for a wing half. Obviously, these results are unrealistic and as an input to a trajectory simulation, will not yield any realistic results. Putting this to the test showed that indeed, a near fuel-free mission could be flown using these data as an input.

### 3.2.2. High-Lift Devices Aerodynamic Modelling

Therefore, a more robust, alternative approach is taken to modelling the control surface aerodynamics, necessary for amongst others high lift. Contrary to other modelling approaches, such as BADA, in which the coefficients of a parabolic drag polar are given for a specific aircraft configuration, the tabular data don't allow such an approach. Instead, a configuration-constant  $\Delta C_L$  and  $\Delta C_{D_0}$  due to high-lift devices deployment are added to the tabular data  $C_L$  and  $C_D$ , respectively.

The high-lift configuration  $\Delta C_L$  that is taken henceforth in this study is based on Equation (3.5). This approach will also further be put into context in Section 6.1.2. Specifically, it is assumed that the lift coefficient increase at a given angle of attack in the high-lift configuration, either takeoff or landing, is  $\Delta C_L = 0.6$ , based on a conservative representation of the  $C_{L_{\max}}$  values reported in Ref. [45]. The same value is taken for the PrP and the VSAERO control surface lift coefficient data, more reliable than the drag data, indicate that this value is feasible. Note that the CSR-01 VSAERO model is only equipped with one main wing control surface, giving a maximum  $\Delta C_L$  of only 0.2. Obviously underequipped for takeoff and landing, this model is thus of no use in providing information on the feasibility of the assumed  $\Delta C_L = 0.6$ . Nonetheless, Ref. [46] indicates that this value is reasonable and even somewhat conservative.

$$\Delta C_{L_{\text{config}}} = C_{L_{\text{max,config}}} - C_{L_{\text{max,clean}}} \quad (3.5)$$

Moreover, Ref. [46] provides values for  $\Delta C_{D_0}$  for the aircraft configurations corresponding to takeoff, initial climb, approach, and landing for several aircraft models, amongst which the A320. Henceforth, the high-lift configuration  $\Delta C_{D_0}$  is taken as the takeoff  $\Delta C_{D_0} = 0.055$ , for both the PrP and A320, unless otherwise stated.

### 3.2.3. Control Surface Aerodynamic Modelling

To model the control redundancy resulting from introduction of DLC as a primary means of control, the control vector  $u$ , as will be explained in Section 4.1.2, has to be augmented with the control surface deflections  $\delta_j$ . As a result, the aircraft is redundantly controllable through the pitch rate  $q$  and the control surface deflections  $\delta_j$ . As previously indicated, this approach is very much a brute-force approach and because rotational dynamics are still not accounted for to limit computational effort, the underlying assumption is that the combinations of control surface deflections allow to generate the required pitch rate at any instant.

The control surfaces of the PrP that are assumed to take part in controlling DLC are the front and rear wing elevators and ailerons, but not the flaps. The flaps are excluded from DLC, because they are assumed to generate the high-lift increment, explained in Section 3.2.2. The DLC moveables are limited to  $\delta_j = \pm 15^\circ$  deflections to respect the boundaries of the experimental data in Figure 3.5 and the control surfaces are assumed to deflect symmetrically about the symmetry plane of the aircraft. The trailing edge control surfaces' specifications are summarised in Table 2.2. Note that the chord lengths indicated in the table denote the local wing chord length, not only the control surface chord.

Subsequently, the control surface deflections  $\delta_j$  have to be mapped to a corresponding lift and drag coefficient increment,  $\Delta C_L$  and  $\Delta C_D$ , respectively. This contribution to the resultant aerodynamic force is essentially the same as the second term in Equation (3.4). However, an alternative way to model this term is used, because the drag obtained through VSAERO is too unrealistic, as discussed in Section 3.2.1. To have a consistent aerodynamic control surface model, the incremental lift is modelled in the same way.

Several models mapping the control surface deflections to the corresponding aerodynamic force increments were tried to no avail. One of these models gives  $\Delta C_L$  and  $\Delta C_D$  as a function of flap deflection and some geometric parameters through a semi-empirical relation [47]. In another approach, the two-dimensional incremental lift and drag due to moveable deflections of wing cross-sections at several stations were obtained with XFOIL [48]. However, neither approach captured compressible wave drag effects well enough, thereby overestimating the attainable incremental lift at low drag.

To this end, an empirical approximation that gives the incremental lift coefficient  $\Delta C_L$  and the incremental drag coefficient  $\Delta C_D$  due to a flap deflection is used. Ref. [49] presents the experimentally obtained 2D incremental lift and drag properties of a flat plate with a plain trailing edge flap in compressible flows as a function of  $M\delta$ .

Although representing the aerofoil by a flat plate is a crude approximation, it is not the aim of this thesis to model the control surface (transonic) aerodynamics in detail. The purpose of this model is to have a realistic enough approximation to the attainable lift and the associated drag. Adopting this approach does allow capturing transonic wave drag and drag rise effects dominant in the high subsonic regime. Because the flat-plate analysis holds for a zero angle of attack, the dependency of  $\Delta C_D$  and  $\Delta C_L$  on  $\alpha$  are neglected in subsequent analyses.

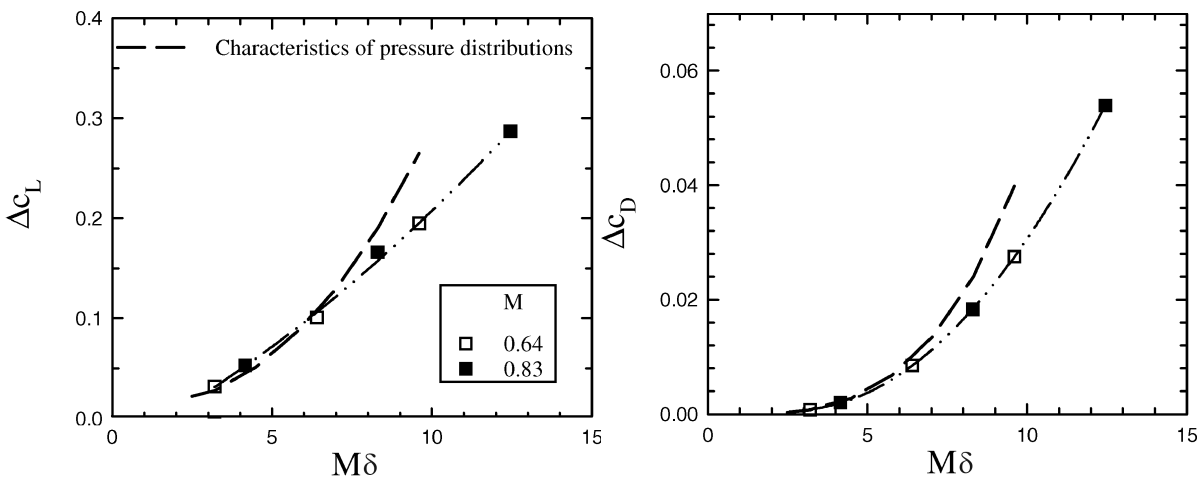


Figure 3.5: The incremental lift and drag as a function of  $M\delta$ , with  $\delta$  in degrees. Image adapted from Ref. [49].

A quadratic fit to the  $\Delta C_D(M\delta)$  and a linear fit through the  $\Delta C_L(M\delta)$  data presented in Figure 3.5 are used. Subsequently, the aerodynamic coefficients corresponding to each control surface are obtained by correcting for the ratio of the area of the flapped wing portion to the aircraft reference area, as shown in Equation (3.6).

$$\begin{aligned}\Delta C_{L_{cs}} &= 2.017 \cdot 10^{-2} \cdot M \delta \frac{S_{\text{flapped}}}{S_{\text{ref}}} \\ \Delta C_{D_{cs}} &= 3.186 \cdot 10^{-4} \cdot (M \delta)^2 \frac{S_{\text{flapped}}}{S_{\text{ref}}}\end{aligned}\quad (3.6)$$

Several shortcomings of using this 2D flat plate approximation must, however, be corrected for. Because the proposed model gives 2D drag components, the zero-lift drag and pressure drag are modelled reasonably well with respect to a 3D wing. However, because a 2D aerofoil essentially constitutes an infinite wing, vortex drag effects are not captured at all. Therefore, an additional penalising vortex drag term, as shown in Equation (3.7), is added to the  $\Delta C_D$  previously described. This breakdown of the drag into separate lift-induced pressure and lift-induced vortex drag is uncommon due to the difficultly distinguishable contributions of both because of their respective proportionalities to  $C_L^2$ , but this separation is physically sound [21].

$$\begin{aligned}C_D &= \overbrace{C_{D_0}}^{\text{zero-lift drag}} + \overbrace{C_{D_2} C_L^2}^{\text{pressure drag}} + \overbrace{\frac{C_L^2}{\pi A e}}^{\text{vortex drag}} \\ C_D + \Delta C_D &= C_{D_0} + \Delta C_{D_0} + C_{D_2} (C_L + \Delta C_L)^2 + \frac{(C_L + \Delta C_L)^2}{\pi A e} \\ \Delta C_D &= \underbrace{\Delta C_{D_0} + C_{D_2} (2C_L \Delta C_L + \Delta C_L^2)}_{\text{2D drag components}} + \underbrace{\frac{2C_L \Delta C_L + \Delta C_L^2}{\pi A e}}_{\text{3D vortex drag correction}}\end{aligned}\quad (3.7)$$

Investigation of the individual terms of  $\Delta C_D$  in Equation (3.7) shows that special attention should be given to the final term. The first two terms constitute the 2D drag components, which are assumed to be represented by the approximation for the 2D incremental drag in Equation (3.6). In the latter 3D vortex drag term, a value of 1.46 is taken for the span efficiency factor  $e$ . This value is based on Ref. [50], in which the span efficiencies of several unconventional aircraft configurations are given, as shown in Figure 3.6.

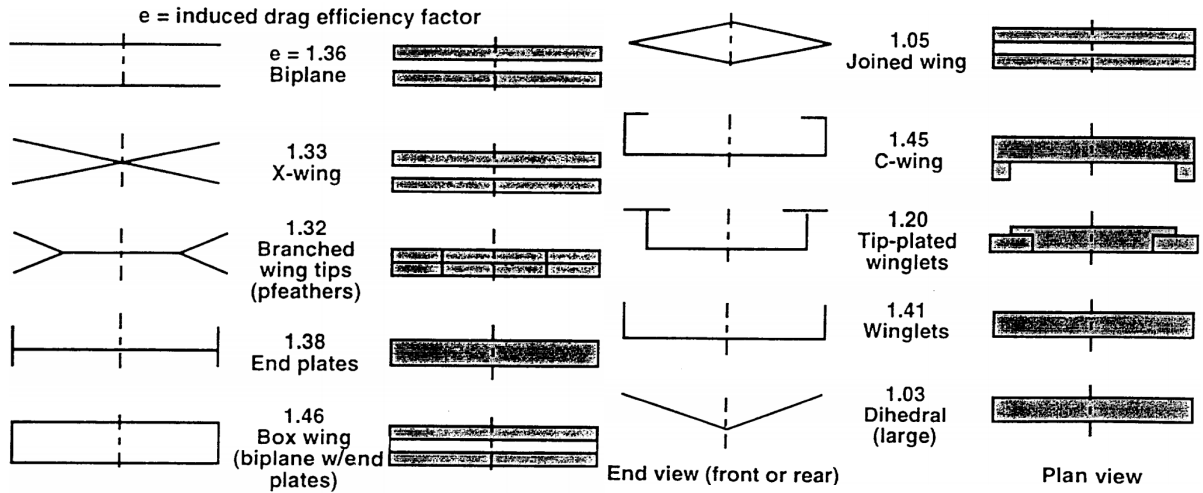


Figure 3.6: The span efficiencies of several unconventional aircraft configurations. Image adapted from Ref. [50].

### 3.3. Propulsive Model

The engine model, necessary to complete the flight mechanics model, that is used in the trajectory optimisation program is created using GTPy [51]. It is an in-house, component-based gas turbine analysis tool, that evaluates off-design performance by coupling to the Gast turbine Simulation Program (GSP) [52]. Through KBE software, the engine can be sized preliminarily, its mass estimated, and its geometry modelled such that its effect on aircraft

aerodynamics, mass and balance, and noise can be investigated. As a result, an informed tradeoff can be made between engine designs, while taking into account multidisciplinary considerations.

In order to allow fair comparison between the PrP and its competitor aircraft, the CSR-01 has been with a modern LEAP-1 engine. Originally, the CeRAS namely doesn't provide any engine specifications for the CSR-01.

In the same fashion as before, these propulsive analyses yield individual data points for several combinations of altitude, Mach number, and throttle setting. Like before, these tabular data must be interpolated to get the TSFC and thrust as a  $C^2$  continuous function. The maximum available thrust maps of the PrP and CSR-01 are shown in Figures 3.7 and 3.8, respectively.

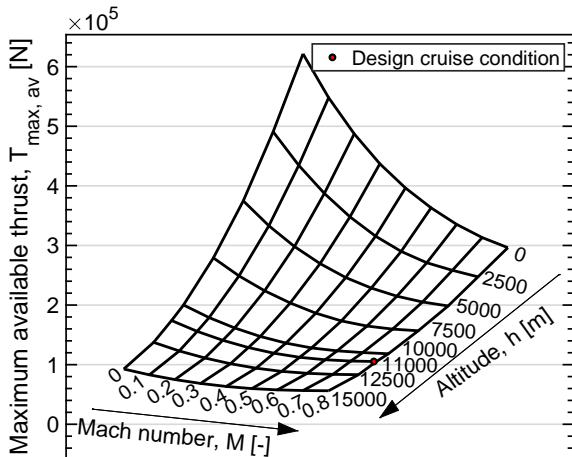


Figure 3.7: The maximum available thrust of the PrP as a function of altitude and Mach number.

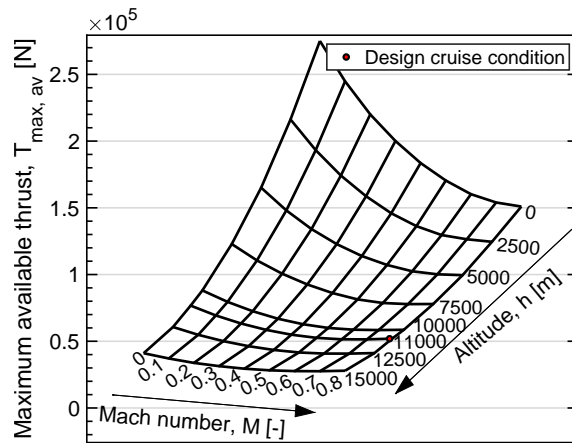


Figure 3.8: The maximum available thrust of the CSR-01 as a function of altitude and Mach number.

The TSFC at maximum throttle as a function of altitude and Mach number is shown in Figures 3.9 and 3.10 for the PrP and CSR-01, respectively. Each engine of the PrP has a TSFC of  $1.40 \times 10^{-5} \text{ kg N}^{-1} \text{ s}^{-1}$  at maximum throttle and at cruise conditions, whereas the CSR-01 has a TSFC of approximately  $1.47 \times 10^{-5} \text{ kg N}^{-1} \text{ s}^{-1}$  at the same conditions.

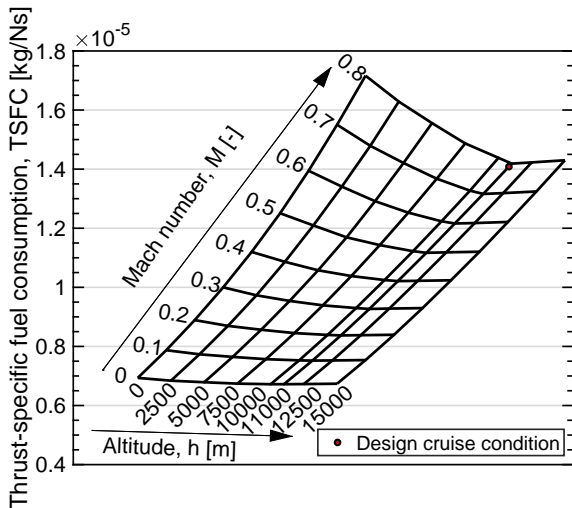


Figure 3.9: The TSFC of the PrP as a function of altitude and Mach number at maximum thrust.

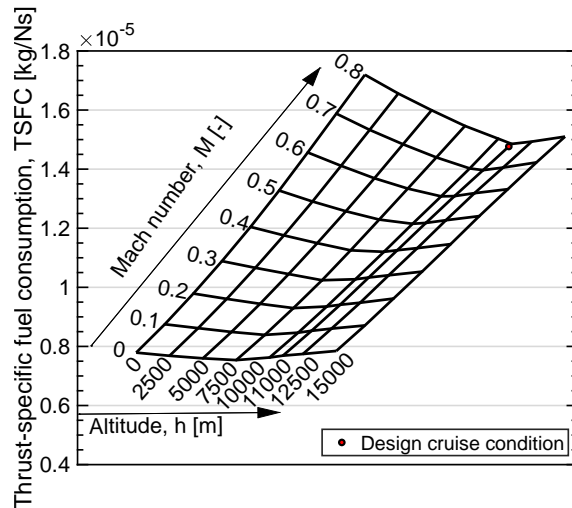
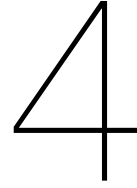


Figure 3.10: The TSFC of the CSR-01 as a function of altitude and Mach number at maximum thrust.





# Optimal Control Theory

This chapter aims at providing a basic understanding of optimal control theory, as it lies at the heart of this research. Note that it is not the intention to provide an exhaustive review on branches of optimal control or to dive into specifics on the numerical implementation of optimal control solution approaches. For an elaborate reference about optimal control, standard textbooks such as Ref. [53] can be consulted.

## 4.1. Fundamentals of Optimal Control

Optimal control theory provides an intuitive approach to aircraft trajectory optimisation not only because the trajectory can be split into multiple phases, but also because control and state variables are naturally distinguished. Let  $u$  denote the control variable vector and, as before,  $x$  the state variable vector. The goal of any optimal control problem is then to find the time histories  $x^*(t)$  and  $u^*(t)$  that minimise the cost functional  $\mathcal{J}$  to  $\mathcal{J}^*$ , simultaneously respecting the problem constraints.

### 4.1.1. Multiphase Problem Formulation

The cost functional  $\mathcal{J}$  is composed of two terms in the most general Bolza objective formulation. The first term  $\Phi$  in the summation sign in Equation (4.1) represents the Mayer end-cost term, whereas the second term represents the Lagrange running cost. The integral-mission cost is then obtained as the sum of the individual phases' costs.

$$\mathcal{J}(x, u, t) = \sum_{p=1}^{n_p} \left[ \Phi^p \left( x_{t_i}^p, t_i^p, x_{t_f}^p, t_f^p \right) + \int_{t_i^p}^{t_f^p} \mathcal{L}(x(t), u(t), t) \right] \quad (4.1)$$

For typical integral-mission analyses, the mission cost functional is set to minimise a combination of the total flight time and fuel consumption. By defining a Cost Index (CI) as in Equation (4.2) [54], the monetary value of fuel use can be traded off against the aircraft turnaround time, which is an indicator of the Direct Operating Costs (DOC). Using the CI, the overall mission cost can simply be determined as in Equation (4.3). Evidently, a zero CI will drive the trajectory to its minimum-fuel solution. Contrarily, the trajectory will go to its minimum-time solution as the CI goes to infinity.

$$CI = \frac{\text{Time cost [$/s]}}{\text{Fuel cost [$/kg]}} \quad (4.2)$$

$$\mathcal{J} = m_i^1 - m_f^f + (t_f^f - t_i^1) CI \quad (4.3)$$

Naturally, the physical system will have to obey a set of governing EoMs in the form of differential algebraic equations. They are the previously discussed EoMs, Equations (3.3), written as Equation (4.4) in vector format. Note that in Equations (3.3), it might seem as if  $\dot{x}$  is a function of some of its own vector elements,  $\dot{\gamma}$  and  $\dot{\chi}$ , thereby requiring an iterative solution approach. However, either by solving sequentially or by expressing  $\dot{\gamma}$  and  $\dot{\chi}$  in terms of the states and controls directly on the RHS, no iteration is required.

$$\dot{x}^p = f(x^p(t), u^p(t), t) \quad (4.4)$$

Additionally, path constraints can be imposed to restrict the continuous-time admissible trajectories in a phase. In general, these constraints can be formulated as in Equation (4.5). Note that setting equal lower and upper bounds,  $C_\ell = C_u$ , essentially transforms the inequality constraint into an equality constraint.

$$C_{\ell,j}^p \leq \mathcal{E}_{\text{path},j}^p(x(t), u(t), t) \leq C_{u,j}^p \quad (4.5)$$

Finally, phase boundary conditions can be imposed on the state variables or time either directly by prescribing their values or indirectly by defining an initial and endpoint or, equivalently, event constraint function that should be satisfied, as in Equation (4.6). In general, multiphase optimal problems do not necessarily impose that the states and even the time be continuous at phase boundaries. Therefore, phase linkage constraints are an indispensable instance of event constraints. Namely, they impose continuity on the time and states at the phase interfaces by requiring that at the end of phase  $p$  and at the start of phase  $p+1$ , the state variables and the time should be equal. That is,  $t_f^p = t_i^{p+1}$  and  $x_f^p = x_i^{p+1}$ .

$$C_{\ell,j}^p \leq \mathcal{E}_{\text{event},j}^p(x_{t_i}^p, t_i^p, x_{t_f}^p, t_f^p) \leq C_{u,j}^p \quad (4.6)$$

One should simply think of the phase linkage function as a specific instance of  $\mathcal{E}_{\text{event},j}^p$  that returns the difference of two phases' trajectories at their common boundary, as illustrated by Figure 4.1. By setting  $C_{\ell,j}^p = C_{u,j}^p = 0$ , i.e. an equality constraint, the trajectory must be continuous at the boundary. Apart from enforcing continuity, one could also deliberately allow trajectory discontinuity at a phase boundary by setting an inequality instead of equality constraint. An example situation in which this might be useful is to simulate an aircraft instantaneously jettisoning fuel. Because the sequentiality of phases is merely guaranteed by their linkage, one could even link multiple phases, in the same way as phase 2 is connected to phases 3 and 5 in Figure 4.1. Possibly useful for simulating the decoupling of the modules of a multistage rocket, such linkage has little application for commercial aircraft trajectories.

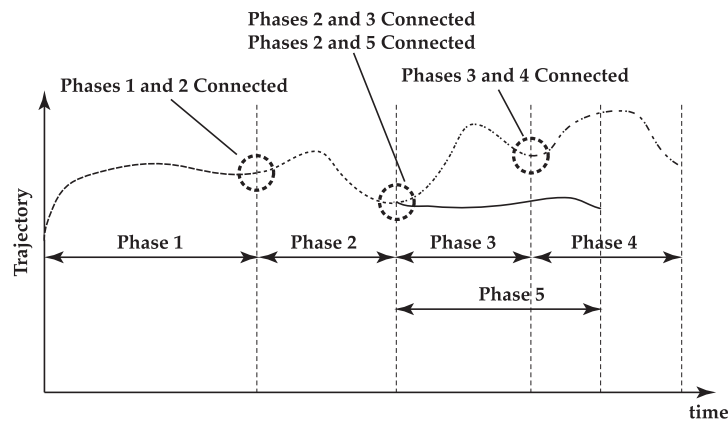


Figure 4.1: An impression of phase linkage. Image taken from Ref. [55].

### 4.1.2. State and Control Vector Definitions

With the distinction between control and state variables comes the important choice of which variables to put in which group, but also which variables to put in neither group. In principle, this choice can be made in many ways, as long as the state rates can be expressed as Equation (4.4) and the chosen system is not over- or underconstrained. However, as the example in Section 3.1.2 showed, some categorisation choices are better than others. Moreover, the importance of the straightforwardness of this choice, for example for code understanding and maintenance, should also not be underestimated. The grouping that has been chosen in this work is shown in Table 4.1.

Table 4.1: The grouping of variables into states and controls.

Group	Variables
State variables $x$	$h, m, V, x, y, \mu, \gamma, \chi, \alpha, \beta$
Control variables $u$	$\tau, p, q, r$

For a large part, the definition of the state variables is based on their being commonplace in aeronautical engineering and on the ease of understanding the expressions of their rates in the form Equation (4.4). As explained in more detail in Section 3.1.2, the computational effort as a result of choosing  $x$  and  $u$  might differ from one choice to another and thus also plays a role. As such, placing variables in one or neither group cannot easily be seen apart from the definition of the EoMs. Some variables, however, like the altitude, TAS, and the aircraft mass are so commonplace, that they are naturally included in the states.

Another consideration that plays a role in the variable grouping is that tight bounding of the state variables reduces the computational effort involved in resolving the problem, whereas adding path constraints increases it. Highlighting the choice for including  $\alpha$  as state variable, imposing bounds on this state, e.g. to prevent the aircraft from flying at an  $\alpha$  that would cause stall, reduces computational effort. Alternatively, if  $\alpha$  hadn't been part of the states, a computationally expensive constraint  $\alpha < \alpha_{\text{stall}}$  should have been added for all flight phases.

One consideration in defining the control vector is the degree to which the variables included are controlled variables in real life. For this reason, the engine throttle setting  $\tau$ , assumed the same for all engines and hence allowing no differential thrust, is included in the control variables. To model the aircraft as accurately as possible one would ideally also include the other pilot controls in  $u$ , either in the form of actual stick commands or in the form of control surface deflections. For the reasons mentioned in Section 3.1.1, this is not an option, however.

As a result, the aircraft model has to be reduced or "cut off" at some point and already mentioned in Section 3.1.2 and Table 4.1, it has been chosen to model the attitude controls by the aircraft's angular rates. There are two main reasons for making the rotational velocities instead of, for example, the attitude angles the control variables. First of all, by modelling the attitude control by the body rotational velocity components, the effects of these rotations on the aerodynamic coefficients, modelled by the second term in Equation (3.4), can be included. Secondly, by controlling the attitude rates instead of angles, instantaneous jumps from one aircraft attitude to another can be prevented. This is easily done by setting appropriate rate limits on the control variables  $p, q, r$ .

### 4.1.3. Excessive Control Penalisation

Similarly, the formulation with the attitude rates in the controls allows limiting of excessive control use. Because of the linearly appearing controls in the EoMs, bang-bang control can occur, where the control variables "bounce" between their respective upper and lower limits. A common fix to this non-physical behaviour is to add an excessive control penalisation term, Equation (4.7), to the objective functional Equation (4.1). The constant  $C_u$  is a measure for the severity of the control penalisation. Generally, setting a very small value for  $C_u$  suffices, because it makes the EoMs non-linear in the controls. As a result, the term's impact on  $\mathcal{J}^*$  is negligible [56].

Note how the square of the controls is taken to equally penalise rotation of the aircraft in either direction. Moreover, note how adding this term would not have been possible if the attitude had been controlled with attitude angles instead of rates; after all, penalisation of a non-zero attitude would undesirably steer the aircraft towards zero pitch and angle of attack.

$$\mathcal{J}_u = C_u \int_{t_i}^{t_f} (p^2 + q^2 + r^2) dt \quad (4.7)$$

Even though it has not been applied in this research to limit computational complexity, one could also limit excessive throttle control use. By introducing a so-called pseudo-control, which does not necessarily have a very intuitive physical meaning, one can add a term  $\dot{\tau}^2$  to the integrand in Equation (4.7). Then,  $\tau$  becomes a state and any excitation of the throttle setting will be penalised (slightly), in the same way as the rotational control variables described above.

## 4.2. Transcription Methods

Several gradient-based strategies exist for solving the continuous-time optimal control problem as posed in the previous section. On the uppermost level, these approaches are classified on the basis of two characteristics: the set of optimal control equations that is discretised, discussed in Section 4.2.1, and the set of variables that is discretised, discussed in Section 4.2.2.

### 4.2.1. Indirect and Direct Solution Approaches

With respect to the former criterion, two non-exhaustive approaches exist [2]. In the first approach, indirect methods first transform the problem into a dual boundary value problem that contains information about the optimality and transversality conditions derived from variational calculus. Although simple problems might allow analytical solution, nearly all practical problems require that the dual problem be discretised next, resulting in a

numerically solvable problem. As a result, *first optimise, then discretise* is a common description of this approach [41, 53, 54].

One disadvantage that is intrinsic to indirect approaches is that the optimality conditions need to be derived for a very complex system of equations. The necessary rederivation of the optimality conditions for each slight problem adaptation, such as added constraints, makes this solution approach unsuited for a general aircraft trajectory optimisation program [57].

Apart from the labour-intensive dualisation of the problem, a major drawback of this method is the required unintuitive guess for non-physical dual, co-state variables. Moreover, the initial guess needs to be better than for direct methods, because of the high sensitivity to the initial guess and the generally much smaller convergence region [2].

Contrarily, direct methods transform the continuous-time equations that describe the optimal control problem directly into a discrete-time problem. In doing so, the infinite-dimensional continuous-time problem is transformed into a large, but sparse NLP problem that can be optimised. Therefore, this approach is aptly and often summarised with *first discretise, then optimise* [41, 53, 54].

One advantage of this method is that it is rather robust to numerical instabilities and bad initial guesses [2]. Unlike indirect methods, direct methods also have the advantage that the order of constrained arcs does not have to be known a priori [2, 41, 58].

### 4.2.2. Shooting and Collocation Methods

The second classification criterion comprises two approaches: shooting and collocation. In shooting methods, only the control-related variables (the adjoints and controls in indirect methods or the controls only in direct methods) are discretised and serve as decision variables in the optimisation routine. The state variables are obtained by integrating the EoMs, thereby automatically satisfying them. An admissible trajectory is found if the vector of decision variables allows integration of the EoMs, while satisfying the boundary or transversality conditions to some tolerance.

In collocation methods, the second approach, both control-related and state variables are discretised and serve as decision variables in the optimisation. With the state variables at the discretised grid's nodes, their values and their derivative values using Equation (4.4) in between nodes are found using an approximation. Collocation methods subsequently enforce that the state equations should be satisfied exactly at some intermediate collocation points by enforcing Equation (4.8); the deficit between the state derivative at the collocation points  $\dot{x}_c$ , obtained by some approximation based on the values of  $\dot{x}$  at the nodes, and the state derivative function  $\ell$ , obtained by evaluating the Equation (4.4) at the collocation points, should be zero [59].

$$\Delta \dot{x}_c^p = \dot{x}_c^p - \ell(x_c^p, u_c^p, t_c) = 0 \quad (4.8)$$

Shooting methods can be further classified according to the number of shooting segments. They are referred to as single-shooting if the entire trajectory is obtained by a single integration, whilst multiple-shooting methods divide the trajectory into several integration intervals [41].

Further subclassification of the collocation methods is based on how the states and controls, in principle only known at the nodes, are approximated at the collocation points. Local collocation methods divide the domain up into smaller segments or finite elements containing a limited number of collocation points, whereas global collocation methods use an approximation of the states and controls over the entire time interval [60].

Finally, collocation methods are further characterised by the type of approximating function that is used. For example, one might approximate the values at the collocation points using piecewise polynomials corresponding to a certain interpolation and a consistent integration scheme. Alternatively, one could choose to approximate the states and controls as a linear combination of some (preferably orthogonal) spectral basis functions. This approach, interchangeably called pseudospectral or orthogonal collocation, has as a final identifier the locations of the collocation points, frequently chosen as the roots of Legendre polynomials, such as Legendre-Gauss (LG), Legendre-Gauss-Radau (LGR), or Legendre-Gauss-Lobatto (LGL). Each of these, in turn, have their advantages and disadvantages in terms of convergence rate and applicability to specific problems [61].

A summary of the rather complex optimal control taxonomy is shown in Figure 4.2. With each branching of optimal control methods, a cross indicates the branch that is found less suitable for this work. The methods' benefits and drawbacks are indicated with plusses and minuses, respectively.

Taking into account the above considerations, it was chosen to solve the trajectory optimisation problem using a LGR pseudospectral direct collocation approach. The main reason for choosing a direct approach is the ease of implementing a problem, without having to provide unintuitive guesses and rederive the optimality conditions

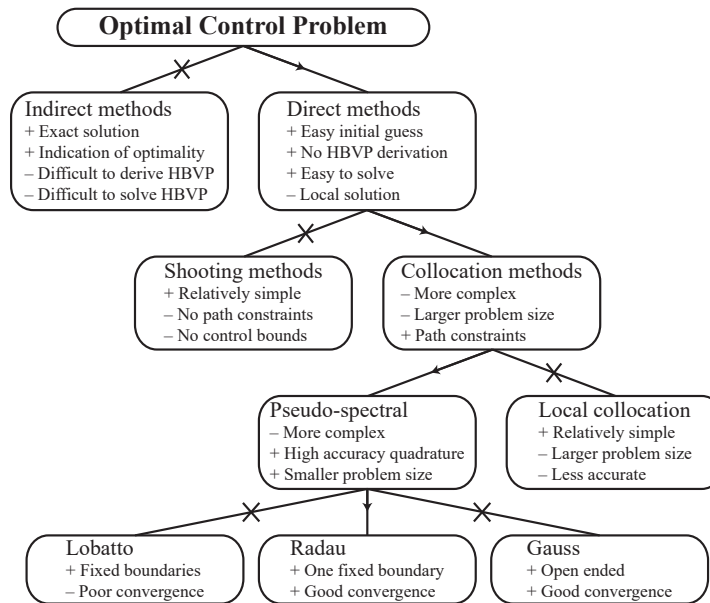


Figure 4.2: The taxonomy of optimal control transcription methods, indicating drawbacks and benefits of each. Image taken from Ref. [57].

for each slight problem adaptation. The main reason for choosing a collocation over a shooting method is the relative robustness of this approach.

### 4.3. Choice of Software

To solve the aforementioned trajectory optimisation problem using a direct collocation method, commercial optimal control transcription software, General Purpose Optimal Control Software II (GPOPS-II), has been used. This software employs an LGR direct pseudospectral (orthogonal) collocation method and serves as an optimal control transcription program with built-in mesh refinement and error quantification [55].

Underneath, the open-source Interior Point Optimizer (IPOPT) is used as NLP optimisation program. Details of this optimiser can be found in Ref. [62].



# 5

## Mission Model and Program Architecture

This chapter serves as an overview of the program that has been written as an aircraft trajectory optimisation tool within PHALANX. Mainly, the tool intends to wrap the optimal control transcription software GPOPS-II, thereby making it more applicable to aircraft trajectory optimisation, specifically. Moreover, the tool provides a scaleable framework in which repetitive tasks, such as setting up phase linkage constraints, are automated. Paradoxically, some mission-related concepts have to be abstracted first, in order to make them usable in software more specialised towards aircraft missions, as is the subject of Section 5.1. Afterwards, Section 5.2 details the execution flow of the program, highlighting some of its features.

### 5.1. Aircraft Mission Modelling

A commercial aircraft mission profile is intrinsically multiphase. This is why the optimal control resolution methods discussed in Chapter 4 are so naturally applicable. The subject of this section is the translation of an intuitive aircraft trajectory model to its multiphase optimal control problem-compatible counterpart. The former is discussed in Section 5.1.1, whereas the latter is the subject of Section 5.1.2. Specific instances of coupled flight phases are given in Section 5.1.3, which are synthesised into a model for the PrP’s design mission in Section 5.1.4.

#### 5.1.1. Aircraft Missions, Constraints, and Capture Conditions

A typical commercial aircraft mission profile can be divided into several flight phases. On the highest level, Ref. [54] distinguishes takeoff, (initial) climb, cruise, approach, and landing and, on a sub-level, each of those phases are in turn broken down to more specific, shorter flight phases.

Ref. [63] adds holding to these broken-down, high-level flight phases, as shown in Figure 5.1. The required holding time capability of an aircraft is typically 15 min at 1500 ft, as specified by European Aviation Safety Agency (EASA) Acceptable Means of Compliance (AMC) 20-6 or Federal Aviation Regulations (FAR) 121.646b. The EASA’s Certification Specifications (CS) and FAR regulations have only minute differences and are henceforth used interchangeably.

In addition to this regular mission definition, critical missions also include diversion to another airport in their specifications. The diversion range is somewhat more arbitrary, because it depends on the aircraft’s Extended-range, Twin-engine Operational Performance Standards (ETOPS) rating and the nearest alternative airport. For example, Ref. [64] accounts for a 370 km diversion, whereas Ref. [35] accounts for 200 km and 500 km diversions.

In practice, the flight envelope of the aircraft is bounded by physical considerations. Firstly, the aircraft is not allowed to fly within a specified tolerance of its (reference) stall speed, according to CS25.103. Practically, this limit will not be sought by any trajectory optimisation algorithm, because of the high drag penalty in this flight regime.

The second flight envelope limitation is caused by the aircraft’s buffet onset boundary. Specified as specific combinations of  $C_L$  and  $M$ , crossing the boundary causes structural vibrations, both at high and low speeds. At high speeds, buffet is caused by shock-induced separation and unsteady flow, causing airframe vibrations. At low to moderate speeds, buffet typically precedes stall. Due to the limitations of the 3DPM used for generating the aerodynamic data, this effect is not modelled, however.

To simulate commercial aircraft procedures realistically, an approach will be adopted in which all flight phases are defined by variables that are kept constant, called flight objectives, and flight phase termination conditions,

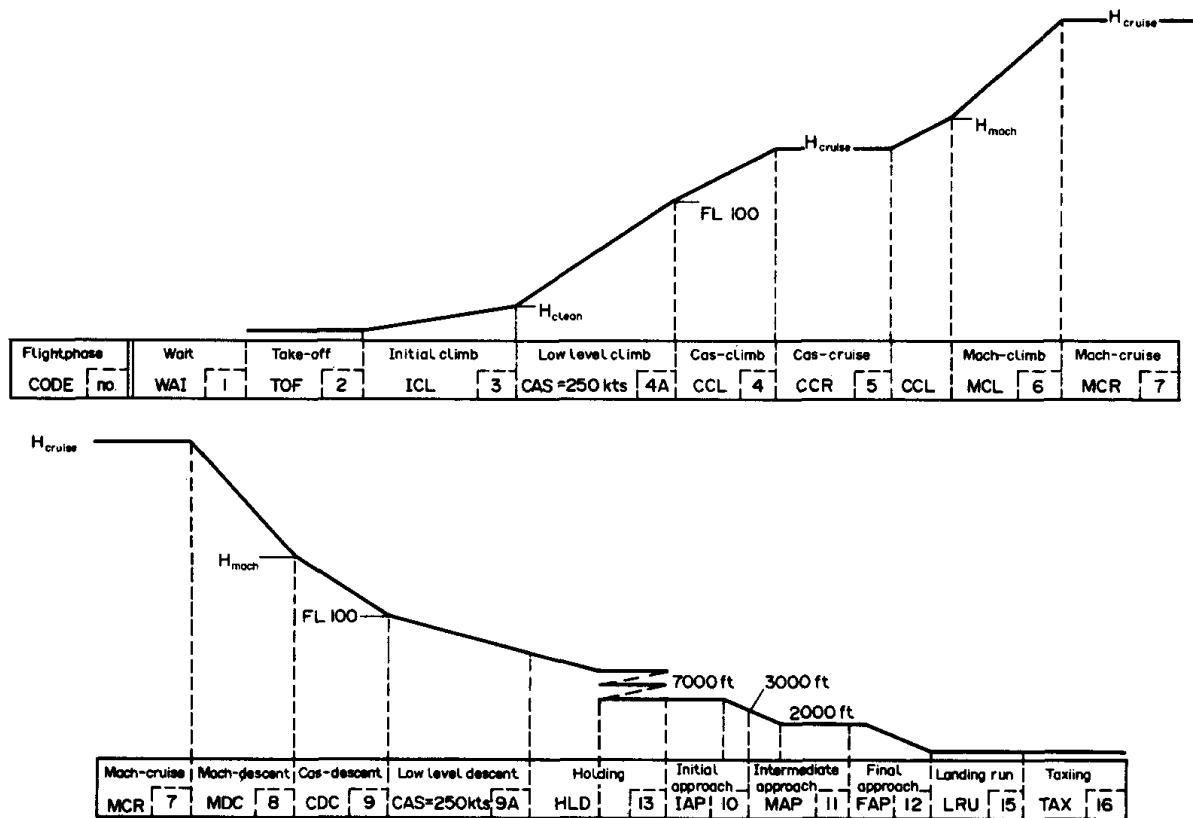


Figure 5.1: A typical commercial aircraft mission profile including hold, without diversion. Image taken from Ref. [63].

called capture conditions [39]. The former model pilot procedures to some extent, whereas the latter ensure mission convergence through proper linkage of flight phases; if a capture variable reaches a specified threshold, the capture condition is satisfied and the next phase is initiated. Obviously, the fulfilment of a capture condition and consequent adequate linkage of neighbouring phases is guaranteed when the capture variable behaves monotonically, i.e. either only increases or decreases in value [39].

Although imposing capture conditions and prescribing flight objectives is necessary for mission convergence in time-stepping aircraft trajectory simulations, this is not strictly the case for integral-mission optimal control approaches. Nonetheless, the concepts of capture conditions and flight objectives are an intuitive and realistic representation of real-life operations and are thus adopted in the program, using them wherever applicable.

### 5.1.2. Mission Class System

To abstract the aircraft mission definition to allow for program scalability and user-friendliness, an OOP approach was taken in modelling the mission and its flight phases. This means that the properties of each have been generalised and pre-programmed into a class or template. These two classes, called `flightPhase` and `mission`, are shown in Figure 5.2. The diamond-headed arrow indicates that a `mission` is composed of one or more `flightPhases`, whereas a `flightPhase` only belongs to one `mission`.

Each class contains an upper and lower segment describing the contents of that class. An incomplete list of the generalised properties, or attributes, of these classes are displayed in their respective upper segments. The functions associated with these classes, called methods, are shown in the respective lower segments. The careful observer may have noticed that `missions` and `flightPhases` have some equal attributes. This has been done to make it easy for the user to set defaults or, for example, mission-level constraints, valid for all `flightPhases`.

Some other noteworthy attributes are the `eom...` attributes, which serve as switches to use a specific set of EoMs or `dynamicConstraints`, such as 2D or 3D EoMs, or flight or ground dynamics EoMs. Moreover, the objective function can either be set on `flightPhase`-level, or on `mission`-level, the desired objective function is a function of variables in multiple phases, such as Equation (4.3).

The functions of the `setFlightObjective` and `setCaptureCondition` methods are to transform the aforementioned capture conditions and flight objectives into optimal control-compatible `pathConstraints`

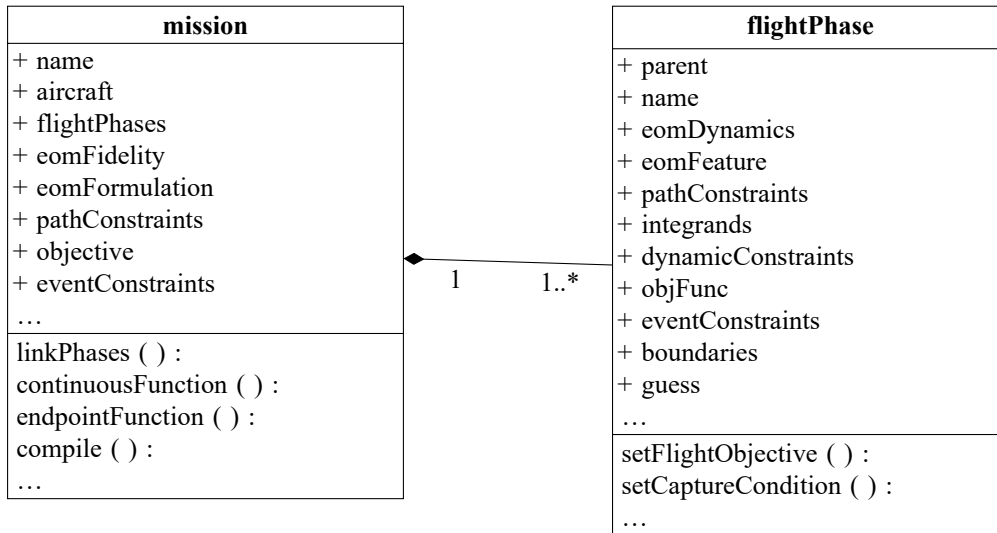


Figure 5.2: A UML class diagram of the mission and flightPhase objects.

and eventConstraints. To this end, flight objectives are simply transformed into path equality constraints. Capture conditions are expressed as a combination of path and event constraints.

For example, a capture condition stating that the phase ends upon having accelerated to a Calibrated Airspeed (CAS) =  $C$  can be expressed as a pathConstraint,  $\mathcal{E}_{\text{path}} = \text{CAS} < C$ , and an eventConstraint,  $\mathcal{E}_{\text{event}} = \text{CAS}_f = C$ . The former guarantees the capture variable doesn't reach the threshold somewhere halfway through the phase, whereas the latter ensures the capture condition is satisfied at the phase end. Inversely, a “decelerate-to-CAS” capture condition would result in a pathConstraint  $\mathcal{E}_{\text{path}} = \text{CAS} > C$ .

The methods of the mission class are mainly intended to tie all flightPhases together. For one thing, linkPhases sets the phase linkage constraints as an instance of eventConstraints, Equation (4.6). For another thing, continuousFunction evaluates all flightPhases' pathConstraints, integrands, and dynamicConstraints and the endpointFunction method evaluates all eventConstraints and objFuncs. Finally, the compile function transforms the class system to a GPOPS-II-compatible input.

### 5.1.3. Flight Phase Stereotypes

To ease defining a mission profile and prevent repetitive work and most of all the labour-intensive debugging upon each new mission definition, functions have been written to define frequently occurring parts of the mission, based on only few top-level parameters. These coupled flightPhases are called “stereotypes” within the tool and correspond to the high-level flight phases mentioned at the beginning of Section 5.1.1. Their specific implementations and underlying assumptions are discussed next.

#### Takeoff

The takeoff stereotype is assumed to consist of three flight phases. The first flight phase is the level ground roll of the aircraft, accelerating from zero to its rotation velocity. During this phase, the states and controls are constrained; no pitching is possible, i.e.  $q = 0$ , the aircraft should follow the runway slope, i.e.  $\gamma = \gamma_{\text{runway}}$ , and in 3D the aircraft should follow the runway heading and have its wings level with the possibly banked runway, i.e.  $\chi = \chi_{\text{runway}}$  and  $\mu = \mu_{\text{runway}}$ . The capture condition of this phase is  $V = V_{\text{rot}}$ .

In the second phase, the aircraft is assumed to have built up enough dynamic pressure to pitch up the aircraft, but the aircraft is still on the runway. This means that except for the constraint  $q = 0$  all the previous constraints still hold. The capture condition for this phase is the condition that the ground reaction forces on the wheels are nil for the first time, i.e.  $N = 0$ . During both ground phases, the rolling friction coefficient is assumed to be constant at 0.02, based on Ref. [65].

The third and final takeoff phase is the airborne phase, in which the aircraft lifts off of the runway and climbs out to a specified clearance or screen height, compliant with CS 25.113. This means the aircraft uses the flight dynamics EoMs for the first time, in which the reaction forces are left out. Moreover, the aircraft is no longer constrained to follow the runway slope or have its wings level with the runway. It is, however, assumed that the runway's heading has to be maintained. The capture condition of this phase is reaching the screen height,  $h_{\text{screen}}$ .

Summarising, the takeoff phase top-level inputs are  $V_{\text{rot}}$ ,  $h_{\text{screen}}$ ,  $\gamma_{\text{runway}}$ ,  $\chi_{\text{runway}}$ , and  $\mu_{\text{runway}}$ .

## Climb and Descent

The climb and descent phases are very similar in their structure and are therefore treated in the same section. First, the climb stereotype is discussed and later, the similarities in defining the descent stereotype are discussed. Based on Ref. [66], the climb stereotype is modelled as four coupled flight phases.

The first flight phase is characterised by the regulatory speed constraint imposed by FAR 91.117a. In this regulation, it is specified that aircraft cannot exceed an Indicated Airspeed (IAS) of 250 kts or  $129 \text{ m s}^{-1}$  below altitudes of 10 000 ft. Due to the unavailability of the IAS, the CAS is usually taken, because it is most similar. This directly explains segments 4a and 9a in Figure 5.1, in which a constant CAS of 250 kts below Flight Level (FL) 100 is imposed, which corresponds to an altitude of 10 000 ft. The capture condition for this phase is reaching an altitude of  $h = 10\,000 \text{ ft}$  or  $3048 \text{ m}$ .

The second flight phase in the climb stereotype is modelled as a level acceleration until a CAS, thereby giving away the capture condition for this phase. Moreover, level flight is maintained, such that a flight objective  $\dot{\gamma} = 0$  is imposed.

In the third flight phase, the aircraft maintains a constant CAS, its new flight objective. Because of the dependence of CAS on dynamic pressure along with the International Standard Atmosphere (ISA) decreasing air density with altitude, the constant-CAS climb results in an accelerated climb. The aircraft maintains this CAS until it reaches a certain  $M$ , which is the capture condition for this phase.

Because of operational limits, such as the Maximum Operative (MO) Mach number, for example, a climbing aircraft maintaining constant CAS may at some point encounter its  $M_{\text{MO}}$ . The corresponding altitude and velocity are usually called the crossover altitude and velocity [37]. In practice, the aircraft will not accelerate up to its  $M_{\text{MO}}$ , but to some other optimal crossover  $M$  [67, 68]. The same transition between constant-CAS and -Mach climb is shown in Figure 5.1, depicted as CCL and MCL, respectively.

In the fourth and final flight phase, the aircraft has as flight objective to maintain a constant  $M$ . Contrary to the CAS, maintaining a constant  $M$  implies a decelerating climb, because the speed of sound decreases with increasing altitude. The capture condition for this phase is to reach the initial cruise altitude, i.e.  $h = h_{\text{cr,i}}$ .

The beauty of applying optimal control is that the constant flight objective values of  $M$  and CAS don't have to be known explicitly. Contrary to time-stepping simulations, one can impose the constraints that their time derivatives must be zero and let the solver find optimum climb CAS and  $M$  values.

The similarity of the descent stereotype lies in that all component flight phases are essentially the same, except that their order is reversed. The first phase is thus defined as a constant- $M$  descent from some initial altitude. At the crossover altitude, the second, constant-CAS descent phase starts. At 10 000 ft, the aircraft decelerates to CAS = 250 kts in the third phase. Finally, the aircraft further descends to some target altitude, while respecting the speed limit of CAS = 250 kts. Both stereotypes are thus characterised by the following top-level inputs: the flight objectives CAS and  $M$  and their target final altitudes.

## Cruise

Aviation authorities have imposed restrictions on altitudes at which an aircraft can fly for a prolonged period of time, to keep Air Traffic Control (ATC) manageable and to promote collision avoidance. Specifically, aircraft are restricted to flying at odd FLs (010, 030, 050, etc.) when flying eastward, while they are restricted to even FLs flying westward [69]. These discrete FLs are not modelled, because it would require Mixed-integer Nonlinear Programming (MINLP), which is deemed out of the scope of this work. Instead, level cruise flight at arbitrary FLs is imposed.

Airlines typically want their aircraft to climb to higher altitudes as the aircraft burn fuel for fuel economy. Because of the aforementioned restriction, however, gradual climbing is prohibited. To strike a happy medium, aircraft typically perform a step climb between level cruise legs, to gain in fuel economy while respecting the level flight requirements. The cruise stereotype is therefore modelled as level flight segments, connected by step climbs, while constraining the  $M$  to not exceed the  $M_{\text{MO}}$  in compliance with CS 25.1505. The top-level input for this stereotype is the number of allowed climb legs.

## Landing

The landing stereotype is modelled according to the Federal Aviation Administration (FAA)'s airplane flying handbook, excluding ground roll.<sup>3</sup> The ground roll is excluded, because limited data are available to model the

<sup>3</sup>URL [https://www.faa.gov/regulations\\_policies/handbooks\\_manuals/aviation/airplane\\_handbook/media/10\\_afh\\_ch8.pdf](https://www.faa.gov/regulations_policies/handbooks_manuals/aviation/airplane_handbook/media/10_afh_ch8.pdf) [Accessed on 15 March, 2020]

braking of the aircraft, either with mechanical or air brakes. Moreover, a detailed study into modelling these aspects is deemed out of the scope of this work. As a result, the landing stereotype has three flight phases in total.

The first flight phase of the stereotype is the base leg, in which the aircraft lines up and gets into position for final approach. This phase does not have a specific capture condition or flight objective, other than connecting the landing stereotype to any preceding phases. In case a descent stereotype is connected to a landing stereotype, the base leg is best left out, because the fourth phase in the descent stereotype can perform the base leg's function of lining up for final approach.

The Final Approach Point (FAP) marks the start of this phase, described in the FAA's handbook as a constant-descent angle approach, in which the pilot controls the angle of descent by varying engine power and pitch angle. Typically, the approach angle is taken as  $3^\circ$  [29], but in a more general formulation, the flight objective is set as  $\dot{\gamma} = 0$  in this second flight phase to leave room for optimisation. Alternatively, the user can always provide a specific approach angle.

The third and final landing stereotype flight phase is the flare or round-out, in which the aircraft prepares for touch-down by making the aircraft fly sufficiently parallel to the runway. In this flight phase, the flare manoeuvre is modelled with a capture condition for which the aircraft reaches the runway altitude, typically  $h_f = 0$ , while the flight path angle matches the runway slope at landing, i.e.  $\gamma = \gamma_{\text{runway}}$ . In reality, too soft landing is undesirable, because it may cause severe landing gear oscillations known as shimmy.<sup>4</sup> Modelling these effects is however out of the scope of this work.

Summarising, the landing stereotype is built on the inputs  $h_{FAP}$ ,  $h_{\text{flare}}$ ,  $h_f$ ,  $\gamma_{\text{runway}}$ ,  $\chi_{\text{runway}}$ , and  $\mu_{\text{runway}}$ .

## Holding

The final stereotype is holding, also known as loiter, and it is modelled according to the FAA's regulatory description of loiter, AIP ENR 1.5. The constraints, such as speed and leg duration constraints, will not be repeated here to promote readability. In a standard holding pattern, the aircraft flies a race track pattern (see Figure 5.3) for a specified time, for example to await landing clearance. One race track "lap" consists of four flight phases: a fix-end turn, an outbound leg, an outbound-end turn, and an inbound leg. To simplify entry procedures, it will be assumed that the aircraft always enters and exits at the holding fix, thereby making the outbound leg not actually the exit direction.

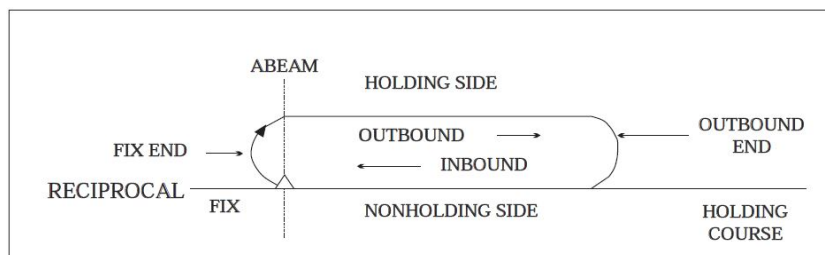


Figure 5.3: Descriptive terms of the holding pattern. Image taken from AIP ENR 1.5.<sup>5</sup>

The first flight phase starts whenever the aircraft reaches a specified holding fix at a pre-specified, inbound heading. Immediately, the aircraft will bank right to turn to reach a point lying somewhere on the "ABEAM". Note that the turn radius is thus not constrained, but its final position's orientation with respect to the fix is. Each turn is constrained by a maximum duration of 60 s or 90 s, depending on altitude.

In the second flight phase, upon leaving the turn, the aircraft flies the outbound leg, which is again constrained to a maximum duration. Moreover, the duration of both legs should be adjusted to meet the overall holding time required.

In the third flight phase at the outbound end, the aircraft turns again, turning to the point that will allow the aircraft to fly a straight leg up to the holding fix

In the fourth, inbound flight phase, the aircraft flies a straight leg up to the holding fix. The four flight phases are repeated  $n$  times, appropriate to satisfy the total holding time.

Because of the maximum allowed durations of the straight legs and turns, the pilot will have to adjust the duration of the straight legs to match the total holding time. This task is also performed upon specification of

<sup>4</sup>URL [http://www.boeing.com/commercial/aeromagazine/articles/2013\\_q3/pdf/AERO\\_2013q3.pdf](http://www.boeing.com/commercial/aeromagazine/articles/2013_q3/pdf/AERO_2013q3.pdf) [Accessed on 1 May, 2020]

<sup>5</sup>URL [https://www.faa.gov/air\\_traffic/publications/atpubs/aip\\_html/part2\\_enr\\_section\\_1.5.html](https://www.faa.gov/air_traffic/publications/atpubs/aip_html/part2_enr_section_1.5.html) [Accessed on 7 February, 2020]

the holding stereotype. Summarising, the holding stereotype can be constructed by inputting the holding fix coordinates  $(x, y)_{\text{hold}}$ , inbound heading  $\chi_{\text{inbound}}$ , holding altitude  $h_{\text{hold}}$ , holding time  $t_{\text{hold}}$ , and the number of laps flown  $n_{\text{laps}}$ .

#### 5.1.4. PrandtlPlane Design Mission

Using the definition of the stereotypes discussed previously, the PrP's mission is defined relatively easily. This design mission definition is shown in Table 5.1, in which the shading indicates the stereotype grouping of individual flight phases. The final approach altitude of 610 m is based on Ref. [6] and the flare altitude of 15 m on Ref. [65]. Moreover, it is assumed that the MO Mach number of the PrP is equal to its design cruise Mach number. As a final note, the design mission is flown in 2D.

Table 5.1: The PrandtlPlane's design mission, with the active flight objectives, capture conditions, and path constraints per phase.

Phase	Description	Flight objective	Capture condition	$\mathcal{E}_{\text{path}}$	$\mathcal{E}_{\text{event}}$
1	Takeoff: level ground roll	$q = 0 \text{ rad s}^{-1}$	$V_{\text{rot}} = 50 \text{ m s}^{-1}$	—	—
2	Takeoff: pitched ground roll	—	$N = 0 \text{ N}$	—	—
3	Takeoff: initial climbout	—	$h = 50 \text{ m}$	—	—
4	Limited-CAS climb	—	$h = 3048 \text{ m}$	$\text{CAS} < 129 \text{ ms}^{-1}$	—
5	Level acceleration	$\gamma = 0 \text{ rad}$	$\text{CAS} = C$	—	—
6	Accelerate-climb	$\text{CAS} = 0 \text{ m s}^{-2}$	$M = C$	—	—
7	Decelerate-climb	$\dot{M} = 0 \text{ s}^{-1}$	$h = 11 \text{ km}$	$M < M_{\text{MO}} = 0.79$	—
8	Cruise: level flight leg 1	$\gamma = 0 \text{ rad}$	—	$M < M_{\text{MO}} = 0.79$	—
9	Cruise: step climb	—	—	$M < M_{\text{MO}} = 0.79$	—
10	Cruise: level flight leg 2	$\gamma = 0 \text{ rad}$	—	$M < M_{\text{MO}} = 0.79$	—
11	Accelerate-descend	$\dot{M} = 0 \text{ s}^{-1}$	$\text{CAS} = C$	$M < M_{\text{MO}} = 0.79$	—
12	Decelerate-descend	$\text{CAS} = 0 \text{ m s}^{-2}$	$h = 3048 \text{ m}$	—	—
13	Level deceleration	$\gamma = 0 \text{ rad}$	$\text{CAS} = 129 \text{ m s}^{-1}$	—	—
14	Limited-CAS descent	—	$h = 610 \text{ m}$	$\text{CAS} < 129 \text{ ms}^{-1}$	—
15	Landing: final approach	$\dot{\gamma} = 0 \text{ rad s}^{-1}$	$h = 15 \text{ m}$	—	—
16	Landing: flare / round out	—	$h = 0 \text{ m}$	—	$\gamma = 0 \text{ rad}$

From the discussion in Section 4.1.2, it is evident that the mission definition has to be complemented by appropriate bounding of the state and controls. These bounds are indicated in Table 5.2.

Table 5.2: The boundaries imposed on the state and control variables in the design mission.

Variable	Lower bound	Upper bound
$h$	0 m	14 000 m
$m$	ZFM	MTOM
$V$	$0 \text{ ms}^{-1}$	$330 \text{ ms}^{-1}$
$x$	0 m	4000 km
$\gamma$	$-25^\circ$	$25^\circ$
$\alpha$	$-6^\circ$	$9^\circ$
$q$	$-5^\circ \text{ s}^{-1}$	$5^\circ \text{ s}^{-1}$
$\tau$	0	1

Moreover, terminal boundary conditions are imposed on the aircraft states and controls. One terminal boundary condition is imposed to ensure that the overall distance flown at the end of the mission equals the required mission range. This allows for easy adaptation of the mission range, simply by changing this boundary condition. In the same way, another terminal boundary condition ensures that the aircraft arrives at its destination at its ZFM, having thus burnt all its fuel upon landing. The initial takeoff mass of the aircraft is then determined accordingly by the solver.

## 5.2. Program Flow

It is the aim of this section to give a concise overview of the execution flow of the program. A schematic overview is shown in Figure 5.4. This Unified Modelling Language (UML) activity diagram shows which parts of the program are wrapped by which piece of software, GPOPS-II, IPOPT, or by the PHALANX module if not enclosed in any dotted-line box.

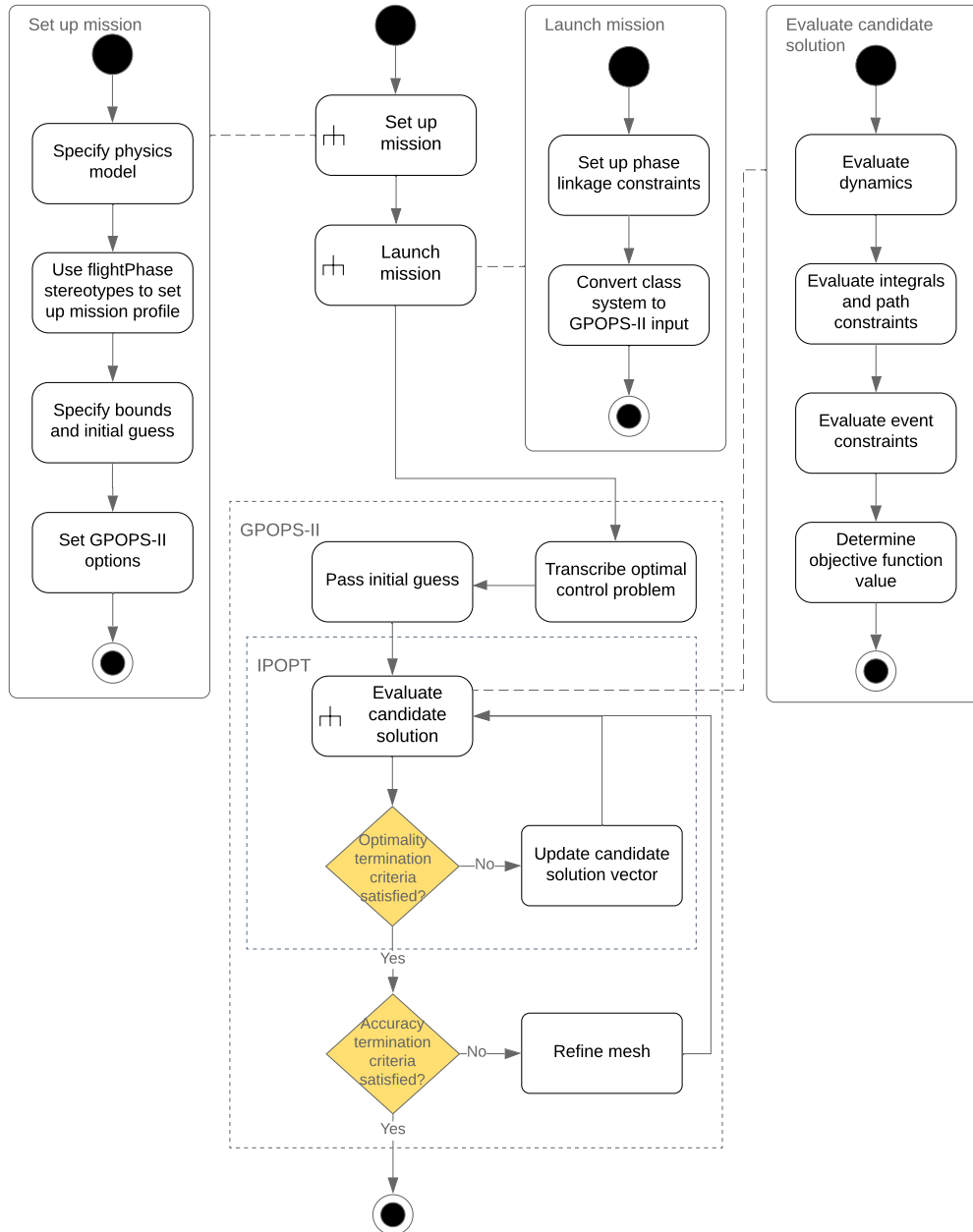


Figure 5.4: A UML activity diagram of the trajectory optimisation program.

First, the user of the program needs to define the mission, for example using the elaborately discussed stereotypes. In doing so, a physics model must be selected, thereby specifying, amongst others, 2D or 3D flight, the inclusion of the aerodynamic coefficients due to the rotational velocities of the aircraft, and possibly the inclusion of unconventional flight controls.

Upon mission launch, the program automatically links the individual phases by imposing linkage constraints. These linkage constraints ensure the continuity of state variables. Moreover, periodic variables such as the heading

angle are linked by transforming their interface deficit functions to sinusoidal functions with period  $2\pi$ , to obtain the required  $C^2$  smoothness. This smooth behaviour is not obtained using the `mod` function native to MATLAB<sup>®</sup> and using this function will trouble convergence. Unfortunately, GPOPS-II doesn't allow setting event constraints as a function of control variables, such that the continuity of the controls cannot be guaranteed.

Next, having received the compatible input structure, GPOPS-II transcribes the problem to a numerical LGR discrete collocation problem. This piece of software now acts as a coordinator between IPOPT and the actual dynamics evaluation functions that are within PHALANX. Passing the current objective function value, the value of all constraints, and the dynamics evaluation to IPOPT, IPOPT subsequently tries to find the objective-minimizing solution vector that satisfies the given constraints.

If IPOPT has reached its termination criteria, GPOPS-II evaluates the obtained solution in terms of numerical accuracy of the EoMs. If this, in turn, is sufficient to satisfy the user-specified tolerances, GPOPS-II terminates and outputs the solution.

# 6

## Verification and Validation

The goal of this section is to present the efforts that have been made to check the validity of the trajectory optimisation model. Due to the unavailability of real-life trajectory data, validation is performed with respect to the solution of a multiphase trajectory optimisation problem found in scientific literature, Ref. [45].

In Section 6.1, the setups of the reference research and of the current study, adapted to allow fair comparison between the two, are discussed. Then in Section 6.2, the resulting optimal trajectories of both setups and the original results presented in the reference paper are discussed, highlighting their differences and explaining those based on the model differences.

### 6.1. Problem Setup

Because the reference study and the current study differ in several respects, the validation has been split into two steps. Replicating the problem setup as well as possible, based on Ref. [45], the resulting trajectory (hereafter referred to as *replicate*) is compared with the results presented in Ref. [45] (hereafter referred to as *reference*) to bring to light the solutions' differences due to their respective optimal control approaches. Replacing the reference EoMs with a simplified form of Equations (3.3), the resulting trajectory (hereafter referred to as *adapted*) can be compared to the reference and replicate trajectories to observe the consequences of adopting new EoMs.

#### 6.1.1. Reference Study Setup

The reference study used for validation is a case study of an A320 flying from Madrid-Barajas to Berlin-Schönefeld airport. The aircraft departs from Madrid, following the Standard Instrument Departure (SID) shown in Figure 6.1. Further details, such as the imposed flight profile, can be found in Ref. [45]. Some of the main characteristics of the model will be repeated here for enhanced readability.

Equations (6.1) describe the 3-DoF coordinated flight dynamics of a point mass aircraft over a spherical Earth. The model assumes that the thrust vector is always aligned with the velocity vector. Note that the EoMs have been adapted slightly, because Ref. [45] uses a different sign convention; whereas the current study takes the heading positive clockwise from true North and the aerodynamic roll angle positive for a right-wing drop, the original EoMs in Ref. [45] imply that  $\chi$  is positive counter-clockwise from the East and that  $\mu$  is positive for a left-wing drop. Equations (6.1) have been adapted to conform to the current study's nomenclature and sign convention.

$$\dot{x} = \begin{bmatrix} \dot{h} \\ \dot{m} \\ \dot{V} \\ \dot{\Lambda} \\ \dot{\Theta} \\ \dot{\gamma} \\ \dot{\chi} \end{bmatrix} = \begin{bmatrix} V \sin \gamma \\ -T \cdot \text{TSFC} \\ \frac{1}{m} \{T - D_{ac}\} - g \sin \gamma \\ \frac{1}{(R_E+h) \cos \Theta} \{V \cos \gamma \sin \chi\} \\ \frac{1}{R_E+h} V \cos \gamma \cos \chi \\ \frac{1}{mV} \{L \cos \mu - mg \cos \gamma\} \\ \frac{1}{mV \cos \gamma} L \sin \mu \end{bmatrix} \quad (6.1)$$

The aerodynamic and propulsive aircraft models used in Ref. [45] are taken from EUROCONTROL's BADA family 3 [8]. This means that a classic parabolic aerodynamic drag polar  $C_D = C_{D_0} + kC_L^2$  is assumed, where



$r$  sufficiently.

Secondly, an additional relation describing the mapping from the angle of attack to the lift coefficient  $C_L(\alpha)$  is necessary. Because the angle of attack recurs in the equations describing the longitudinal and vertical accelerations,  $\dot{V}$  and  $\dot{\gamma}$  respectively, the mapping has to be fairly realistic. Because this relation is not provided by BADA, the mapping  $C_L(\alpha)$  found from VSAERO CFD analyses of the A320-like CSR-01 aircraft was used [30]. The bounds on  $\alpha$  were chosen in such a way that the maximum and minimum allowed  $C_L$  stated in the reference paper are respected. That is, the constraints  $C_{L\min} < C_L < C_{L\max}$  are replaced with  $\alpha_{\min} < \alpha < \alpha_{\max}$ .

Another feature that must be accounted for in recreating the Madrid-Berlin mission is the use of high-lift devices. The reference study models this in compliance with the BADA aerodynamic model: deployment of high-lift devices results in a new aircraft configuration and in corresponding new values for  $C_{D_0}$  and  $k$ . In the case of the adapted problem setup, the additional lift associated with flying in a new configuration should be modelled differently. One cannot simply change the values of the coefficients  $C_{D_0}$  and  $k$ , because this would disregard the increase in lift at a given angle of attack. Therefore, the lift coefficient increments corresponding to each configuration are taken as the increase in  $C_{L\max}$  with respect to the clean configuration. As such, the upward shift of the lift curve  $C_L(\alpha)$  is accounted for, whereas its generic leftward shift isn't [38].

The setups' distinct kinematic representations of the aircraft's inertial reference system is the final difference that must be recognised. Namely, the waypoint and initial and final positions of the aircraft are stated using a latitude-longitude, spherical representation in the reference setup, whereas the adapted setup employs an eastward and northward distance, flat-Earth frame of reference. Mapping the geodetic coordinates  $\Theta$  and  $\Lambda$  to  $x$  and  $y$  coordinates using Equations (6.2), an ambiguity is introduced: as  $\Theta \rightarrow 90^\circ$ ,  $x \rightarrow 0$ , no matter the actual distance travelled East. This is an inevitable consequence of Earth's meridians converging near the poles.

$$\begin{aligned} x &= R_E (\Lambda - \Lambda_i) \cos \Theta \\ y &= R_E (\Theta - \Theta_i) \end{aligned} \quad (6.2)$$

## 6.2. Comparison of Trajectories

The ground tracks of the three mission setups are shown in a Mercator-projected map in Figure 6.2. The ground tracks of the reference and replicate trajectories are strikingly similar, but do not overlap exactly. Moreover, during the cruise portion of the flight, the adapted trajectory is slightly less curved than the other two trajectories.

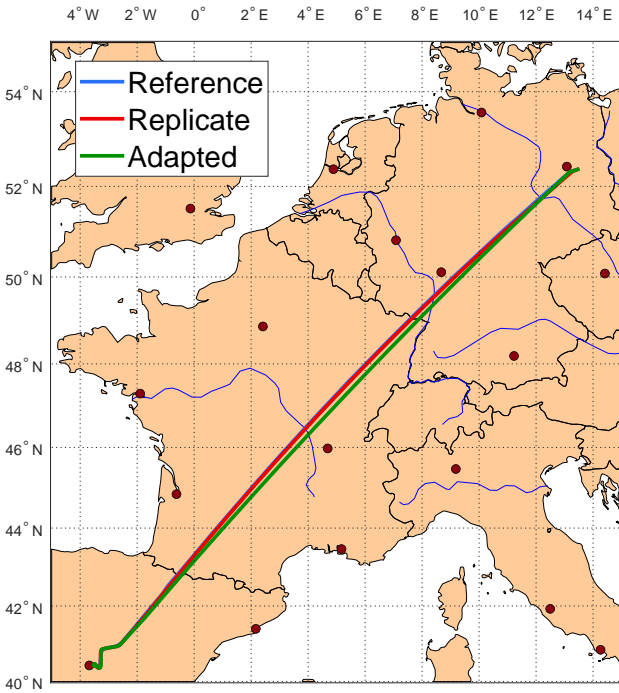


Figure 6.2: The reference, replicate, and adapted trajectories' ground tracks, mapped using a Mercator projection.

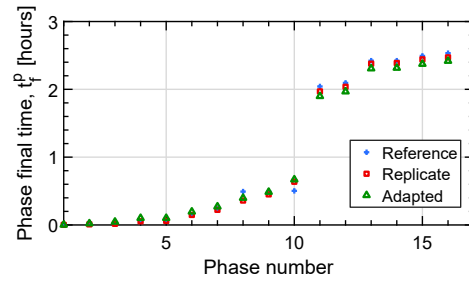


Figure 6.3: The phase switching or end times for each of the mission setups.

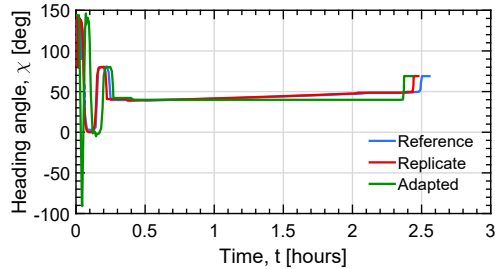


Figure 6.4: The reference, replicate, and adapted trajectories' heading angle time histories.

In fact, upon closer inspection of the time histories of the heading angle  $\chi$  in Figure 6.4, it can be seen that in actuality, the aircraft maintains a constant heading in the adapted trajectory. That is, its trajectory is not curved at all in the cruise phase, of which the initial and final times are easily distinguished in Figure 6.3 by the large time interval. Thinking back to the EoMs underlying the adapted trajectory, the fact that the aircraft travels from Madrid to Berlin in a straight line is a logical consequence of the flat-Earth assumption. Contrarily, the slight change in heading angle that is observed for the reference and replicate trajectories is an immediate consequence of their travelling a spherical surface. The adapted trajectory's curvature observed in Figure 6.2 must thus be fully attributed to Mercator projection distortion.

Another consequence of this difference in spherical and flat Earth frames of reference is that the trajectory flown is shorter for the adapted mission. Because the adapted trajectory goes from Madrid to Berlin in a straight line instead of a geodesic line, the distance travelled and the consequent mission duration is shorter. This effect is visible in the time signals' length differences in Figure 6.4, but also in all subsequent signals, such as Figures 6.5 and 6.6.

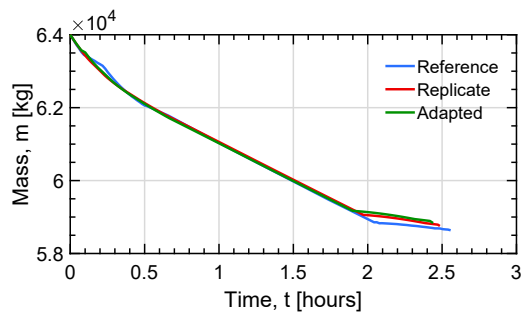


Figure 6.5: The reference, replicate, and adapted trajectories' aircraft mass time histories.

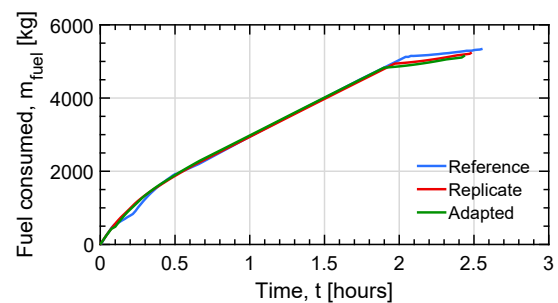


Figure 6.6: The reference, replicate, and adapted trajectories' fuel consumption time histories.

Figures 6.5 and 6.6, depicting the fuel consumption and the resulting mass time histories of the aircraft, show that the adapted trajectory gains in fuel economy because of its shortened trajectory. Nevertheless, it is seen that even the replicate trajectory gains in fuel economy with respect to the reference results, even though these two are expected to coincide due to their equivalent mission setups.

Figure 6.7 shows that the altitude profiles obtained for the replicate and adapted trajectories deviate quite a lot from the reference trajectory. Whereas the latter is somewhat hesitant in climbing, the former two trajectories indicate that the aircraft saves fuel partly by climbing to higher altitudes earlier, both during the SID and cruise.

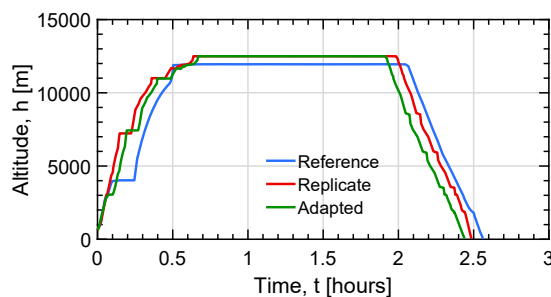


Figure 6.7: The reference, replicate, and adapted trajectories' altitude time histories.

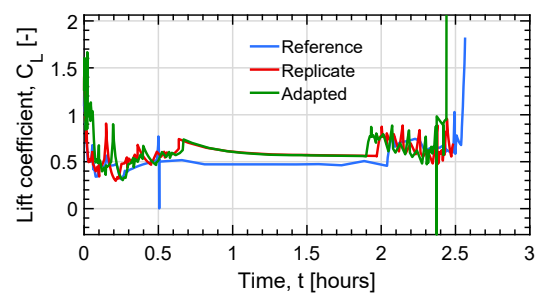


Figure 6.8: The reference, replicate, and adapted trajectories' lift coefficient time histories.

Because of the replicate and adapted trajectories' higher-altitude cruise flight, the aircraft flies at a higher lift coefficient (see Figure 6.8) at approximately the same velocity (see Figure 6.9) with respect to the reference trajectory. Limited by the BADA operational model's imposition of a  $M_{MO} = 0.82$ , the maximum velocity for a given altitude is fixed and in all three trajectories the aircraft seeks this limit.

In any case, the fact that the replicate and adapted trajectories exhibit lift coefficient, velocity, and thrust profiles much distinct from the reference trajectory can only be seen as a logical consequence of the chosen alternative altitude profile.

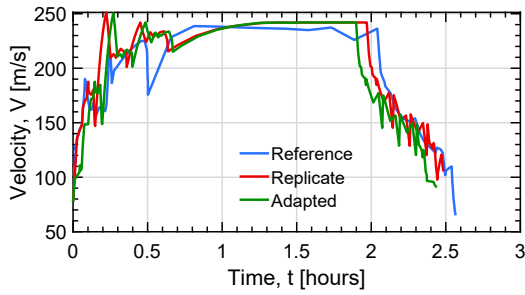


Figure 6.9: The reference, replicate, and adapted trajectories' velocity time histories.

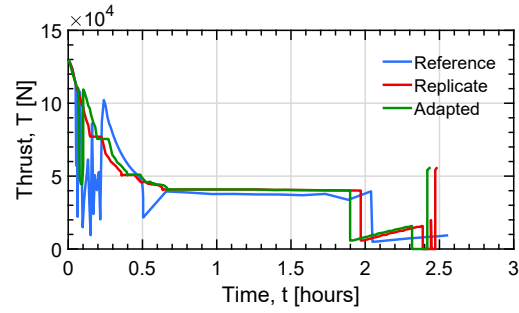


Figure 6.10: The reference, replicate, and adapted trajectories' thrust time histories.

It is hard to draw definitive conclusions on the agreement of the rather high-frequency time signals shown in Figures 6.8, 6.11 and 6.12, because of the cropping of high-gradient regions in the graph. Moreover, the reference trajectory data was read off of graphs, making it hard to distill the reference data points from these highly oscillatory regions in the trajectory.

Nonetheless, the replicate and adapted trajectories show very good agreement in nearly all variables' time histories. Having discussed the root cause of the time lag between the two being the different kinematic models underlying the two setups, the trends of the two are generally identical. As such, it can be concluded that the assumption that the thrust vector is always aligned with the velocity vector that underlies the EoMs of the replicate setup is of little to no impact on the final outcome.

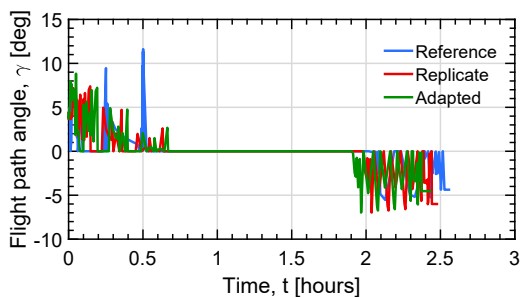


Figure 6.11: The reference, replicate, and adapted trajectories' flight path angle time histories.

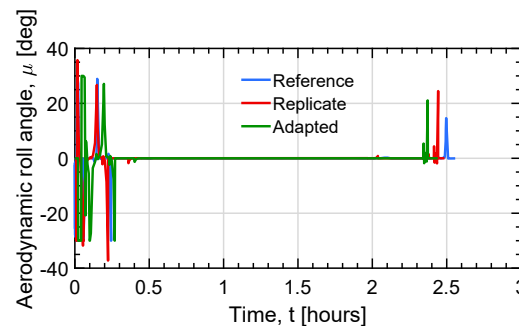


Figure 6.12: The reference, replicate, and adapted trajectories' aerodynamic roll angle time histories.

Unfortunately, a quantification of the agreement of the trajectories at the collocation points is not possible, because of the setups' different time instances at which the variables' signals are sampled. Moreover, the time lag between the trajectories' trends would impede a meaningful interpretation of numerical error quantification of those sample points anyway. Instead, a numerical comparison of the top-level performance metrics is presented in Table 6.1. It is seen that these metrics agree reasonably well.

Table 6.1: Comparison of optimal top-level performance metrics of the validation mission setups.

Mission setup	Duration [h:mm:ss]	Error w.r.t. reference	Fuel consumed	Error w.r.t. reference
Reference	2:33:26	Not applicable	5344 kg	Not applicable
Replicate	2:29:05	-2.83 %	5246 kg	-1.84 %
Adapted	2:26:21	-4.26 %	5165 kg	-3.36 %



# Mission Performance

In this chapter, the performance of the PrP and of the CSR-01 is elaborately discussed and compared, based on multiple case studies. First, Section 7.1 deals with presenting the design mission optimal trajectories of both aircraft for several CIs. Then, a maximum-range mission is simulated in Section 7.2, to analyse the aircraft's off-design, harmonic mission performances. In Section 7.3, a zoomed-out overview of the performance of both aircraft in terms of top-level performance metrics is given.

## 7.1. Design Mission Performance

With the mission setup as presented in Section 5.1.4, a flexible framework is available in which multiple missions can easily be run. This allows for comparison of missions with only few changed controlled parameters. As a baseline result, the design mission is the first of the missions that is discussed in Section 7.1.1. Its setup is obtained by imposing on the setup depicted in Table 5.1 the state boundary condition that the distance travelled at the final time be  $x(t_f) = 4000$  km, as discussed in Section 5.1.4. Afterwards, an exploratory sensitivity study of the design mission performance metrics to changes in TLDRs is given in Section 7.1.2.

### 7.1.1. Design Mission Trajectory Comparison

The design mission is run for several cost functionals  $\mathcal{J}$  in the form of CIs taking the values 0, 1, and  $\infty$ . As explained in Section 4.1.1, a CI of 0 corresponds to the case where mission duration is deemed “zero times” as important as fuel consumption, i.e. the minimum-fuel mission. A unit CI corresponds to the case in which fuel and time are deemed equally important. Finally, as  $CI \rightarrow \infty$ , the trajectory is driven to its minimum-time solution.

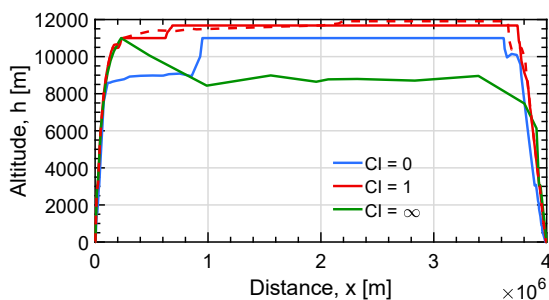


Figure 7.1: The PrP's design mission 2D trajectory for several CIs.

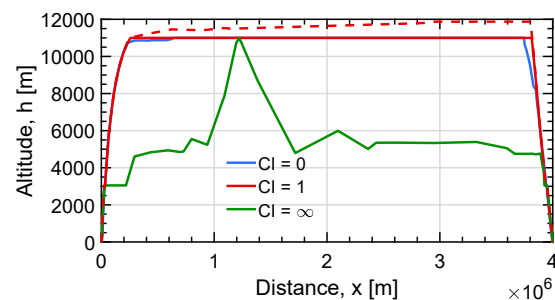


Figure 7.2: The CSR-01's design mission 2D trajectory for several CIs.

The minimum-fuel solutions for both aircraft in Figures 7.1 and 7.2 show rather realistic altitude profiles. The CSR-01 maintains its initial cruise altitude nicely, whereas the PrP seems to postpone its cruise at 11 km to a later instant. Possibly, this is because the solver deems it inefficient to fly at such a high altitude, while the aircraft is still heavy at the start of cruise. This might be an indication that the fuel-optimal cruise altitude of the PrP is actually lower than the imposed cruise altitude of 11 km. This lead is further investigated in Section 7.1.2.

During the mission for  $CI = 1$ , the solver interestingly seems to seek a solution that bypasses the imposed mission profile, for both aircraft. Even though the constraints are set such that the aircraft is allowed to fly two level cruise segments with a step climb in between, the optimisation algorithm has been able to find a loophole: by shortening the level legs and stretching the climb in between, it is able to perform a gradual, fuel-economic climb, indicated with the dashed red line. This gradual-climb solution is shown wherever applicable with a dashed line henceforth, because it nicely shows the capabilities of the optimiser and the intended optimisation strategy, especially.

This behaviour is eliminated by imposing a constraint that the aircraft should climb at an average RoC between 500 ft/min and 1500 ft/min during the step climb flight phase. These values are based on the FAA's Aeronautical Information Manual (AIM)<sup>7</sup>, in which these minimum and maximum RoCs are advised. Shown with the solid red lines in Figures 7.1 and 7.2, it is seen that with this newly imposed constraint, the PrP makes use of the step climb, whereas the CSR-01 maintains its initial altitude throughout cruise.

The reason why the PrP does and the CSR-01 does not make use of the available step climb during cruise can be sought in the respective fuel burns of both aircraft. Considering that the CSR-01 burns approximately 10 t of fuel on this mission and that the PrP burns approximately double that amount, illustrated by Figures 7.3 and 7.4, whereas the mission times are of similar scale, a unit CI index puts the emphasis in the optimal trajectory differently for both aircraft. The PrP is driven to a slightly more fuel-efficient trajectory, whereas the CSR-01 tends towards a faster mission. Hence, the PrP climbs during cruise for fuel economy, whilst the CSR-01 seeks larger temporal gain.

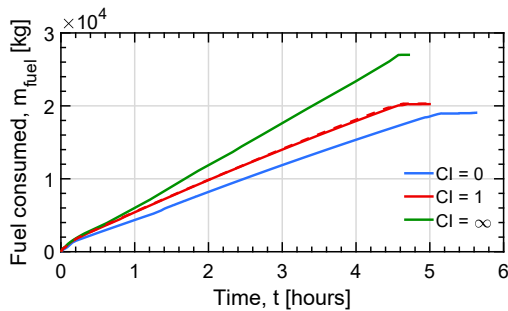


Figure 7.3: The PrP's design mission fuel consumption for several CIs.

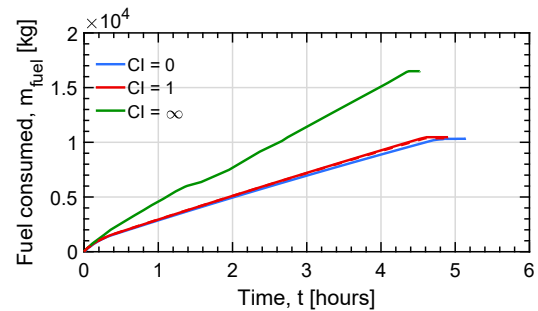


Figure 7.4: The CSR-01's design mission fuel consumption for several CIs.

The difference in optimisation strategy as a result of different CIs is evident, especially in the case of the CSR-01's mission. Contrary to the minimum-fuel mission, the minimum-time solution shown in Figure 7.2 clearly drives the aircraft to a low altitude to maximise its TAS after having reached the imposed initial cruise altitude of  $h_{cr,i}$ . That is, because of the higher speed of sound at lower altitude and the imposed constraint that  $M < M_{MO}$ , flying at lower altitude increases the maximum attainable flight speed, thereby minimising mission time. The same behaviour, though somewhat less pronounced is exhibited by the PrP and shown in Figure 7.1.

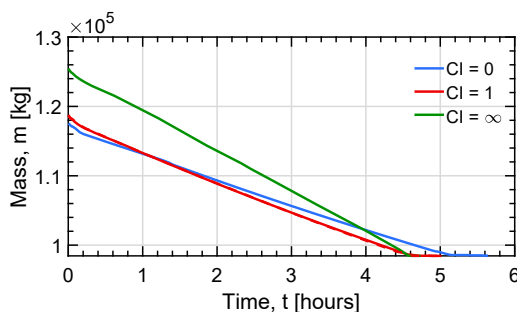


Figure 7.5: The PrP's design mission mass for several CIs.

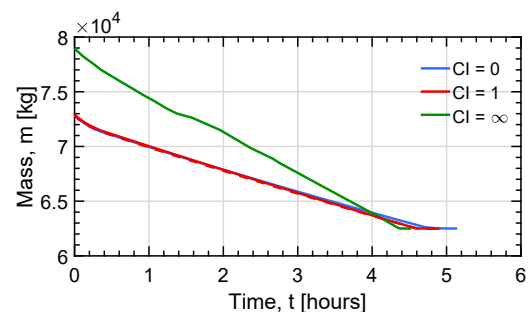


Figure 7.6: The CSR-01's design mission mass for several CIs.

How low both aircraft can fly to maximise their flight velocities is limited by their respective fuel capacities at

<sup>7</sup>URL [https://www.faa.gov/air\\_traffic/publications/atpubs/aim\\_html/chap4\\_section\\_4.html](https://www.faa.gov/air_traffic/publications/atpubs/aim_html/chap4_section_4.html) [Accessed on 13 May, 2020]

maximum payload; both aircraft namely expend all their fuel on the 4000 km minimum-time mission, as seen in Figures 7.3 and 7.4. As shown in Figures 7.5 and 7.6, this means that the aircraft take off at their respective MTOMs, because of the imposed terminal state boundary condition  $m_f = ZFM$ , discussed in Section 5.1.4.

Observing the Mach profiles of both aircraft shown in Figures 7.7 and 7.8, the PrP shows much varying behaviour for the different CIs. Limited by the MO Mach number of  $M_{MO} = 0.79$ , both aircraft obviously seek this upper limit when flying their minimum-time trajectories. Interestingly but somewhat unexpectedly, the minimum-fuel trajectory of the PrP is flown at a much lower Mach number than its design cruise Mach number, whereas the CSR-01's flight Mach numbers for the different CIs are much more in line with expectations. The PrP's tendency to fly at this low velocity for fuel economy warrants a closer investigation.

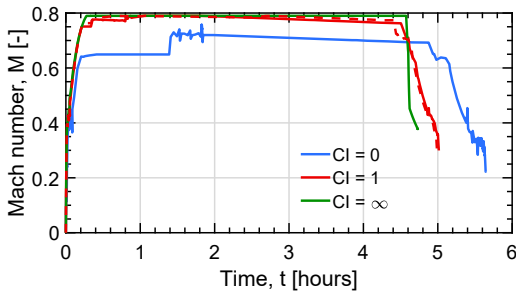


Figure 7.7: The PrP's design mission Mach number for several CIs.

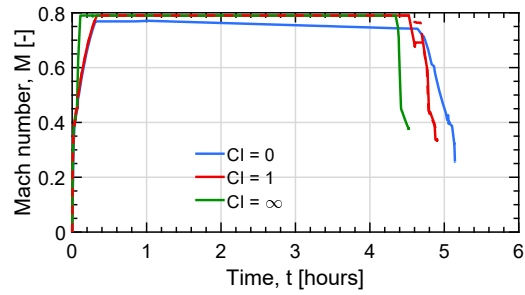


Figure 7.8: The CSR-01's design mission Mach number for several CIs.

Inspection of the Specific Air Range (SAR), the quantity maximised for fuel economy depicted in Figure 7.9, shows that indeed  $M \approx 0.70$  maximises the SAR for the aircraft at its mid-cruise mass, when imposing a cruise altitude of  $h = 11$  km. The SAR is calculated with Equation (7.1) and can be interpreted as the instantaneous flyable distance per unit mass of fuel. Its maximum occurs with the throttle setting  $\tau$  at approximately 84%. With respect to the maximum attainable SAR at maximum thrust setting, the 84% throttle setting gives the aircraft an increase of nearly 8% in SAR. Reducing the throttle setting even further to 70% increases the attainable SAR even further to up to slightly over  $200 \text{ m kg}^{-1}$ , except that steady cruise at an altitude of  $h = 11$  km is not feasible with this amount of thrust. The feasibility boundary is indicated with the line indicating where the available thrust at 84% throttle setting equals the thrust required.

$$\text{SAR} = \frac{V}{\dot{m}_{\text{fuel}}} \tag{7.1}$$

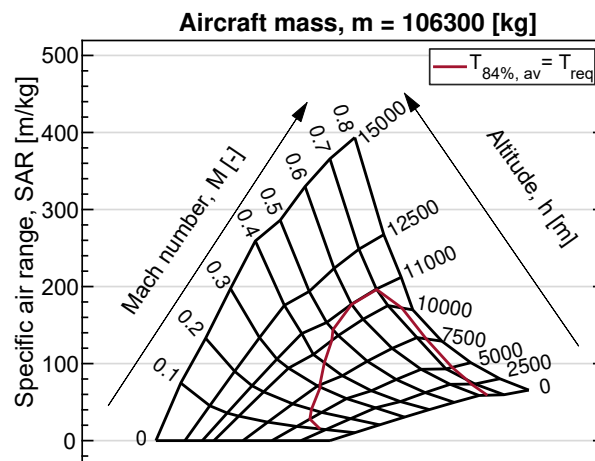


Figure 7.9: The SAR of the PrP as a function of Mach number and altitude for  $\tau = 84\%$  and  $m = 106 \text{ t}$ .

As a final remark it is noted here that the control boundaries are not always respected properly at phase ends by GPOPS-II, as illustrated in Figures 7.10 and 7.11. Here it is seen that at the thrust exceeds the maximum sea-level

available thrust at several time instants. It is thought that this behaviour is a consequence of the underlying LGR quadrature, in which every phase's endpoint is not one of the collocation points.

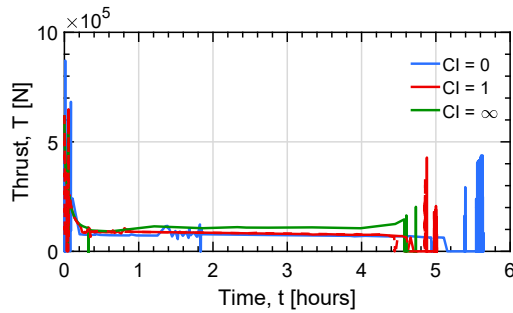


Figure 7.10: The PrP's design mission thrust for several CIs.

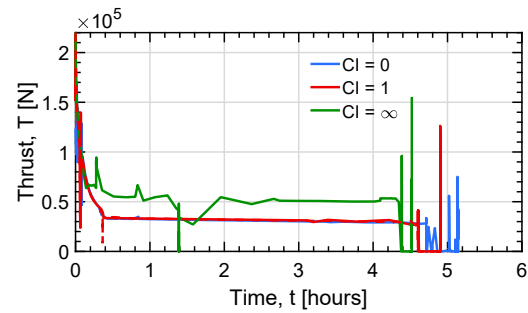


Figure 7.11: The CSR-01's design mission thrust for several CIs.

### 7.1.2. Top-Level Design Requirement Sensitivity

The intent of this section is to present the results of a small study into the PrP's mission performance sensitivity to two selected TLDRs. Specifically, the previous analysis of the design mission has indicated that the PrP might benefit from flying at a different cruise altitude. That is, the obtained trajectories of the PrP hint at the current design cruise altitude not being fuel-optimal for the given mass of the aircraft. Therefore, the sensitivity of the PrP's top-level performance metrics to two TLDRs,  $h_{cr,i}$  and ZFM, will be investigated in this section.

#### Sensitivity to Initial Cruise Altitude

In a first analysis, the same design mission is run for three CIs with this time, however, a freely optimisable initial cruise altitude. Illustrated by Figure 7.12, it becomes evident that for fuel-optimal flight, the PrP should not cruise at its design cruise altitude of 11 km. Instead, the trajectory optimisation indicates that an altitude of approximately 9.3 km would be more appropriate. Not only does the resulting trajectory look much smoother, the additional fuel savings by leaving the initial cruise altitude freely optimisable are considerable with 2.2% with respect to the design range minimum-fuel trajectory with an imposed initial cruise altitude of 11 km. On the other hand, Figure 7.13 indicates that the aircraft flies even more slowly near a Mach number of 0.63 thereby tremendously increasing the mission duration by nearly 7%.

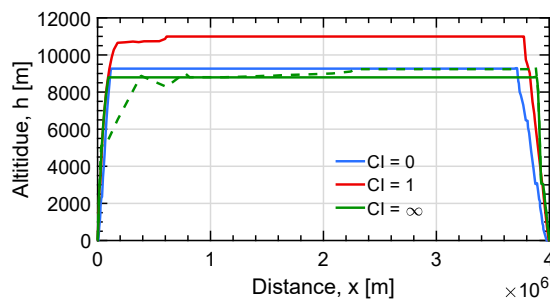


Figure 7.12: The PrP's altitude profile when leaving the initial cruise altitude freely optimisable for several CIs.

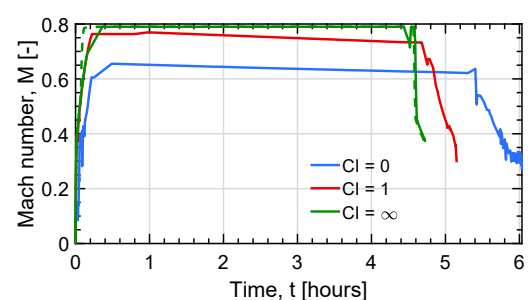


Figure 7.13: The PrP's Mach profile when leaving the initial cruise altitude freely optimisable for several CIs.

In the mission optimised for a unit CI, the solver converges to a cruise altitude of 10 m below the TLDR cruise altitude of 11 km. This indicates that whenever both time and fuel considerations are of equal importance, the design cruise altitude is appropriate. Interestingly, though, the aircraft no longer performs the gradual-climb cruise observed in Figure 7.1. In spite of the seemingly minor trajectory differences, the effects on the fuel performance of the aircraft, shown in Figure 7.15, are notable: flying level cruise at an altitude of 10 990 m gives the aircraft an approximate fuel gain of 1.7% over the design mission for CI = 1. The overall objective function value for this optimal mission is however nearly equal, because the fuel gain is offset by the nearly 2.7% increased mission time.

Remarkably, the optimal altitude in the trajectory optimised for a unit CI does not lie between the altitudes for minimum time and fuel. In the same way as before, the trajectory for minimum time in which the aircraft

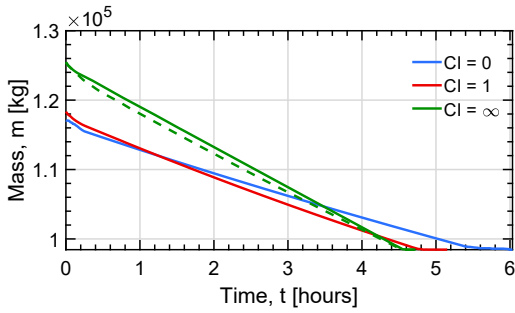


Figure 7.14: The PrP’s mass when leaving the initial cruise altitude freely optimisable for several CIs.

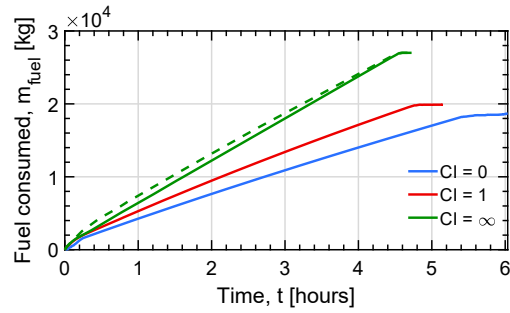


Figure 7.15: The PrP’s fuel consumption when leaving the initial cruise altitude freely optimisable for several CIs.

bypasses the imposed mission profile by performing a gradual-climb cruise is indicated with a dashed (green) line. Apart from the much smoother trajectory, the aircraft gains nearly half a minute with respect to the 11 km initial cruise altitude by flying to its alternative initial cruise altitude of nearly 8.8 km.

### Sensitivity to Zero-Fuel Mass

In a second analysis, the sensitivities of the top-level performance metrics to changes in the PrP’s ZFM is investigated. Assuming an average total passenger mass of 95 kg [35], the ZFM is varied with up to ten times the average passenger mass. A decrease in ZFM simulates the case in which the aircraft takes off with vacant seats. Contrarily, an increase in ZFM simulates the aircraft taking off with “dead weight”, such as unused contingency fuel or extra payload. In any case, the MTOM of the aircraft is kept constant.

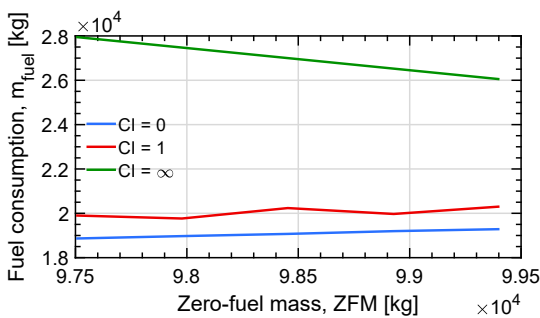


Figure 7.16: The PrP’s absolute fuel consumption as a function of ZFM for several CIs.

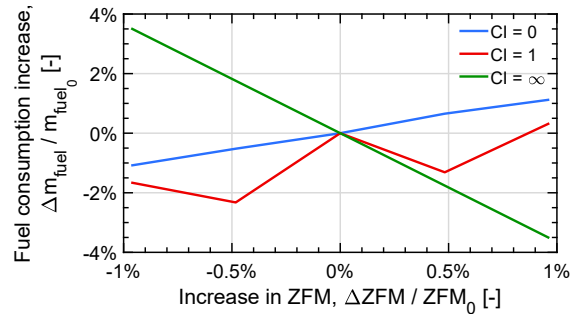


Figure 7.17: The PrP’s relative fuel consumption as a function of changes in ZFM for several CIs.

Illustrated by Figures 7.16 and 7.17, the minimum-fuel missions show a linear relation between the ZFM and the overall fuel consumption of the aircraft. As expected, an increase in ZFM triggers an increase in fuel consumption. This practically linear behaviour is perfectly in line with the behaviour observed in Ref. [45]. Specifically, Figure 7.17 shows that a near 1% increase in ZFM incurs a fuel consumption penalty over 1%, with respect to the baseline ZFM, minimum-fuel mission.

As expected, decreasing the ZFM also decreases the mission time, when flying for minimum time. As illustrated by Figures 7.18 and 7.19, a 1% decrease in ZFM causes an approximate 0.4% decreased mission time. Two effects are at play here. The first and obvious effect is that a decrease in ZFM reduces the dead weight of the aircraft, thereby reducing its overall drag and hence the mission time. The second effect is that a decrease in ZFM at a constant MTOM implies a larger amount of fuel dispensable by the aircraft, as seen in Figures 7.16 and 7.17. As seen previously, the aircraft burn all their fuel trying to fly as low and therefore as fast as possible on the minimum-time missions, directly explaining the increased fuel consumption for a decreased ZFM. Therefore, the larger amount of fuel at its disposal also allows the aircraft to fly lower and hence faster.

A clear trend for the unit CI mission is not easily distinguished. Because the objective function for these missions allows for switching between one flight strategy (minimising fuel) or another (minimising time), a change of ZFM apparently also changes the emphasis the solver puts on either strategy.

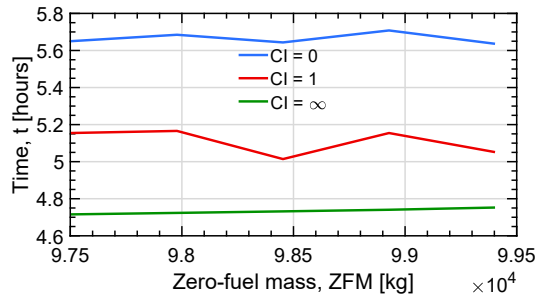


Figure 7.18: The PrP's absolute mission time as a function of ZFM for several CIs.

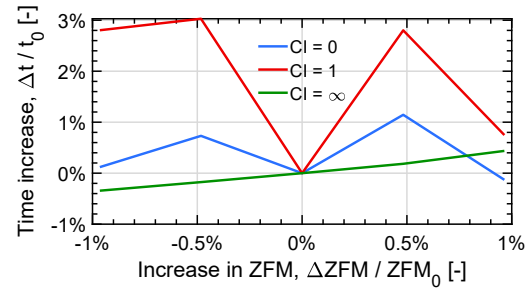


Figure 7.19: The PrP's relative mission time as a function of changes in ZFM for several CIs.

## 7.2. Harmonic Mission Performance

In the same way as before, the harmonic mission, i.e. the mission that maximises the range at maximum payload, is defined by the setup in table 5.1. However, this time no boundary condition is imposed on the final position  $x(t_f)$ . Instead, the objective function is defined as  $\mathcal{J} = -x(t_f)$  to maximise the range. This implies that in this analysis, no distinction is made between CIs, as was the case for the previous analyses. After all, maximising the range, one cannot simultaneously optimise for minimum fuel, time, or a combination thereof.

The 2D trajectories of the PrP and CSR-01 are shown in Figure 7.20, in which the range advantage of the CSR-01 is clearly recognised. Again, the gradual-climb trajectories are indicated with dashed lines. At a maximum range of approximately 5420 km, the design point of the PrP clearly lies in a range segment even shorter than the CSR-01, which is capable of travelling around 6200 km. Unsurprisingly, the trends in the altitude profiles show striking resemblance to those in the design mission minimum-fuel trajectories. After all, both maximum-range and minimum-fuel missions seek to maximise the SAR.

The same resemblance holds for the trends that are shown for the Mach number in Figure 7.21; whereas the CSR-01 flies at or near its design cruise Mach number for fuel-economic travel, the PrP flies notably slower. The same explanation as before holds for the slow flight in this case.

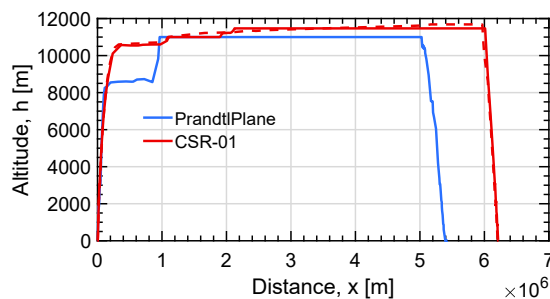


Figure 7.20: The PrP and CSR-01's harmonic mission 2D trajectories.

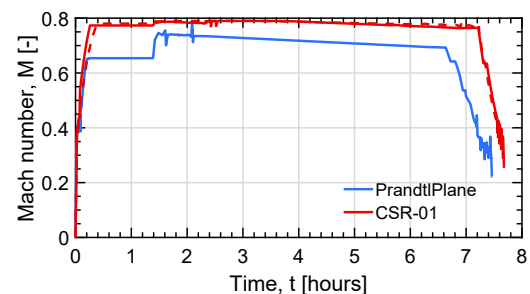


Figure 7.21: The PrP and CSR-01's harmonic mission Mach number.

Both aircraft make full use of their fuel capacity at maximum payload, as shown in Figures 7.22 and 7.23. As before, the mission is set up in such a way that the aircraft arrive at their destination at their respective ZFMs. Flying their maximum range, the aircraft take off at MTOM.

## 7.3. Top-level Mission Performance for Various Ranges

The aim of this section is to view the results obtained for different mission ranges and different optimisation metrics in a different light. Rather than looking at each mission's trajectory specifics, a more zoomed-out stance will be taken in this section, to gain insight on the performance of both aircraft on a higher level.

Starting with the two most rudimentary performance indices that have been subject of previous discussions, too, both aircraft's temporal and fuel performance are shown in Figures 7.24 and 7.25. It is immediately clear that the high-CI missions have little application for real life commercial airliners. Indeed, marginal temporal gain induces an enormous fuel expense for both aircraft. By flying for minimum time, the PrP is able to decrease its

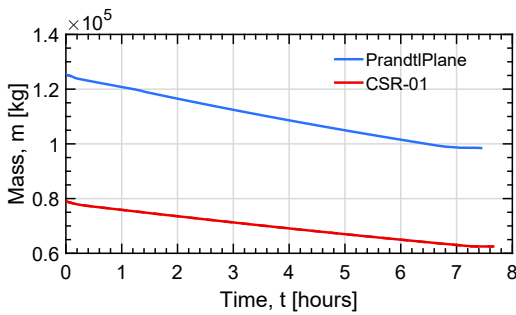


Figure 7.22: The PrP and CSR-01's harmonic mission mass.

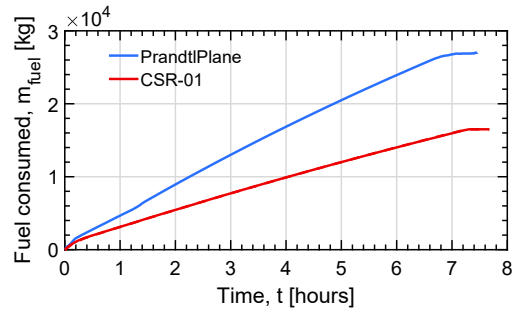


Figure 7.23: The PrP and CSR-01's harmonic mission fuel consumption.

mission time by nearly 16.2 % at the cost of over 41.5 % more fuel, with respect to the 4000 km minimum-fuel mission. Likewise, the CSR-01 consumes nearly 60 % more fuel to fly a 12.1 % faster mission.

Confirming the earlier findings that the PrP tends to fly slower than its competitor, the curves in Figure 7.24 corresponding to those of the PrP are generally steeper, indicating a lower average velocity, than those corresponding to the CSR-01. The CSR-01 has an approximately 10 % higher average velocity on the minimum-fuel missions. On the minimum-time missions, the average velocity of the CSR-01 is approximately equal to that of the PrP on the 2000 km range mission, over 4.5 % higher on the 4000 km mission, and nearly 12 % higher on the maximum-range mission.

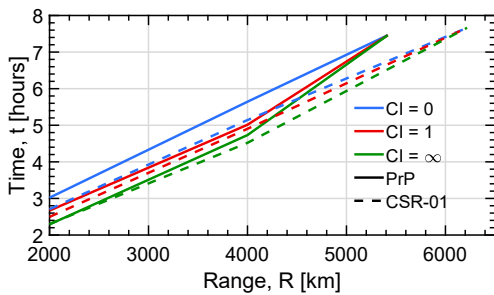


Figure 7.24: The PrP and CSR-01 mission time as a function of CI and range.

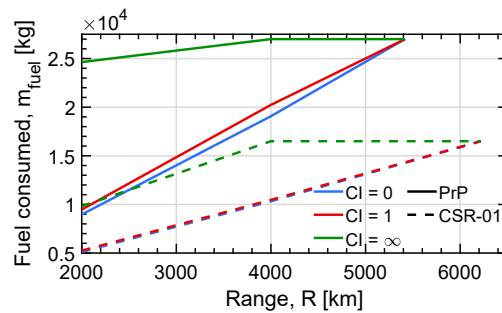


Figure 7.25: The PrP and CSR-01 fuel consumption as a function of CI and range.

The PrP outperforms the CSR-01 in terms of relative fuel consumption. Whereas in absolute terms, the fuel consumption of the PrP is obviously higher, the PrP carries over twice as many passengers as the CSR-01. Displayed in Figures 7.26 and 7.27 are the respective PrP and CSR-01 fuel burn per passenger and fuel burn per passenger-kilometre for several ranges and CIs. At a fuel consumption of approximately 15 g/pax/km, the PrP is 14.5 % more efficient than its competitor on the short-range, minimum-fuel mission, 10 % on the design range minimum-fuel mission, and nearly 8.5 % on the maximum-range mission.

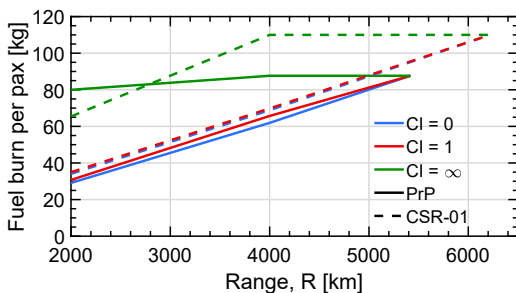


Figure 7.26: The PrP and CSR-01 fuel consumption per seat as a function of CI and range.

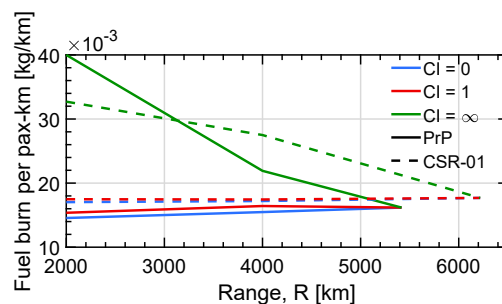
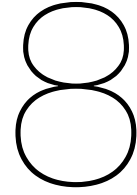


Figure 7.27: The PrP and CSR-01 fuel consumption per seat-kilometre as a function of CI and range.

Obviously, the CSR-01 is more versatile than the PrP in terms of employability due to its higher maximum range. Of course, this is one of the premises of the PrP design intent; to design an aircraft that delivers efficient flights in the short-range segment.

As a concluding remark, it is noted here that the trajectory optimisation tool lacks somewhat in performance, especially in two respects. First of all, the runtimes necessary to solve these trajectory optimisation problems are rather long. The optimal trajectories discussed in this chapter typically take hours to complete. Secondly, inputting problems with more than approximately 20 flight phases also troubles convergence to an optimal solution, possibly because of the large dimensionality of the problem. Moreover, convergence is troubled by inputting noisy tabular data, because of the consequent non-convexity of the problem.



# Unconventional Control Benefits

This chapter aims at presenting the results of the analyses that have been run to quantify the benefits of allowing DLC. Logically, adopting the redundant flight deflective controls is expected to bring about a performance benefit. After all, the conventionally controlled optimal trajectory, without deflecting any control surfaces, is still a valid solution to the DLC-enabled trajectory optimisation problem. Therefore, the solution obtained when allowing DLC should be at least as good as the conventional-control trajectory.

The first thing that stands out when inspecting the obtained solution is that the aircraft deflects all its moveables simultaneously and by the same amount, at all times. Therefore, only a single moveable deflection per mission is visible in Figure 8.1. In essence, this means that allowing only single control DoF accounting for all moveables' deflections would have sufficed upon setting up the problem. Intuitively, this holds true for the model used. After all, no moveable-specific aerodynamics have been used, except for a factor scaling the attainable  $C_L$  and  $C_D$  per moveable. Because no rotational dynamics are considered, the primary deflection consideration is the incremental lift-to-drag ratio, which is equal for all control surfaces for a given deflection.

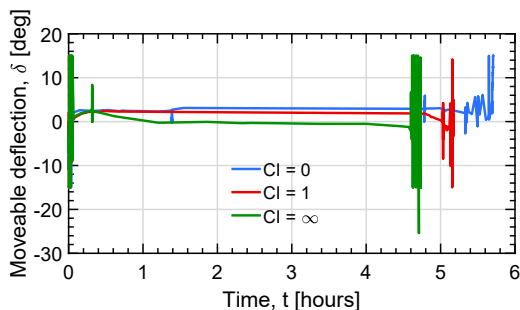


Figure 8.1: The PrP's moveable deflections for several CIs.

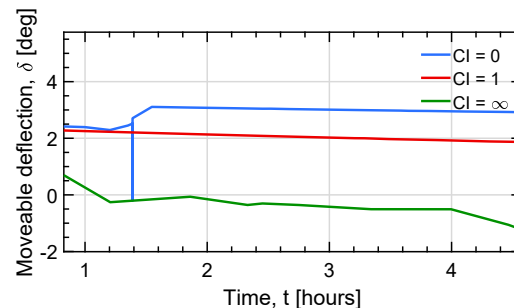


Figure 8.2: The PrP's moveable deflections for several CIs in cruise.

Moreover, it is very interesting to note how the aircraft doesn't deflect the control surfaces excessively during cruise. Rather, the deflective controls are used in a more subtle, variable-camberlike way. During the other phases, however, the control surface deflections are highly oscillatory, such that meaningful interpretation of the results is hindered. Therefore, the interpretation of the results will be limited to the cruise phase.

The different CIs cause the aircraft to vary the camber of the aerofoil differently during cruise. For the minimum-fuel mission, the aircraft uses the variable camber primarily to increase the aerodynamic efficiency. At start of cruise, the aircraft is heavier and needs to fly at a slightly higher lift coefficient. As the aircraft burns fuel and loses weight over time, it decreases the moveables' deflections slightly, resulting in a decrease of incremental lift. This is more easily seen in Figure 8.2, in which the cruise portion of the figure has been enhanced.

Contrarily, in the minimum-time mission, the aircraft uses the additional control to slightly increase the down-force on the aircraft as it loses weight during the cruise phase. At the cost of a slight control drag penalty, decreasing lift during cruise seems counter-intuitive. However, the aircraft apparently incurs a slightly lower overall drag penalty by decreasing the camber and consequently flying at a slightly higher angle of attack. It should,

however, be noted that the incremental lift and drag resulting from this deflection are practically nil, as shown in Figures 8.3 and 8.4. Note that the graphs have been clipped vertically, to promote readability.

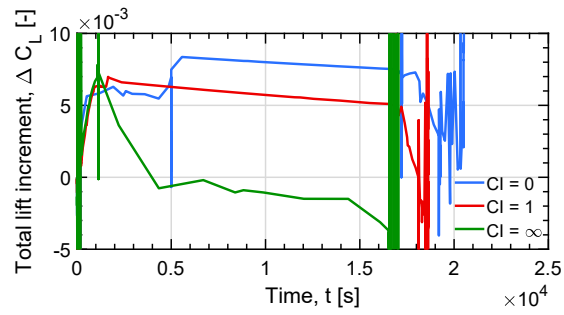


Figure 8.3: The PrP's total lift increment due to DLC.

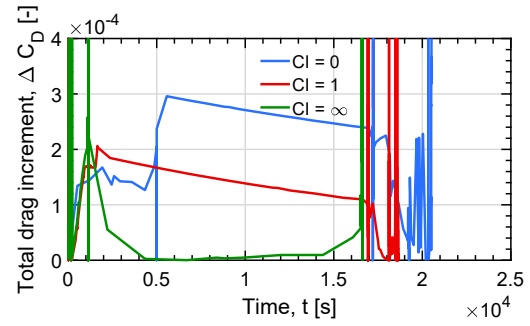


Figure 8.4: The PrP's total drag increment due to DLC.

Inspection of Figures 8.5 and 8.6 shows that the Mach and altitude profiles of the DLC-controlled missions don't differ substantially from the original, regularly controlled missions. One remarkable difference is observed in the altitude profile for a unit CI. With DLC enabled, the aircraft no longer tries to gradual-climb cruise, as was previously the case. A possible explanation for this is that variable camber now gives the aircraft an alternative way of fuel-optimising the cruise phase. In the regularly controlled mission, the aircraft bypassed the imposed level cruise flight constraint to perform a gradual-climb cruise. However, enablement of variable camber has proved an alternative way of dealing with the weight decrease during cruise, such that cruise-climb is no longer a necessity for fuel economy.

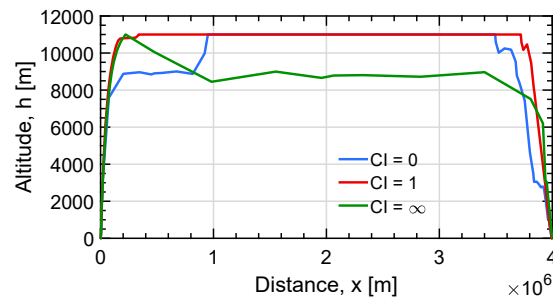


Figure 8.5: The PrP's 2D trajectory, while enabling DLC.

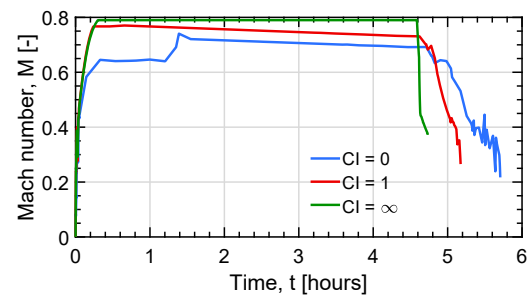


Figure 8.6: The PrP's Mach profile, while enabling DLC.

Zooming out to the missions' top-level performance metrics, the aircraft gains only marginally in its performance by the enablement of DLC. On the minimum-fuel mission, the fuel consumption is decreased by nearly 0.6%. Optimising for minimum time, the mission duration is negligibly decreased with seconds with respect to the regularly controlled mission.

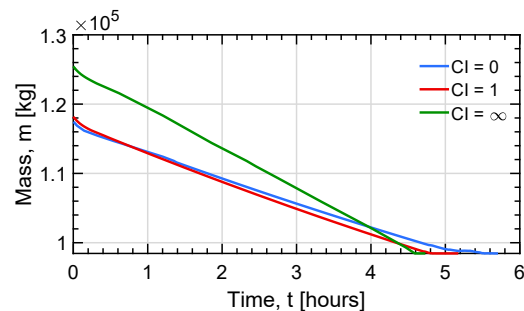


Figure 8.7: The PrP's mass, while enabling DLC.

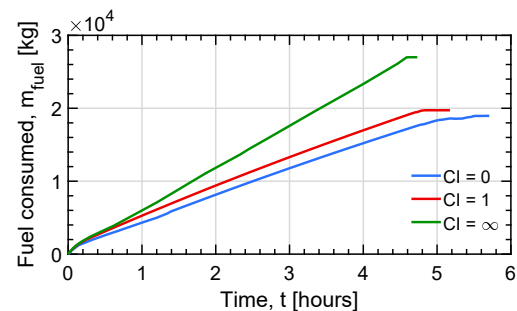


Figure 8.8: The PrP's fuel consumption, while enabling DLC.

It is again stressed here that these results should be interpreted with appropriate caution. In these results, the discretisation errors from numerical resolution of the trajectory optimisation problem were not assessed and therefore

also not mitigated, subsequently. Moreover, aircraft trim has not been considered and a simplified model for the aircraft's control surface aerodynamics was used.

On the other hand, the potential benefits of DLC might be underestimated because the sluggishness of the aircraft's pitch control is not modelled. As mentioned in Section 2.3.1, application of DLC is especially beneficial to those aircraft that exhibit large pitch damping. However, this effect is not captured because of rotational dynamics are disregarded, as explained in Section 3.1.1. Nevertheless, the instants at which the aircraft changes its attitude are of short duration with respect to the mission duration, such that the benefits of DLC might be captured better by high-frequency flight dynamics simulations.



## Conclusions and Recommendations

The aim of this research has been to assess the mission performance of a box-wing aircraft by developing a configuration-agnostic, multi-fidelity optimal control toolbox for performance and mission analysis. Specifically, the box-wing aircraft under investigation is one designed for the short range and a high passenger capacity. Because of the similar design range, the aircraft's performance is compared to that of the CSR-01, a substitute model for the A320.

First of all, the conclusions of the report are presented in the form of answers to the research questions posed in the introduction of the report. Afterwards, recommendations for future work related to the current research are given.

### Conclusions

The main research question posed in this work is: *how does the PrP perform when flying its optimal mission, for a given range?* To answer this question, two subsidiary research questions were posed. The primary sub-question pertains to how the PrP's trajectory compares to that of its competitor aircraft. The secondary sub-question pertains to how large the performance gain due to the enablement of DLC is. In the same way as the subsidiary research questions, the conclusions of this report are twofold.

### PrandtlPlane Mission Performance

To analyse the performance of the PrP with respect to its competitor, an aircraft trajectory optimisation tool has been developed. Physically, the aircraft are regarded as a point mass, implying that rotational dynamics and trim are not considered. Moreover, use was made of TUD in-house software to obtain both aircraft's aerodynamic and propulsive data sets. Subsequently, an optimal control approach was taken to resolve the trajectory optimisation problem.

Analysis of both aircraft's optimal trajectories for various ranges and CIs has shown that the PrP outperforms its competitor in terms of relative fuel consumption, when flying for minimum fuel. Illustrated by Figure 9.1, the PrP uses up to nearly 15 % less fuel per passenger per kilometre than its competitor on its fuel-optimal missions.

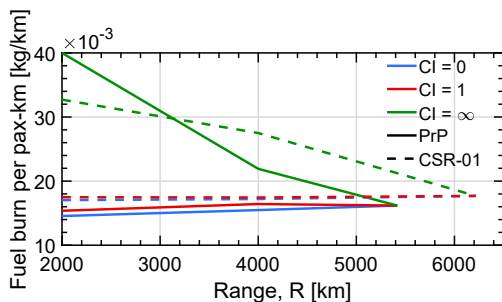


Figure 9.1: The PrP and CSR-01 fuel consumption per seat-kilometre as a function of CI and range.

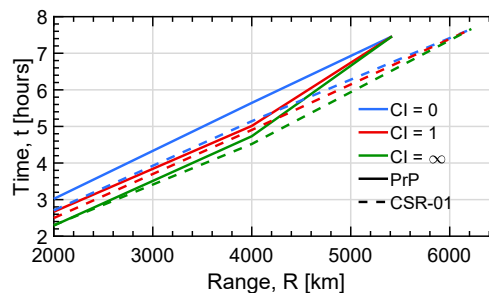


Figure 9.2: The PrP and CSR-01 mission time as a function of CI and range.

Nonetheless, the PrP's superior fuel-per-passenger performance comes at the cost of inferior performance in other respects, as illustrated by Figure 9.2. First of all, the PrP's harmonic range of 5400 km is much shorter than its competitor's maximum range at maximum payload of 6200 km. Secondly, in contrast to its competitor, the PrP flies approximately 0.1 slower than its cruise Mach number for fuel economy, thereby flying nearly 10 % slower on average than its competitor to complete the 4000 km design mission. In general, the PrP flies nearly all its trajectories slower than its competitor, with the exception of the short-range, minimum-time mission.

In the fuel-optimal design mission, the PrP postpones its cruise at 11 km to a later instant, possibly indicating that the cruise altitude TLDR might not be fuel-optimal. Investigating the possibility that the PrP might benefit from a different cruise altitude altogether showed that, indeed, the PrP rather flies its fuel-optimal trajectory at lower cruise altitudes of 9.3 km for a 2.2 % decrease in fuel consumption at the cost of a nearly 7 % longer flight duration. Nevertheless, when both fuel and time considerations are taken into account, the 11 km cruise altitude is deemed appropriate.

Changes in the ZFM of the PrP alter the performance of the aircraft notably. When flying for fuel economy, the change in fuel consumption is directly proportional to the change in ZFM; a 1 % increase in ZFM results in an increase in fuel consumption over 1 %. When flying for minimum time, a similar direct proportionality holds; a 1 % decrease in ZFM causes a near half percent decreased mission time at the cost of increased fuel consumption. Namely, a decrease in ZFM at constant MTOM implies that the aircraft has more fuel at its disposal during the mission, thereby allowing it to fly lower and thus faster.

### PrandtlPlane Direct Lift Control Benefits

Because of the PrP's redundant front and rear wing control surfaces, it can deflect its moveables in such a way, that it generates a net increase in lift without altering the pitching moment. Together with changing its angle of attack by pitching up or down, DLC is a redundant, instantaneous means of controlling the lift. Considering only the increased number of control DoFs, it should therefore logically enhance the performance of the PrP.

To enable a flight dynamics simulation with DLC, an alternative model was used for the control surface aerodynamics. Because the aerodynamic data obtained by analyses in VSAERO resulted in unrealistic incremental drag due to control surface deflections, it was chosen to model the incremental lift and drag differently altogether. Instead, the results of an empirical study were used, giving the incremental lift and drag as a function of the trailing edge flap deflection of a flat plate in a compressible flow, thereby capturing wave drag effects dominant in the transonic regime. The two-dimensional incremental lift and drag coefficients of this study were subsequently corrected for three-dimensional vortex drag effects.

In the optimal trajectories, the aircraft deflects all its control surfaces simultaneously and by the same amount at all times, even though this behaviour was not explicitly imposed. This is thought to be a consequence of the aerodynamic control surface model that is used, which includes no actual control surface geometry specifics, except for a factor scaling the incremental lift and drag coefficients. Moreover, because no rotational dynamics are considered, the primary consideration in using the deflective controls is the attainable incremental lift-to-drag ratio, which is equal for each control surface.

Using the deflective controls to only subtly vary camber during cruise, the PrP benefits only marginally from the redundant controls. Specifically, the projected mission time savings, when flying for minimum time, are in the order of seconds and hence negligible. The fuel savings per passenger per kilometre with respect to its fuel-optimal, 4000 km design mission are estimated at 0.6 %. In view of both the used flat-plate approximation and the discretisation uncertainties that inevitably come with numerical resolution of the trajectory analysis, appropriate caution should be exercised when using these numbers in an absolute sense.

## Recommendations

### Recommendations for Future Research

In future research, it is advised that trim considerations be taken into account. It is still not feasible to consider trim during the trajectory optimisation, because of the associated computational effort. However, an a posteriori study into the trim feasibility of the trajectories presented in this work might already provide valuable information. Moreover, this way one might be able to estimate the fuel required for trimming the aircraft, by approximation.

Moreover, it would be interesting to investigate how the aerodynamic design of the PrP can be refined to alter the fuel-optimal altitude and Mach number. As the PrP has to fly significantly slower and lower than its TLDRs for fuel economy, it might be of interest to incorporate these findings in another design iteration. For example, one might choose to reconsider these TLDRs or to refine the aerodynamic design such that the aircraft flies fuel-optimally at a Mach number and altitude closer to its TLDRs.

Due to limited time resources not performed within the current study, an error quantification and, subsequently, a grid refinement study would provide useful information about the confidence bounds of the results presented within this work. Inevitably, resolution of the problem on a discretised temporal mesh introduces uncertainties in the solution. Even though the obtained solution is exact at the collocation points by construction, numerical errors are present in between collocation points. Error quantification and automatic grid refinement functionality is already present within GPOPS-II.

## Recommendations for Software Improvement

Although not strictly necessary, the toolbox code can be made more accessible by replacing the commercial software GPOPS-II by similar optimal control transcription software. For example, Imperial College London Optimal Control Software (ICLOCS) seems to be a versatile alternative to GPOPS-II.<sup>8</sup>

Additionally, the trajectory optimisation tool may further be developed by streamlining the code. Currently, the runtime of a typical aircraft mission is very long. Even though this is partially attributable to the noisy propulsive and aerodynamic data sets, code performance can undoubtedly be enhanced in other respects, too.

Finally, the developed program provides a framework in which different physics models can easily be implemented and added. It is therefore hoped that the current tool serves as a starting point for a TUD in-house trajectory optimisation tool. The tool can be modularly expanded with other trajectory models used in future researches studying for example short-time, single-maneuvre trajectory optimisation or the effect of wind on aircraft performance. With such expansions, the work of researchers will become more easily reusable.

---

<sup>8</sup>URL <http://www.ee.ic.ac.uk/ICLOCS/> [Accessed on 28 May, 2020]



# Bibliography

- [1] J. T. Betts and W. P. Huffman, “Mesh refinement in direct transcription methods for optimal control,” *Optimal Control Applications and Methods*, vol. 19, no. 1, pp. 1–21, 1998.
- [2] J. T. Betts, “Survey of numerical methods for trajectory optimization,” *Journal of guidance, control, and dynamics*, vol. 21, no. 2, pp. 193–207, 1998.
- [3] M. Darecki, C. Edelstenne, T. Enders, E. Fernandez, P. Hartman, J.-P. Herteman, M. Kerkloh, I. King, P. Ky, M. Mathieu, *et al.*, “Flightpath 2050 europe’s vision for aviation,” *Off. Eur.*, 2011.
- [4] A. Gittens, J. Poole, A. de Juniac, F. Liu, and J. Pie, “Aviation benefits,” report, ICAO AI CANSO IATA ICCAIA, 2017.
- [5] Airbus S.A.S., “Global market forecast cities, airports & aircraft 2019 - 2038,” 2019.
- [6] S. Alam, M. Nguyen, H. Abbass, C. Lokan, M. Ellejmi, and S. Kirby, “Multi-aircraft dynamic continuous descent approach methodology for low-noise and emission guidance,” *Journal of Aircraft*, vol. 48, no. 4, pp. 1225–1237, 2011.
- [7] ICAO, *Continuous Descent Operations (CDO) Manual*. ICAO, 1 ed., 2010.
- [8] A. Nuic, D. Poles, and V. Mouillet, “Bada: An advanced aircraft performance model for present and future atm systems,” *International Journal of Adaptive Control and Signal Processing*, vol. 24, no. 10, pp. 850–866, 2010.
- [9] F. Faggiano, R. Vos, M. Baan, and R. Van Dijk, “Aerodynamic design of a flying v aircraft,” 2017.
- [10] A. Frediani, V. Cipolla, and E. Rizzo, *The PrandtlPlane configuration: overview on possible applications to civil aviation*, pp. 179–210. Springer, 2012.
- [11] Y. Liu, A. Elham, P. Horst, and M. Hepperle, “Exploring vehicle level benefits of revolutionary technology progress via aircraft design and optimization,” *Energies*, vol. 11, no. 1, p. 166, 2018.
- [12] R. Martinez-Val and E. Schoep, “Flying wing versus conventional transport airplane: the 300 seat case,” 2000.
- [13] A. Frediani, V. Cipolla, K. Abu Salem, V. Binante, and M. Picchi Scardaoni, “On the preliminary design of prandtlplane civil transport aircraft,” in *7th Eucass Conference, Milan*, 2017.
- [14] P. Okonkwo and H. Smith, “Review of evolving trends in blended wing body aircraft design,” *Progress in Aerospace Sciences*, vol. 82, pp. 1–23, 2016.
- [15] R. Cavallaro and L. Demasi, “Challenges, ideas, and innovations of joined-wing configurations: a concept from the past, an opportunity for the future,” *Progress in Aerospace Sciences*, vol. 87, pp. 1–93, 2016.
- [16] M. Voskuijl, J. de Klerk, and D. van Ginneken, *Flight Mechanics Modeling of the PrandtlPlane for Conceptual and Preliminary Design*, pp. 435–462. Boston, MA: Springer US, 2012.
- [17] G. La Rocca and M. Van Tooren, “Enabling distributed multi-disciplinary design of complex products: a knowledge based engineering approach,” *Journal of Design Research*, vol. 5, no. 3, pp. 333–352, 2007.
- [18] M. Voskuijl, G. La Rocca, and F. Dircken, “Controllability of blended wing body aircraft,” in *Proceedings of the 26th International Congress of the Aeronautical Sciences, ICAS 2008, including the 8th AIAA Aviation Technology, Integration and Operations (AIO) Conference, Anchorage, Alaska, September 14-19, (2008)*, Optimage Ltd., 2008.

- [19] P. Wu, M. Voskuijl, and L. Veldhuis, “An approach to estimate aircraft touchdown attitudes and control inputs,” *Aerospace Science and Technology*, vol. 71, pp. 201–213, 2017.
- [20] L. Prandtl, “Induced drag of multiplanes,” Report NACA-TN-182, NACA, 1924.
- [21] L. W. Traub, “Unified approximation for nonparabolic drag polars,” *Journal of aircraft*, vol. 44, no. 1, pp. 343–346, 2007.
- [22] A. Frediani and G. Montanari, *Best wing system: an exact solution of the Prandtl’s problem*, pp. 183–211. Variational Analysis and Aerospace Engineering, New York, NY: Springer New York, 2009.
- [23] L. Demasi, G. Monegato, E. Rizzo, R. Cavallaro, and A. Dipace, “Minimum induced drag theorems for joined wings, closed systems, and generic biwings: Results,” in *56th AIAA/ASCE/AHS/ASC Structures, Structural Dynamics, and Materials Conference*, p. 0698, 2015.
- [24] M. M. Munk, “The minimum induced drag of aerofoils,” Report NACA-TR-121, NACA, 1923.
- [25] DLR, TUD, UNIPI, and SKYBOX, “Report on socio-economic scenarios and expectations,” report, DLR TUD UNIPI SKYBOX, 2017.
- [26] A. Frediani, V. Cipolla, K. A. Salem, V. Binante, and M. P. Scardaoni, “Conceptual design of prandtlplane civil transport aircraft,” *Proceedings of the Institution of Mechanical Engineers, Part G: Journal of Aerospace Engineering*, vol. 0, no. 0, p. 0954410019826435, 2018.
- [27] I. Terekhov and V. Gollnick, “A concept of forecasting origin-destination air passenger demand between global city pairs using future socio-economic scenarios.”
- [28] V. Cipolla, A. Frediani, K. Abu Salem, M. Picchi Scardaoni, A. Nuti, and V. Binante, “Conceptual design of a box-wing aircraft for the air transport of the future,” 2018. doi:10.2514/6.2018-3660.
- [29] I. C. A. Organization, “International standards and recommended practices: Annex 14 to the convention on international civil aviation: Aerodromes. aerodrome design and operations,” 2004.
- [30] K. Risse, K. Schäfer, F. Schültke, and E. Stumpf, “Central reference aircraft data system (ceras) for research community,” *CEAS Aeronautical Journal*, vol. 7, no. 1, pp. 121–133, 2016.
- [31] C. Varriale, A. Raju Kulkarni, G. La Rocca, and M. Voskuijl, “A hybrid, configuration-agnostic approach to aircraft control surface sizing,” 2019.
- [32] D. Drake, “Direct lift control during landing approaches,” in *2nd Annual Meeting*, p. 316, 1965.
- [33] W. Pinsker, “The control characteristics of aircraft employing direct-lift control,” Report 0114703299, HM Stationery Office, 1970.
- [34] D. Amato, “Direct lift control of a prandtlplane aircraft for improved landing performances,” thesis, 2019.
- [35] C. Varriale, “Aircraft performance analysis and mission profile optimization,” report, Delft University of Technology, 2018.
- [36] M. Carini, M. Méheut, L. Sanders, S. Kanellopoulos, C. Varriale, G. La Rocca, K. Abu Salem, V. Cipolla, A. Frediani, and V. Binante, “Aerodynamic and acoustic analysis of the baseline prandtlplane,” Report 4.1, ONERA, 2019.
- [37] M. Bartel and T. M. Young, “Simplified thrust and fuel consumption models for modern two-shaft turbofan engines,” *Journal of Aircraft*, vol. 45, no. 4, pp. 1450–1456, 2008.
- [38] D. Raymer, *Aircraft design: a conceptual approach*. American Institute of Aeronautics and Astronautics, Inc., 1992.
- [39] Y. Zhao and R. A. Slattery, “Capture conditions for merging trajectory segments to model realistic aircraft descents,” *Journal of guidance, control, and dynamics*, vol. 19, no. 2, pp. 453–460, 1996.
- [40] N. X. Vinh, *Optimal trajectories in atmospheric flight*. Elsevier, 1981.

- [41] F. Fisch, *Development of a framework for the solution of high-fidelity trajectory optimization problems and bilevel optimal control problems*. PhD thesis, Technische Universität München, 2011.
- [42] G. Ruijgrok, *Elements of airplane performance*. VSSD, 2009.
- [43] L. E. Fogarty and R. M. Howe, “Computer mechanization of six-degree of freedom flight equations,” *Simulation*, vol. 11, no. 4, pp. 187–193, 1968.
- [44] A. Raju Kulkarni, C. Varriale, M. Voskuijl, G. La Rocca, and L. L. Veldhuis, “Assessment of sub-scale designs for scaled flight testing,” 17-06-2019 2019.
- [45] M. Soler, A. Olivares, E. Staffetti, and J. Cegarra, “Multi-phase optimal control applied to 4d business trajectory strategic planning in air traffic management,” in *Proceedings of the 1st International Conference on Application and Theory of Automation in Command and Control Systems*, pp. 68–78, 2011.
- [46] J. Sun, J. M. Hoekstra, and J. Ellerbroek, “Aircraft drag polar estimation based on a stochastic hierarchical model,” 2018.
- [47] B. W. McCormick, *Aerodynamics, aeronautics, and flight mechanics*. John Wiley & Sons, Inc., 2 ed., 1995.
- [48] M. Drela, *XFOIL: An analysis and design system for low Reynolds number airfoils*, pp. 1–12. Springer, 1989.
- [49] K.-M. Chung, “Aerodynamic characteristics of deflected surfaces in compressible flows,” *Journal of aircraft*, vol. 41, no. 2, pp. 415–418, 2004.
- [50] J. H. McMasters, D. J. Paisley, R. J. Hubert, I. Kroo, K. K. Bofah, J. P. Sullivan, and M. Drela, “Advanced configurations for very large subsonic transport airplanes,” report, NASA, 1996.
- [51] P. Proesmans, “Preliminary propulsion system design and integration for a box-wing aircraft configuration, a knowledge based engineering approach,” thesis, 2019.
- [52] W. P. Visser, *Generic Analysis Methods for Gas Turbine Engine Performance: The development of the gas turbine simulation program GSP*. PhD thesis, Technische Universiteit Delft, 2014.
- [53] J. T. Betts, *Practical methods for optimal control and estimation using nonlinear programming*, vol. 19. Siam, 2010.
- [54] M. Soler, A. Olivares, and E. Staffetti, “Multiphase optimal control framework for commercial aircraft four-dimensional flight-planning problems,” *Journal of Aircraft*, vol. 52, no. 1, pp. 274–286, 2015.
- [55] M. A. Patterson and A. V. Rao, “GPOPS-II: A matlab software for solving multiple-phase optimal control problems using hp-adaptive gaussian quadrature collocation methods and sparse nonlinear programming,” *ACM Transactions on Mathematical Software (TOMS)*, vol. 41, no. 1, p. 1, 2014.
- [56] S. Hartjes and H. Visser, “Optimal control approach to helicopter noise abatement trajectories in nonstandard atmospheric conditions,” *Journal of Aircraft*, vol. 56, no. 1, pp. 43–52, 2019.
- [57] S. Hartjes, *An Optimal Control Approach to Helicopter Noise and Emissions Abatement Terminal Procedures*. PhD thesis, Technische Universiteit Delft, 2015.
- [58] V. M. Becerra, *Practical direct collocation methods for computational optimal control*, pp. 33–60. Springer, 2012.
- [59] C. R. Hargraves and S. W. Paris, “Direct trajectory optimization using nonlinear programming and collocation,” *Journal of Guidance, Control, and Dynamics*, vol. 10, no. 4, pp. 338–342, 1987.
- [60] G. T. Huntington and A. V. Rao, “Comparison of global and local collocation methods for optimal control,” *Journal of Guidance, Control, and Dynamics*, vol. 31, no. 2, pp. 432–436, 2008.
- [61] D. Garg, M. Patterson, W. Hager, A. Rao, D. Benson, and G. Huntington, “An overview of three pseudospectral methods for the numerical solution of optimal control problems,” 2017.

- [62] A. Wächter, “Short tutorial: getting started with ipopt in 90 minutes,” in *Dagstuhl Seminar Proceedings* (U. Naumann, O. Schenk, H. D. Simon, and S. Toledo, eds.), Schloss Dagstuhl-Leibniz-Zentrum fuer Informatik, 2009.
- [63] H. G. Visser, “Terminal area traffic management,” *Progress in Aerospace Sciences*, vol. 28, no. 4, pp. 323–368, 1991.
- [64] R. E. Perez and P. W. Jansen, “Coupled aircraft design and staging assignment for long-range operations,” *Journal of Aerospace Operations*, vol. 4, no. 4, pp. 223–243, 2017.
- [65] D. G. Hull, *Fundamentals of airplane flight mechanics*. Springer, 2007.
- [66] D. Wu and Y. Zhao, “Optimization and sensitivity analysis of climb and descent trajectories for reducing fuel burn and emissions,” in *11th AIAA Aviation Technology, Integration, and Operations (ATIO) Conference, including the AIAA Balloon Systems Conference and 19th AIAA Lighter-Than-Air Systems Technology (LTA) Conference*, p. 6879, 2011.
- [67] J. Gagné, A. Murrieta, R. M. Botez, and D. Labour, “New method for aircraft fuel saving using flight management system and its validation on the l-1011 aircraft,” in *2013 Aviation Technology, Integration, and Operations Conference*, p. 4290, 2013.
- [68] R. S. F. Patrón, R. M. Botez, and D. Labour, “New altitude optimisation algorithm for the flight management system cma-9000 improvement on the a310 and l-1011 aircraft,” *The Aeronautical Journal (1968)*, vol. 117, no. 1194, pp. 787–805, 2013.
- [69] ICAO, “Rules of the air,” 2005.